Superconductivity in correlated multiorbital systems with spin-orbit coupling: Coexistence of even- and odd-frequency pairing, and the case of Sr₂RuO₄

O. Gingras [1,2,3,*] N. Allaglo,[2] R. Nourafkan,[2] M. Côté [3] and A.-M. S. Tremblay [2]

[1]*Center for Computational Quantum Physics, Flatiron Institute, 162 Fifth Avenue, New York, New York 10010, USA*
[2]*Département de Physique, Institut quantique, Université de Sherbrooke, Sherbrooke, Québec J1K 2R1, Canada*
[3]*Département de Physique, Université de Montréal, C. P. 6128, Succursale Centre-Ville, Montréal, Québec H3C 3J7, Canada*

The superconducting order parameter of strontium ruthenate is the center of a lasting puzzle calling for theoretical studies that include the seldom-considered effects of spin-orbit coupling and the frequency-dependence of the order parameters. Here we generalize the frequency-dependent theory of superconductivity mediated by spin and charge fluctuations to include spin-orbit coupling in multiorbital systems and we characterize the superconducting states using the spin-parity-orbital-time *SPOT* quantum numbers, group theory, and phase distributions in the complex plane. We derive a pseudospin formulation that maps the inter-pseudospin sector of the normal state Eliashberg equation to a pseudospin-diagonal one. Possible superconducting order parameters for strontium ruthenate are obtained starting from a realistic density-functional-theory normal state. We find that spin-orbit coupling leads to ubiquitous entanglement of spin and orbital quantum numbers, along with notable mixing between even- and odd-frequency correlations. We propose a phase diagram obtained from the temperature dependence of the leading and subleading symmetries in the pseudospin-orbital basis. An accidental degeneracy between leading inter-pseudospin symmetries in strontium ruthenate, B_{1g}^+ and A_{2g}^-, could resolve apparent experimental contradictions.

I. INTRODUCTION

For several decades, the paradigm of *s*-wave superconductivity has been found inadequate to describe superconductivity in correlated systems. Instead, these materials host a rich variety of superconducting order parameters (SCOP). In these so-called unconventional superconductors, many SCOPs have already been identified and understood as highly dependent on the underlying electronic structure and on electronic interactions. For example, the SCOP in high-temperature cuprate superconductors has been shown to have *d*-wave, or more accurately, B_{1g} symmetry, emerging from the interplay between the electronic kinetic energy and single orbital Coulomb repulsion [1–9]. In Hund's metals with 3*d* electrons such as the iron-based superconductors, the local Coulomb repulsion at the Fermi level acts on multiple orbitals [10]. Pnictides can exhibit $s^\pm$-wave, an A_{1g} symmetry with a sign change between different Fermi surfaces [11].

Usually, one would think that the symmetry of a system's SCOP should be identified rather quickly. It is thus surprising that, after several decades of work leading to remarkable progress of experimental probes and numerical methods, the symmetry of the SCOP of strontium ruthenate (Sr₂RuO₄, SRO) has not yet been unambiguously established [12,13]. The reason is that certain measurements appear contradictory. This is not only an experimental challenge but also one for theories of strong electronic correlations in 4*d*/5*d* multior-

bital system with important spin-orbit coupling (SOC). A large variety of symmetries are possible in this materials, thus making the prediction of SCOPs more challenging [14,15].

In SRO, initially reckoned a spin-triplet state due to its constant Knight-shift [16,17], independent verifications have highlighted a heating effect so that a dominantly spin-singlet state appears more credible [18–20]. Another experiment probing spins using polarized neutrons met a similar fate [21,22]. Previously in contradiction with evidences for Pauli limiting [12,23], these experiments now agree.

Another critical characteristic of SRO is its two-component nature inferred by evidences of time-reversal (TR) symmetry breaking [24,25]. Ultrasound experiments also support a two-component SCOP that couples to the B_{2g} shear mode [26,27]. Additionally, the enhancement of the critical temperature under uniaxial pressure [23] not only provides strong evidence for an even-parity (*e-p*) SCOP [28], it is also a useful knob to study this two-component property. Indeed, muon spin relaxation (μSR) measurements observed two transition temperatures under pressure, indicative of a lifted degeneracy between the two components [29]. Surprisingly however, specific heat measurements, known to be extremely sensitive to superconducting transitions, have detected only a single transition temperature [30].

Consequently, various theoretical proposals have been formulated in replacement to the initial chiral *p*-wave state [31], including domain-wall physics and inhomogeneities [32,33]. A two-component character can be realized in two ways. First, the components can be degenerate by symmetry if the SCOP transforms like a two-dimensional (2D) irreducible

*ogingras@flatironinstitute.org

representation (irrep) of the D_{4h} point group. The only *e-p* such possibility is the E_g irrep. One such proposed state is the $d_{xz} + id_{yz}$, which could originate from momentum-dependent **k**-SOC [34,35]. However, density-functional theory (DFT) expects this coupling to be negligibly small in SRO, known to have a quasi-2D character [36,37]. Moreover, these E_g states under uniaxial stress should generate two transitions in specific heat.

Another possibility for two components is that they are degenerate by accident and transform like different irreps. The most natural of the two components is a $d_{x^2-y^2}$ B_{1g} state, since thermal conductivity and scanning tunneling microscopy point in this direction [38,39] and it should originate from antiferromagnetic fluctuations predicted by DFT [40] and from the strong spin fluctuations caused by the nesting of the quasi-one-dimensional bands [41]. Such a symmetry was well studied in the context of the cuprates [1,2]. For the second component, some studies have proposed an extended *s*-wave [42–44] or odd-parity (*o-p*) states [45–49] also originating from this strong nesting vector. Unfortunately, these combination would not couple to the B_{2g} shear mode. Other studies proposed $g_{xy(x^2-y^2)}$ A_{2g}, a higher angular momentum version of $d_{x^2-y^2}$ [50–53]. The similar nodal structures of $d_{x^2-y^2}$ and $g_{xy(x^2-y^2)}$ could reduce the signature on specific heat, but not remove it entirely. It has been proposed theoretically that this accidental degeneracy is more consistent with ultrasound experiments than the other symmetry-protected $d_{xz} + id_{yz}$ proposal [54]. Moving away from the $d_{x^2-y^2}$ state, a $d_{xy} \pm is^*$ state was proposed also proposed [55,56]. However, accidental degeneracies should be lifted by small perturbations. Although not definitive, μSR measurements under isotropic conditions did not observe a split in the critical temperatures [57]. Additionally, disorder by nonmagnetic impurities could help split the transition temperatures [58].

These seemingly inconsistent results suggest that the set of SCOP considered up to now might be incomplete. To guide potential SCOP candidates, we need to first construct an accurate normal state electronic structure on which to build many-body correlations that should generate a broad richness of possible superconducting states in SRO. The dominant mechanism explaining its superconductivity is pairing mediated by the exchange of spin and charge fluctuations [2,59–61]. The Bardeen-Cooper-Schrieffer [62] and Ginzburg-Landau theories [63] neglect the frequency dependence of this interaction, or replace it by a single even in frequency sharp cutoff at the Debye frequency. Doing so constrains the Gorkov function $\langle T_\tau \psi(\tau)\psi \rangle$ to be purely even in imaginary time and correspondingly in frequency (even-frequency). These approaches hide not only the frequency structure of possible SCOPs but also neglect a whole set of superconducting states that are purely odd in fermionic frequency (odd-frequency) [64]. This type of superconductivity was first proposed by Berezinskii in the context of ^{3}He [65] and then in the strong coupling limit of the electron-phonon interaction [66–68]. It is now considered ubiquitous at interfaces [69–71], impurity sites [72], and in some multiorbital systems [73–75]. The finite Kerr effect observed in SRO was linked with the presence of odd-frequency correlations [76]. In previous papers [40,77], pure odd-frequency solutions were found when examining leading superconducting instabilities of SRO without

SOC. These seldom-considered odd-frequency pairing correlations could help understand the ambiguous behavior of SRO and we are interested to study how they arise in the presence of SOC.

In this paper, we generalize the frequency-dependent formulation of superconductivity mediated by spin and charge fluctuations in multiorbital systems [40,61,78,79] to include SOC. Although the approach developed is general, in the present study we apply it solely to the SRO case.

We present in Sec. II results from density functional theory (DFT) after a qualitative discussion of the electronic structure of SRO. We explain the effects of SOC and how a pseudospin symmetry is respected for the t_{2g} orbitals in the quasi-2D approximation. In Sec. III, frequency-dependent two-body vertex corrections are generalized to incorporate SOC. In the particle-hole (*p-h*) channel, vertex corrections are quantified at the level of the random phase approximation (RPA) using Stoner factors. We study the effect of these *p-h* fluctuations on the normal state *p-p* scattering through what we refer to as the normal state linearized Eliashberg equations. We explain how pseudospin and inversion symmetries simplify numerical calculations to the same level of numerical complexity as in the absence of SOC.

In Sec. IV, we present tools to characterize multi-spin-orbital frequency-dependent Gorkov functions. First, *SPOT* decomposition [64] allows to quantify the mixing (entanglement) of spin, momentum, orbital, and imaginary-time quantum numbers. Second, with group theory we classify SCOPs by irreps of the normal state's space group along with time-reversal (TR) symmetry. In particular, we tabulate the irreps describing how the spin-orbital components of the Cooper pairs transform in t_{2g} systems.

In Sec. V, we present the resulting phase diagram of the leading and subleading gap function symmetries that can emerge from the normal state, depending on the interactions. We find that SOC couples multiple spin-orbital sectors within a specific irrep and naturally intricates *SPOT* combinations. This mixing induces phases differences between components of the gap function but preserves TR symmetry. As leading symmetries, we find two states with coexisting *SPOT* contributions in all spin-orbital sectors. One is a B_{1g}^+ state whose intraorbital components are purely even frequency, compatible with many proposed solutions for SRO. The other is an A_{2g}^- state whose intraorbital components are purely odd-frequency. This state is a SOC generalization of the odd-frequency state found in Ref. [40] when neglecting SOC. The weighted distributions of the phases of these leading candidates are studied and suggest a complex interference between the different *SPOT* contributions. We also study the temperature dependence of a few leading eigenvalues at two points of the phase diagram. Some symmetries exhibit nonmonotonous behaviors. As subleading states, we find other states that have odd-frequency intraorbital character: an odd-parity E_u^- *p*-wave-like, another A_{2g}^- and an A_{1g}^- state.

II. NORMAL STATE ELECTRONIC STRUCTURE

The normal state's electronic structure is essential to understand the emergence of an unconventional superconducting state. Similarly to the cuprates, the dominant interactions at

the Fermi level of body-centered tetragonal SRO involve the quasi-2D ruthenium-oxide planes [36,37]. In Sec. II A, we discuss the ruthenium (Ru) atomic problem, which has partially filled $4d$ electrons. Their localized nature leads to sizable multiorbital Coulomb repulsion that can generate the potential mediators of superconductivity. Furthermore, the large atomic number of these atoms implies strong local SOC. Spin is no longer a conserved quantity but pseudospin is. In Sec. II B, we introduce the lattice. The Ru atom is in the center of a tetragonally elongated octahedron of oxygen (O) atoms. The resulting crystal field Δ_{CF} splits the Ru-$4d$ electrons into the t_{2g} and the e_g subsets. Omitting the unoccupied e_g states, we model local interactions on a DFT Hamiltonian downfolded to the t_{2g} orbitals using projectors. In this Hamiltonian, the effect of SOC on the O atoms effectively act as **k**-dependent SOC. In the quasi-2D approximation, the pseudospin basis stays diagonal. Details and orbital characters of the resulting Fermi surfaces are presented in Sec. II C.

A. Atomic problem

In strongly correlated unconventional superconductors, Cooper pairs emerge from strong electron-electron interactions. The simplest interacting model showcasing this property is the one-band Hubbard Hamiltonian [80–84]. Its multiorbital generalization is the Kanamori-Slater Hamiltonian (KSM) [85]. Its rotationally invariant formulation is detailed in Appendix C and its expression given in Eq. (C1). It depends on two parameters: on-site Coulomb repulsion U and Hund's coupling J. In SRO, studies based on realistic electronic structures have shown that strong electronic correlations improve considerably the quantitative description of the one- and two-body propagators characterizing its normal state [86–91]. In this paper, we include strong electronic correlations only at the two-body level through spin and charge fluctuation theory described in Sec. III and detailed in Appendices A and B.

Another key physical mechanism affecting the Ru-$4d$ electrons is SOC [92]. This relativistic effect induced by the important electrostatic potential generated by Ru's large nucleus couples the electronic spin $\boldsymbol{S}$ and angular momentum $\boldsymbol{L}$ together. When acting on Ru-$4d$ states, these operators respectively have norms $l = 2$ and $s = \frac{1}{2}$. We use a basis that is diagonal in the projections L_z and S_z along the $\hat{z}$ axis. The atomic SOC is purely local and thus transforms like the A_{1g} irrep of the D_{4h} space group. It has the form $H_{SOC}^{A_{1g}} = \lambda_{SOC}^{A_{1g}} \boldsymbol{L} \cdot \boldsymbol{S}$, which can be recast into ladder operators that couple states with quantum numbers $L_z = l_z$ and $S_z = \frac{1}{2}$ with those having $L_z = l_z + 1$ and $S_z = -\frac{1}{2}$. This coupling is thus block tridiagonal in spin-angular momentum space as represented in Fig. 1(a). Consequently, the electrons are better described by the total angular momentum quantum operator $\boldsymbol{J} = \boldsymbol{L} + \boldsymbol{S}$ with the eigenstates' quantum numbers $|j, J_z\rangle$ where j is a half-integer between $\frac{1}{2}$ and $2 + \frac{1}{2}$ and J_z can go from $-j$ to j. As a result, the 10-fold degeneracy of $4d$ electrons with $l, s = 2, \frac{1}{2}$ is broken into a four- and a sixfold subsets respectively characterized by the total angular momenta $j = \frac{3}{2}$ and $\frac{5}{2}$. Figure 1(b) shows which spin-angular
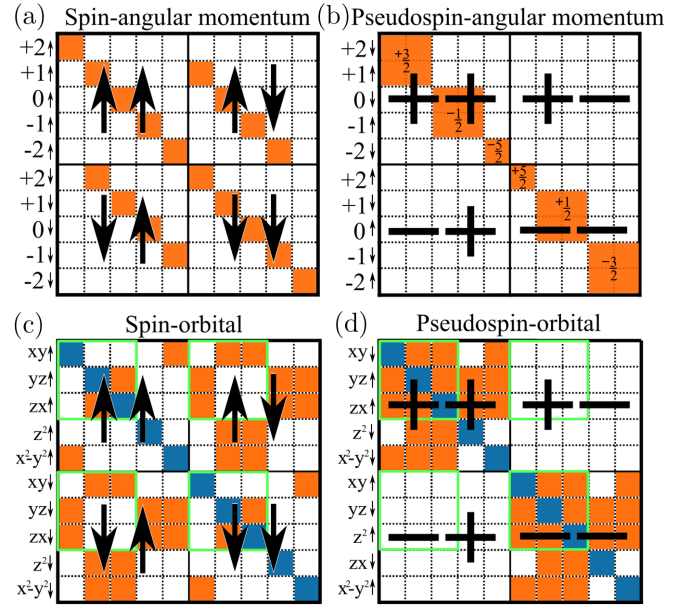

FIG. 1. Nonzero components of the Hamiltonian projected on the Ru-$4d$ shell in different basis sets, that is the (a) spin-angular momentum, (b) pseudospin-angular momentum with the J_z labels, (c) spin-orbital, and (d) pseudospin-orbital basis. All basis include atomic SOC components in orange (grey) and the effects of the crystal field are highlighted in blue (dark grey) for the orbital basis. The lime (light grey) squares highlight the t_{2g} subset in the orbital basis.

momentum states are necessary to combine to construct a state with a given J_z.

B. Crystal field and pseudospin basis

The crystal structure in which the atoms are embedded breaks the spherical symmetry of the atomic limit. In many correlated superconductors, the solutions to the local crystal field are real spherical harmonics also called orbitals. In SRO, the space group is D_{4h} and the Ru atom sits in the center of a tetragonal octahedron of O atoms. The hybridization between Ru-$4d$ and O-p electrons separates the $4d$-shell into the t_{2g} and e_g subsets, depicted in Fig. 2(a). The elongated nature of the octahedron introduces further splittings within these subsets.

The t_{2g} subset includes a quasi-2D d_{xy} orbital along with two symmetry related quasi-one-dimensional d_{yz} and d_{zx} orbitals while d_{z^2} and $d_{x^2-y^2}$ form the e_g subset. These orbitals are shown in Fig. 2(b) and the transformation from the angular momenta to the orbitals is given by

$$|z^2\rangle = |l_z = 0\rangle, \quad \begin{matrix} |yz\rangle \\ |zx\rangle \end{matrix} = \begin{bmatrix} \frac{i}{\sqrt{2}} & \frac{i}{\sqrt{2}} \\ \frac{i}{\sqrt{2}} & \frac{-i}{\sqrt{2}} \end{bmatrix} \begin{matrix} |l_z = -1\rangle \\ |l_z = +1\rangle \end{matrix}$$

$$\begin{matrix} |xy\rangle \\ |x^2 - y^2\rangle \end{matrix} = \begin{bmatrix} \frac{1}{\sqrt{2}} & \frac{-1}{\sqrt{2}} \\ \frac{1}{\sqrt{2}} & \frac{1}{\sqrt{2}} \end{bmatrix} \begin{matrix} |l_z = -2\rangle \\ |l_z = +2\rangle \end{matrix}. \quad (1)$$

The nonvanishing crystal field and SOC components of the Hamiltonian in the spin-orbital basis are depicted in Fig. 1(c).

The orbitals diagonalize the CF Hamiltonian but not $H_{SOC}^{A_{1g}}$. Using the total angular momentum instead, it can be
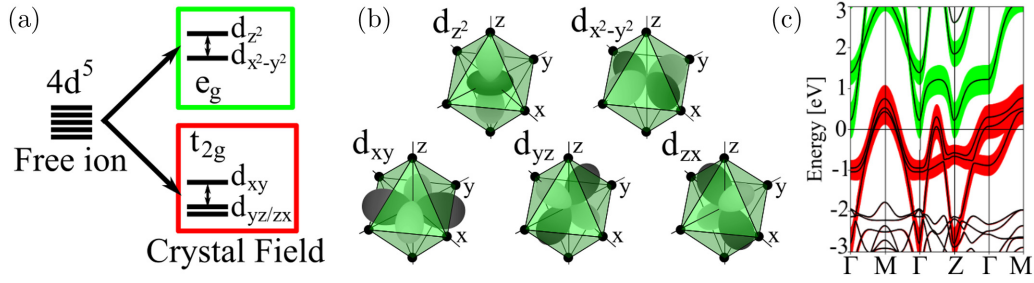
FIG. 2. Effect of the crystal field generated by the octahedron of oxygen atoms around the Ru-4d electrons. (a) Cartoon of the splittings. In a perfect octahedral environment, the t_{2g} and e_g electrons are split. Including the elongation of the octahedron generates further splittings within these subsets. (b) Real spherical harmonics associated with the eigenstates of the crystal field potential. (c) Projection of a realistic electronic band structure on the t_{2g} states in red (dark grey) and the e_g states in green (light grey). There are no e_g states at the Fermi level, which is shifted to 0 in this figure. The labels of the high-symmetry points are shown in Fig. 4.

diagonalized into two blocks, as shown in Fig. 1(d). As one can see, the pseudospin is an orbital dependent spin defined as

$$\rho = \pm \quad \text{for } J_z \in \left\{ \pm\frac{1}{2}, \mp\frac{3}{2}, \pm\frac{5}{2} \right\}. \tag{2}$$

Although predominantly local, SOC can have additional contributions to the atomic part. For example, an electron from the Ru-4d shell could hop to a neighboring O, flip its spin because of SOC and hop back with a different spin. Thus, when downfolding to the Ru-t_{2g} orbitals, this SOC process appears as being momentum dependent and is known as **k**-SOC. In Ref. [35], they find that different hoping sequences lead to three such effective couplings: the intralayer $H_{\text{SOC}}^{\text{B}_{1g}}$ and $H_{\text{SOC}}^{\text{B}_{2g}}$, along with the interlayer $H_{\text{SOC}}^{\text{E}_g}$ terms. In the t_{2g} subset, $H_{\text{SOC}}^{\text{B}_{1g}}$ and $H_{\text{SOC}}^{\text{B}_{2g}}$ connect electrons on the xy orbital having a spin σ with electrons on the yz and zx orbitals having a spin $-\sigma$. These contributions are intra-pseudospin. $H_{\text{SOC}}^{\text{E}_g}$, on the other hand, is inter-pseudospin since it connects an electron in the xy orbital with one in the yz and zy orbitals without affecting its spin. Fortunately, SOC associated to O-p electrons is small, as is also interlayer hoping in SRO. Consequently, DFT predicts this inter-pseudospin potential to be negligibly small [35], as we find. In the present paper, we use the quasi-2D character of SRO to simulate the $k_z = 0$ and $k_z = 2\pi/c$ planes for which the $H_{\text{SOC}}^{\text{E}_g}$ coupling completely vanishes. Thus the noninteracting Hamiltonian is block diagonal, a useful property to simplify the problem.

C. Realistic electronic structure

In spin and charge fluctuation theory, the superconductivity is mediated through partially filled orbitals of the correlated atoms only. Devising a tight-binding model of the appropriate set of local orbitals requires to fit many parameters. Instead, we start from a realistic electronic structure that we downfold onto the appropriate set of local orbitals. We use DFT from the ABINIT package [93–95] with the projected augmented wavefunction pseudopotentials [96,97].

In 4d electron systems, the crystal-filed splitting is sufficiently larger than SOC such that the latter can be considered as a perturbation with respect to the former. In SRO, there are only four electrons that partially fill the 4d-t_{2g} shell of the Ru atom and the 4d-e_g are states too far above the Fermi level to mix with the t_{2g} orbitals. This is confirmed by looking at the orbital character of the band structure obtained using DFT as shown in Fig. 2(c). Thus we omit the e_g states and project the Hamiltonian on the t_{2g} subset only.

The large SOC on the Ru atom couples the xy with the xz and yz orbitals with opposite spins. Without SOC, spin conservation makes the normal-state Hamiltonian diagonal in spins while crystal-field symmetry preserves the block diagonal form of the xz, yz sector. With SOC, the spin and orbital sectors are coupled [92]. The intra-pseudospin block of the normal-state Hamiltonian shown in Fig. 1(d) would be diagonal in the band basis, but we work in the orbital basis since it is the natural choice to study spin and charge fluctuations originating from local interactions. The colors in Fig. 3 represent the orbital characters of the resulting Fermi sheets in the first Brillouin zone. The α and β sheets mainly comes from quasi-one-dimensional bands with xz and yz orbital char-
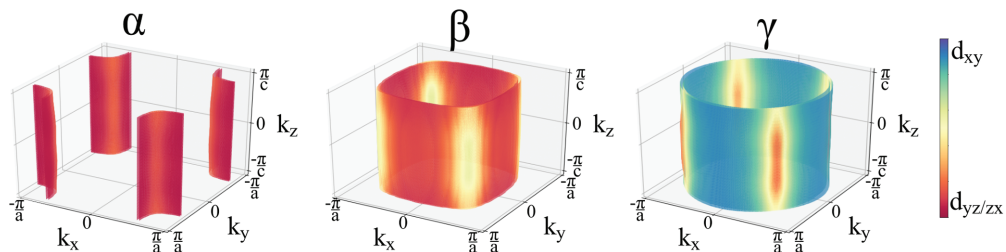

FIG. 3. Orbital character projected on the α, β, and γ Fermi sheets as also calculated in Ref. [92]. The blue color corresponds to xy orbital character while the red color corresponds to yz and xz orbital characters without distinction between these two.
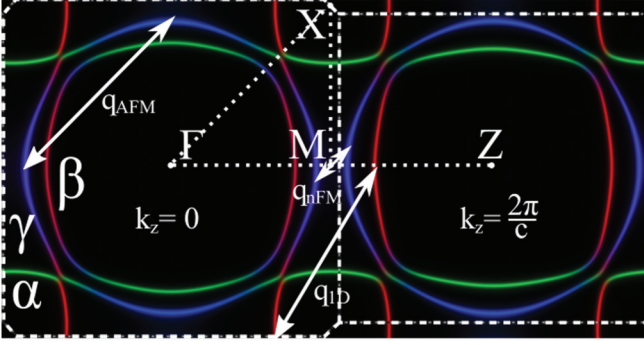
FIG. 4. Spectral function in the orbital basis of the noninteracting system obtained by DFT with SOC for in-plane momenta $k_z = 0$ and $k_z = \frac{2\pi}{c}$. The resulting α, β, and γ bands form the Fermi surface. The xy, yz, and zx orbitals of the Ru atom are projected on the Fermi surface with orbital character identified by the blue, green, and red colors respectively. High-symmetry points are label and connected by dots to show a specific path. Dashed lines highlight the Brillouin zone, characterized by its body-centered tetragonal nature. The arrows label different dominant nesting vectors of the Fermi surface defined in Fig. 5(a).

acters, while the γ sheet is mostly a quasi-2D band with xy orbital character. The color code clearly shows that SOC introduces spin-orbital entanglement around the $k_x = \pm k_y$ diagonals, most obvious there because the bands are degenerate at these points in the absence of SOC.

Similarly, Fig. 4 shows the projection of the xy, yz, zx orbital characters on the α, β, and γ bands at the Fermi surface for cuts $k_z = 0$ and $k_z = 2\pi/c$. These k_z momenta are connected by in-plane vectors because of the body-centered nature of the D_{4h} space group. We use the downfolded spin-orbital Hamiltonian to construct $\boldsymbol{G}^{\rho}_{Kl_1l_2}$, the Green's functions that characterize the propagation of a normal state's quasiparticle with pseudospin ρ from orbital l_1 to l_2 with energy momentum $K \equiv (i\omega_m, \mathbf{k})$. This model Green's function is connected to the general Green's function in Appendix D and its properties are given in Appendix E.

Now starting from the normal state, we study instabilities towards ordered states. In SRO, the Fermi liquid (FL) state preceding the superconducting state appears below $T_{\mathrm{FL}} \sim$ 25 K [36,98]. By using DFT, we have a well-defined Fermi liquid, which allows us to study the role of SOC but neglects strong electronic correlations at the one-body level. Although various studies have shown their importance for SRO [86–91], none of them was able to correctly account for electronic correlations, SOC and temperatures below T_{FL} at the same time. The exactitude of SRO's normal state in its Fermi liquid regime is an ongoing challenge. In this context, we decided to focus on generalizing spin and charge fluctuation mediated superconductivity to multiorbital systems with SOC. This formalism will remain valid once it will be possible to include all ingredients to obtain the normal state of SRO.

III. SPIN AND CHARGE FLUCTUATION THEORY

Since interactions are diagonal in the basis of isolated atoms, they do not commute with the band Hamiltonian. In perturbation theory, even the ground state is a linear com-

bination of Slater determinants. With long-range Coulomb repulsion being screened, the atomic interactions that are left lead to rather large energy denominators. Instead, a band electron creates electron-hole pairs best described as spin and charge-density waves. These influence other electrons, a process known as electron-electron scattering by exchange of spin- or charge-density fluctuations. They are the lowest-energy excitations and hence lead to small energy denominators in perturbation theory. The resulting phase diagrams exhibit a rich variety of competing ordered states with associated order parameters. Isoelectronic doping suggests that SRO lies in the vicinity of magnetic orderings [99], consistent with the important spin fluctuations found by neutron scattering [41,100–102]. In addition, the well-established correlated character of Ru t_{2g} electrons [86–91,103] makes SRO the archetypal representative of superconductivity mediated by spin and charge fluctuations. In this section we summarize the basic ideas, which are formulated in more details in Appendices A and B.

In Sec. III A, two-body susceptibilities $\boldsymbol{\chi}_\alpha$ are introduced from a free-energy perspective for α either the p-h or the p-p channels. They can signal phase transitions and are expressed in terms of bare susceptibilities $\boldsymbol{\chi}^0_\alpha$, complemented with vertex corrections. We present the dominant components of the bare susceptibilities and discuss the origin of their momentum and orbital structure. We comment on the interplay between both channels through Parquet equations.

In Sec. III B, the enhancement of spin (charge) fluctuations due to two-body interactions in the p-h channel is quantified using the magnetic (density) Stoner factor S^m (S^d). We model the p-h vertex corrections using the Kanamori-Slater Hamiltonian (KSH), incorporated within the random phase approximation (RPA). We verify a scaling relation observed in the bare vertex and justify our choice of parameter sampling.

Now, these spin and charge fluctuations generated by local interactions can mediate pairing in the p-p channel. Ultimately, we are interested in the structure of resulting SCOPs, solutions to the linearized Eliashberg equation. Applying the frequency-dependent formulation of the pairing interactions to multiorbital systems with SOC is extremely challenging and requires huge numerical capabilities. In Sec. III C, we show how the linearized Eliashberg equation for systems with inversion and pseudospin symmetries can be effectively reduced to a problem that is as computationally expensive as the spin-diagonal case encountered when there is no SOC.

A. Two-particle susceptibilities

As derived in Appendix A, instabilities can be found from responses to source fields. At the two-body level, they are either number-conserving or pairing fields, respectively taking the forms

$$\psi^\dagger(\mathbf{2})\boldsymbol{\phi}_{11}(\mathbf{2}; \mathbf{1})\psi(\mathbf{1}) \quad \text{and} \quad \psi(\mathbf{2})\boldsymbol{\phi}_{21}(\mathbf{2}; \mathbf{1})\psi(\mathbf{1}) \qquad (3)$$

with corresponding Hermitian conjugates. Here we use the superindex $\boldsymbol{i} \equiv (\mathbf{k}_i, \mu_i, \tau_i)$, which contains momentum, spin-orbital $\mu_i \equiv (\sigma_i, l_i)$, and imaginary time quantum numbers of an electron created and destroyed, respectively, by $\psi^\dagger(\boldsymbol{i})$ and $\psi(\boldsymbol{i})$. Taking the first derivative of the free energy $\mathcal{F}$ with respect to those fields respectively lead to the normal and
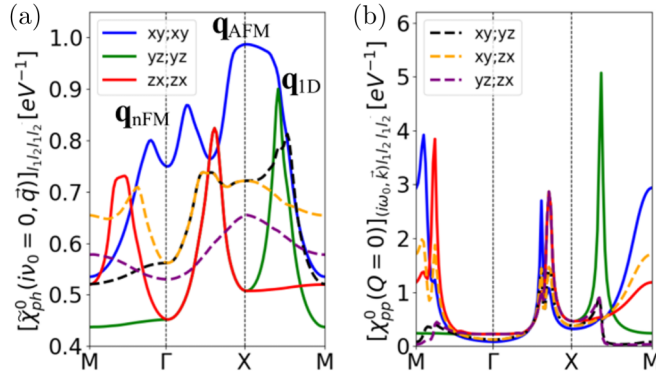
FIG. 5. Real part of the dominant intraspin components of the (a) *p-h* and (b) *p-p* bare susceptibilities in the orbital basis along a high-symmetry path. Full lines (dashed lines) are attributed to the intraorbital (interorbital) components. In (a), we show the RPA susceptibility $\tilde{\chi}^0_{ph}$ defined in Eq. (13) and important peaks associated to nesting vectors in Fig. 4 are identified. We verified that the interspin components are negligible compared to the intraspin ones.

anomalous Green's functions

$$G(1;2) = \beta \left.\frac{\delta \mathcal{F}[\phi]}{\delta \phi_{11}(2;1)}\right|_{\phi=0} \text{ and } F(1;2) = \beta \left.\frac{\delta \mathcal{F}[\phi]}{\delta \phi_{21}(2;1)}\right|_{\phi=0}.$$

(4)

In the normal state, G describes the propagation of an electron, with its largest value near the Fermi energy momentum. Introducing more electronic correlations at the one-body level makes electrons further away from the Fermi energy contribute more [40]. On the other hand, F does not conserve the number of particles and must vanish in the absence of source-fields in the normal state. More details and properties of G and F are given in Appendices D and E.

The second derivatives lead to two-body susceptibilities χ_α. A transition from the normal to an ordered phase happens when infinitesimally small fields can trigger finite responses, signaled by a diverging χ_α at low temperature. Neglecting two-body interactions, we find the bare susceptibilities χ^0_α given by

$$\left[\chi^0_{ph}(Q)\right]^{\mu_1\mu_2\mu_3\mu_4}_{KK'} = -\frac{1}{\beta} G^{\mu_1\mu_3}_{K+Q} G^{\mu_4\mu_2}_K \delta_{KK'},$$

(5)

$$\left[\chi^0_{pp}(Q)\right]^{\mu_1\mu_2\mu_3\mu_4}_{KK'} = \frac{1}{2\beta} G^{\mu_1\mu_3}_{K+Q} G^{\mu_2\mu_4}_{-K} \delta_{KK'},$$

(6)

where $K = (\mathbf{k}, i\omega_m)$, $K' = (\mathbf{k}', i\omega'_m)$ are the fermionic four-momentum vectors and $Q = (\mathbf{q}, i\nu_n)$ the bosonic one. β is the inverse temperature. In this paper, χ^0_α are constructed from a DFT calculation with SOC. Several relations for χ^0_{pp} are given in Appendix F.

In Fig. 5(a), we show the real part of the dominant intra- and interorbital components of $\tilde{\chi}^0_{ph} \equiv \frac{1}{N\beta} \sum_K [\chi^0_{ph}]_{KK}$ at $i\nu_0 = 0$ with N the number of K points. The summation is perform at the bare level, justified by the subsequent RPA dressing explained in Sec. III B. We only show intraspin components as they dominate. Because the DFT propagators characterize mostly states at the Fermi level, the $\mathbf{q}$ vectors for which the susceptibility has peaks are associated with the overlapping of a part the Fermi sheets and another that is shifted by $\mathbf{q}$.

These peaks are called nesting vectors and, for SRO, some are labeled in Fig. 5(a) and are visualized in Fig. 4. They were similarly discussed in Ref. [40]. The $\mathbf{q}_{1D}$ vector that folds nicely the β band onto the α one is largest in the *yz-zx* orbitals sector. $\mathbf{q}_{1D}$ was experimentally characterized by various neutron scattering experiments [41,100,102,104]. The two other labeled peaks involve the large pockets of states of the γ band, with *xy* character. These pockets are near a van Hove singularity where the density of states diverges [105–107]. In certain pressure conditions, the γ band reaches the van Hove singularity, leading to a Lifshitz transition [23,28,108–114]. The nesting of these pockets produces an antiferromagnetic (AFM) plateau along with a nearly ferromagnetic (nFM) peak. Neglecting SOC, these peaks were similar in height [40]. Including SOC, the AFM peak is significantly favored over to the nFM one.

In Fig. 5(b), we show the same components but for the real part of χ^0_{pp}. We look only at the $Q = 0$ bosonic four-momentum because we are interested in superconducting Cooper pairs with no center-of-mass energy momentum, as discussed in Sec. III C. In fermionic Matsubara frequencies, we show only $i\omega_0$ for which the susceptibility is largest. As understood from inversion symmetry in Eq. (6), the peaks are associated to $\mathbf{k}$ points of the Fermi surface. By inspecting carefully a peak of an intraorbital component, one can observe that many peaks are split in two because different orbitals contribute to nearly touching Fermi sheets due to SOC.

Now we include two-body interactions captured by the irreducible vertices $\boldsymbol{\Gamma}_\alpha$. Susceptibilities χ_α are expressed in series expansions in the interactions as

$$\chi_{ph} = \frac{\chi^0_{ph}}{1 - \boldsymbol{\Gamma}_{ph}\chi^0_{ph}} \quad \text{and} \quad \chi_{pp} = \frac{\chi^0_{pp}}{1 - \boldsymbol{\Gamma}_{pp}\chi^0_{pp}}$$

(7)

that are commonly called the Bethe-Salpeter equations [115]. An instability in the α channel is attained once the largest eigenvalue λ_α of the operator $V_\alpha = \boldsymbol{\Gamma}_\alpha \chi^0_\alpha$ reaches unity. Then the associated χ_α diverges and the system reorganizes in a different phase. These vertices result from electronic interactions and are coupled through the Parquet equations derived in Appendix B. It is this complex interplay that leads to competition between ordered states and a rich variety of emergent phases in correlated systems [59,60,116]. The idea of spin and charge fluctuation mediated superconductivity is that although the *p-h* fluctuations can be too weak to induce a transition in the *p-h* channel, they still can mediate interactions in the *p-p* channel that leads to a divergence. Indeed in this scenario, the SCOPs are very dependent on the details of the *p-h* fluctuations and thus the electronic interactions. The subtle competition between different nesting vectors in the spin and charge channels has a crucial influence on the type and symmetry of the superconducting states that can arise.

B. Stoner factors in the particle-hole channel

In the *p-h* channel, the largest eigenvalue of V_{ph} called the Stoner factor never reaches unity. Doing so would mean we have already fallen into a magnetic or charge order. We use the Stoner factor as a quantifier of the proximity to a *p-h* ordered state, since it measures the enhancement in *p-h* fluctuations due to two-body interactions. Without SOC, the

system is spin-diagonal and V_{ph} is block diagonal in the so-called density and magnetic channels associated respectively with singlet and triplet particle-hole fluctuations. In the $S_z = 0$ channel, the density/magnetic (d/m) block is given as

$$V_{d/m}^0(Q) \equiv V_{ph}^{\uparrow\uparrow\uparrow\uparrow}(Q) + / - V_{ph}^{\uparrow\uparrow\downarrow\downarrow}(Q) \qquad (8)$$

where we used $V_{ph}^{\sigma\sigma\sigma'\sigma'}(Q) = V_{ph}^{\sigma'\sigma'\sigma\sigma}(Q)$. The other magnetic channels with $S_z = \pm 1$ are obtained as

$$V_m^{+1}(Q) \equiv V_{ph}^{\uparrow\downarrow\uparrow\downarrow}(Q) \quad \text{and} \quad V_m^{-1}(Q) \equiv V_{ph}^{\downarrow\uparrow\downarrow\uparrow}(Q). \qquad (9)$$

Including SOC, this block diagonal property of V_{ph} is no longer true and spin and charge fluctuations are coupled together. In the present case, we observe that these deviations are small enough so that we still refer to charge (spin) fluctuations and we quantify them by looking at the density (magnetic) Stoner factors $S^{d(m)}$ defined as

$$S^{d(m)} \equiv \max \text{eig}\{V_{d(m)}^0(Q)\}. \qquad (10)$$

Let us now discuss the specific choice of vertex Γ_{ph} entering $V_{ph} = \Gamma_{ph}\chi_{ph}^0$. As discussed in Appendix C, the two-body interactions are modelled using the rotationally invariant formulation of the KSH. This model is a multiorbital generalization of the Hubbard model and depends on the on-site Coulomb repulsion U, along with the Hund's coupling J. In the p-h channel, the spinful p-h irreducible vertex function Γ_{ph} is taken as the local and static antisymmetrized Coulomb interaction Λ_{ph} explicit in Eq. (C3). Comparing with Eq. (B5), we miss ladder functions in both in the p-p and p-h channels. The p-p one can be neglected, since we work in the normal state were p-p fluctuations remain small. The p-h one is absorbed in Λ_{ph} and renormalizes U and J from the bare values to further screened ones. This is similar to what is done in the two-particle self-consistent (TPSC) approach [117].

Now the local and static properties of Λ_{ph} simplifies the dressing of the p-h susceptibility in Eq. (7) so that it becomes diagonal in fermionic four-momentum, that is

$$[\chi_{ph}(Q)]_{KK'} = [\chi_{ph}(Q)]_{KK}\delta_{KK'}. \qquad (11)$$

Moreover, the p-h susceptibility influences pairing through the ladder function (B7) that characterizes the exchange of a p-h fluctuation between to electrons. Using Eq. (11), it simplifies to

$$[\Phi(Q)]_{KK'}^{\mu_1\mu_2\mu_3\mu_4} = [\Lambda_{ph}\tilde{\chi}_{ph}(Q)\Lambda_{ph}]^{\mu_1\mu_2\mu_3\mu_4}\delta_{KK'} \qquad (12)$$

where we only need the so-called RPA susceptibility

$$\left[\tilde{\chi}_{ph}(Q)\right]^{\mu_1\mu_2\mu_3\mu_4} = \frac{1}{N\beta}\sum_K \left[\chi_{ph}(Q)\right]_{KK}^{\mu_1\mu_2\mu_3\mu_4}. \qquad (13)$$

This operation can be performed at the bare level, thus we define the RPA bare p-h susceptibility as

$$\left[\tilde{\chi}_{ph}^0(Q)\right]^{\mu_1\mu_2\mu_3\mu_4} = \frac{1}{N\beta}\sum_K \left[\chi_{ph}^0(Q)\right]_{KK}^{\mu_1\mu_2\mu_3\mu_4}. \qquad (14)$$

Several relations for $\tilde{\chi}_{ph}^0$ are given in Appendix F. This approximation reduces greatly the amount of numerical resources needed for vertex corrections at the cost of lacking a proper description of the energy-momentum dependence of the fluctuations. In this paper, we focus on the effects of SOC.

In another study neglecting SOC for a better treatment of the electronic correlations using dynamical mean-field theory (DMFT), it was shown that the frequency-dependence of the p-h vertex leads to a reduction of the AFM peak and an enhancement of the nFM one [90]. All of these effects can influence the ordering of the leading superconducting states.

In Figs. 6(a) and 6(b), we show the dependence of S^m (S^d) on the parameters U and J. Instead of these parameters, it is useful to employ J/U and S^m because they have more physically relevant interpretations, which allows to constrain them. Moreover, the p-h vertex Λ_{ph} satisfies a scaling relation Eq. (C5), which directly applies to the Stoner factors as

$$S^{d(m)}[U, J] = U \cdot S^{d(m)}[1, J/U]. \qquad (15)$$

To ensure repulsive on-site interactions in Eq. (C3), one should satisfy $J/U < 1/3$. We extend the constraint to $J/U \leqslant 0.45$ because some work have considered attractive on-site interactions in their study of superconductivity in SRO [52,118,119]. Moreover, in the spirit of Hund's coupling, which favours same spin alignment, the interorbital Coulomb repulsion should be stronger in the interspin channel $U' = U - 2J$ compared to the intraspin one $U'' = U - 3J$, imposing $J/U \geqslant 0$. As for S^m, it quantifies the role of two-body interactions in generating magnetic fluctuations. Isoelectronic doping experiments have shown that there is a lot of magnetic ordering in proximity to SRO [99]. We study $S^m \geqslant 0.5$ to tune the system in the vicinity of a magnetic instability, yet never do we reach S^m (S^d) $\geqslant 1$ since this would imply a magnetic (charge) instability in the p-h channel.

As a result, $0 \leqslant J/U \leqslant 0.45$ and $0.5 \leqslant S^m \leqslant 0.95$ defines the region of parameter space where we study superconductivity in Sec. IV. Figure 6(c) shows S^d in this parameter space, which is also highlighted by the dotted lines in Figs. 6(a) and 6(b). The charge channel becomes more important at small J/U where Hund's coupling does not force spins to be aligned so that charge can move more freely between local orbitals.

In Fig. 6(d), we highlight the scaling relation Eq. (15), which implies the dependence of $S^{d/m}/U$ over J/U and temperature. The lighter colors corresponds to $T = 1000$ K, the middle one to $T = 250$ K and the darker to $T = 100$ K. In our study, U and J are kept fixed with temperature and the dependence of the Stoner factors over temperature can be assessed from the height of the bare p-h susceptibility's peaks that sharpen with lowering temperatures. The discontinuities are associated to different leading **q** vectors depending on the interaction parameters.

C. Particle-particle channel in the pseudospin basis

In the p-p channel where instabilities lead to superconductivity, we are interested in the eigenvectors $\Delta \equiv \Delta_{pp}(Q = 0)$ of the operator $V_{pp} \equiv V_{pp}(Q = 0)$ with largest eigenvalue $\lambda \equiv \lambda_{pp}$. $Q = 0$ is chosen because, in the absence of an external magnetic field, the leading instability is usually for Cooper pairs with no net four-momentum since this minimizes the free energy by having no net superfluid flow. In the normal state, these eigenvectors characterize instabilities that satisfy
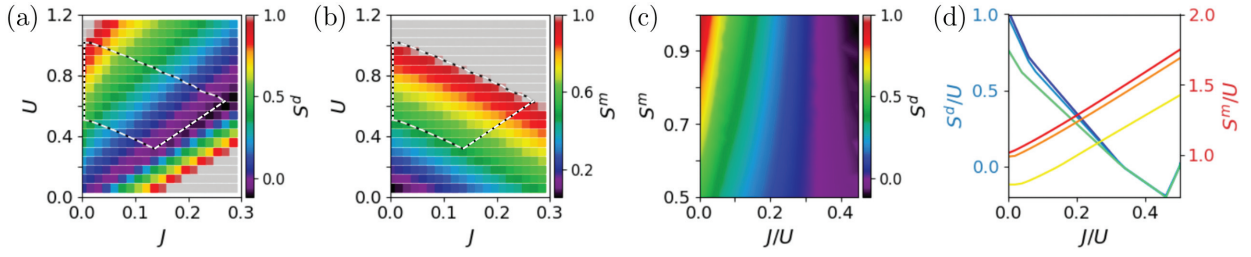
FIG. 6. At $T = 250$ K, in the J and U parameter space, (a) and (b) respectively show the density (S^d) and magnetic (S^m) Stoner factors defined by Eq. (10). Instead of U and J as parameters, we prefer to use S^m and J/U as discussed in the main text. In (c), we show S^d in this new parameter space, constrained by physical intuition. This region is highlighted in (a) and (b) by the doted lines. In (d), we show the scaling relation Eq. (15) for the Stoner factors, with their respective temperature dependence. S^d/U is plotted from dark blue to light green and S^m/U from dark red to yellow. The darker color is computed at $T = 100$ K, the one in between at $T = 250$ K and the lighter one at $T = 1000$ K. The kinks are related to changes in dominant nesting vectors.

the linearized Eliashberg equation

$$\lambda \Delta_K^{\mu_1\mu_2} = - \sum_{K'\mu_3\mu_4} [V_{pp}]_{KK'}^{\mu_1\mu_2\mu_3\mu_4} \Delta_{K'}^{\mu_3\mu_4}. \quad (16)$$

As discussed in Sec. II B, the noninteracting DFT Hamiltonian projected on the $4d$-t_{2g} orbitals of the Ru atom is diagonal in spina and orbitals when neglecting SOC. Including it entangles the spin and orbital quantum numbers of electrons. Rotating to the pseudospin-orbital basis, the quasi-2D Hamiltonian becomes diagonal in pseudospin, although orbitals and spins stay entangled. Consequently, the bare susceptibilities Eqs. (5) and (6) are also diagonal in pseudospin with

$$[\chi_\alpha^0]^{\rho_1\rho_2\rho_3\rho_4} = [\chi_\alpha^0]^{\rho_1\rho_2\rho_1\rho_2} \delta_{\rho_1\rho_3} \delta_{\rho_2\rho_4}. \quad (17)$$

As highlighted in Fig. 15 of Appendix C, our choice of p-h vertex function Λ_{ph} is spin-diagonal, but not pseudospin-diagonal. An example of an interaction diagram that does not preserve pseudospin is shown in Fig. 7, which leads to finite $[\Gamma_{ph}^0]^{\rho\rho\bar\rho\bar\rho}$ contributions, with $\bar\rho = -\rho$.

However, the dressed susceptibility is still block diagonal, having an intra-pseudospin channel

$$\chi'_{ph} = \begin{bmatrix} \chi_{ph}^{++++} & \chi_{ph}^{++--} \\ \chi_{ph}^{--++} & \chi_{ph}^{----} \end{bmatrix} \quad (18)$$

and an inter-pseudospin channel

$$\chi''_{ph} = \begin{bmatrix} \chi_{ph}^{+-+-} & \chi_{ph}^{+--+} \\ \chi_{ph}^{-++-} & \chi_{ph}^{-+-+} \end{bmatrix}. \quad (19)$$

Consequently, the pairing vertex V_{pp} can also be expressed as a block diagonal matrix in the intra- and inter-pseudospin channels. The solutions of the Eliashberg equation in each of
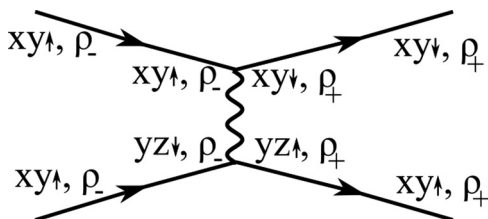

FIG. 7. Example of a first order diagram of the dressed p-h susceptibility that does not preserve pseudospin.

these channels are thus independent. Equation (16) restricted to the inter-pseudospin channel leads to the following coupled equations:

$$\lambda[\Delta_K]_{l_1l_2}^{+-} = -[V_{KK'}]_{l_1l_2l_3l_4}^{+-+-}[\Delta_{K'}]_{l_3l_4}^{+-} - [V_{KK'}]_{l_1l_2l_4l_3}^{+--+}[\Delta_{K'}]_{l_4l_3}^{-+},$$

$$\lambda[\Delta_K]_{l_1l_2}^{-+} = -[V_{KK'}]_{l_1l_2l_3l_4}^{-++-}[\Delta_{K'}]_{l_3l_4}^{+-} - [V_{KK'}]_{l_1l_2l_4l_3}^{-+-+}[\Delta_{K'}]_{l_4l_3}^{-+}, \quad (20)$$

where $V_{KK'} \equiv [V_{pp}]_{KK'}$. The Pauli principle leads to

$$[\Delta_K]_{l_1l_2}^{+-} = -[\Delta_{-K}]_{l_2l_1}^{-+} \quad (21)$$

and in systems with inversion symmetry, the solutions are either even- or odd-parity (e-p or o-p). They are defined as

$$[\Delta_K^{ep/op}]_{l_1l_2} = [\Delta_K]_{l_1l_2}^{+-} \mp [\Delta_{K^*}]_{l_2l_1}^{-+}, \quad (22)$$

with $K^* \equiv (\mathbf{k}, -i\omega_m)$. In this basis, we found that off-diagonal elements completely vanish when SOC in neglected. Considering SOC within the pseudospin approximation, we found that they were several orders of magnitude smaller than the diagonal ones so that Eqs. (20) can be expressed as

$$\lambda \begin{bmatrix} \Delta_K^{ep} \\ \Delta_K^{op} \end{bmatrix} = -\frac{1}{2} \begin{bmatrix} V_{KK'}^{ep} & 0 \\ 0 & V_{KK'}^{op} \end{bmatrix} \begin{bmatrix} \Delta_{K'}^{ep} \\ \Delta_{K'}^{op} \end{bmatrix} \quad (23)$$

where

$$[V_{KK'}^{ep/op}]_{l_1l_2l_3l_4} = [V_{KK'}]_{l_1l_2l_3l_4}^{+-+-} \mp [V_{KK'^*}]_{l_1l_2l_4l_3}^{+--+}$$
$$\mp [V_{K^*K'}]_{l_2l_1l_3l_4}^{-++-} + [V_{K^*K'^*}]_{l_2l_1l_4l_3}^{-+-+}. \quad (24)$$

Using the relation (F10), the effective pairing vertex can finally be expressed as

$$V_{KK'}^{ep/op} = [\Gamma_{KK'}^{ep/op}][\chi_{pp}^0(K')]^{+-+-} \quad (25)$$

with

$$[\Gamma_{KK'}^{ep/op}]_{l_1l_2l_3l_4} = [\Gamma_{KK'}]_{l_1l_2l_3l_4}^{+-+-} \mp [\Gamma_{KK'^*}]_{l_1l_2l_4l_3}^{+--+}$$
$$\mp [\Gamma_{K^*K'}]_{l_2l_1l_3l_4}^{-++-} + [\Gamma_{K^*K'^*}]_{l_2l_1l_4l_3}^{-+-+}. \quad (26)$$

For the intra-pseudospin channel, Pauli's exclusion principle is not sufficient to construct an effective pairing vertex and we have to solve the spinful system through Eq. (16) to study these solutions. They can be understood as having total pseudospin of 1 and pseudospin projection ± 1. Comparing

effective solutions in the inter-pseudospin channel with those of the spinful system, we not only verify that both give the same answer but also that all pseudo-triplet states are almost degenerate. This is very fortunate because, while we cannot go to low enough temperatures in the spinful case, the degeneracy between the intra-pseudospin and inter-pseudospin solutions allow us to discuss all possible solutions by only inspecting the inter-pseudospin channel.

IV. CHARACTERIZATION OF GAP FUNCTIONS

Ordered states like superconductivity are characterized by an order parameter that breaks at least one symmetry of the normal state. As explained in Sec. III, the gap function $\mathbf{\Delta}$ is an eigenvector of the pairing vertex $\mathbf{V}_{pp}$. This is the SCOP that we want to characterize. In frequency-dependent multi-spin-orbital systems, these SCOP have many degrees of freedom involving various types of classifications.

In Sec. IV A, we first introduce the *SPOT* decomposition as a tool to quantify the interplay between these quantum numbers. In Sec. IV B, we apply group theory to assign a single label, the irrep of the D_{4h} space group, that involves all quantum numbers together. We decompose spin-orbital basis functions of the t_{2g} subset in terms of irreps and discuss time-reversal symmetry. Finally in Sec. V, we apply these tools to the inter-pseudospin solutions of the effective Eliashberg equation Eq. (23) for SRO. As leading eigenvectors, we find B_{1g}^{+} and A_{2g}^{-} states. We discuss how SOC couples different orbital sectors and compare them with experiments, discuss their phase weighted distributions and investigate how their eigenvalues evolve with temperature. As subleading symmetries, we find another A_{2g}^{-}, a set of degenerate E_{u}^{-} and an A_{1g}^{-}. We discuss why we do not find some of the other proposed solutions for SRO.

A. SPOT contributions

The gap function $\mathbf{\Delta}$ transforms like the anomalous Green's function or Gorkov function $\mathbf{F}$ defined in Appendix E. It is given by a time-ordered product of two fermion destruction operators,

$$\mathbf{F}_{K}^{\mu_1\mu_2} = \int_{0}^{\beta} d\tau \, e^{i\omega_m\tau} \langle T_{\tau} \psi_{\mathbf{k}l_1}^{\sigma_1}(\tau)\psi_{-\mathbf{k}l_2}^{\sigma_2}\rangle, \tag{27}$$

where the two electrons forming a pair have four quantum numbers each: spin-orbitals $\mu_1 = (\sigma_1, l_1)$ and μ_2, along with energy momenta in Matsubara frequency $K = (i\omega_m, \mathbf{k})$ and $-K$. T_{τ} is the imaginary-time-ordering operator. Using the sign change upon the exchange of two fermions, this two-fermion object, and thus $\mathbf{\Delta}$ as well, satisfies the Pauli principle

$$\mathbf{\Delta}_{\mathbf{k}l_1 l_2}^{\sigma_1\sigma_2}(i\omega_m) = -\mathbf{\Delta}_{-\mathbf{k}l_2 l_1}^{\sigma_2\sigma_1}(-i\omega_m). \tag{28}$$

The exchange of each quantum number is respectively characterized by the $\hat{S}$, $\hat{P}^*$, $\hat{O}$, and $\hat{T}^*$ operators [64], acting as follows:

$$[\hat{S}\mathbf{\Delta}]^{\sigma_1\sigma_2} \equiv [\mathbf{\Delta}]^{\sigma_2\sigma_1}, \quad [\hat{P}^*\mathbf{\Delta}]_{\mathbf{k}} \equiv \mathbf{\Delta}_{-\mathbf{k}},$$

$$[\hat{O}\mathbf{\Delta}]_{l_1 l_2} \equiv \mathbf{\Delta}_{l_2 l_1}, \quad [\hat{T}^*\mathbf{\Delta}](i\omega_m) \equiv \mathbf{\Delta}(-i\omega_m), \tag{29}$$

where, when omitted, quantum numbers stay untouched. Note that $\hat{T}^*$ is simply the exchange of relative time, different from time reversal $\hat{\mathcal{T}}$. Moreover, there was recently a generalization of these operators to systems with strong SOC involving the exchange of total angular momentum $\hat{J}$ instead of the exchanges of spin $\hat{S}$ and orbitals $\hat{O}$ [120]. We did not consider it in this paper. In terms of these operators, Eq. (28) be expressed as $\hat{S}\hat{P}^*\hat{O}\hat{T}^*\mathbf{\Delta} = -\mathbf{\Delta}$. Because these operations are idempotent, the eigenvalues of each operators are $+$ and -1, associated to even and odd eigenvectors. The SCOPs are not necessarily eigenvectors, so we use the *SPOT* decomposition to characterize gap functions in systems where multiple *SPOT* eigenvectors are cohabiting.

In centrosymmetric systems like D_{4h}, all irreps are eigenvectors of $\hat{P}^*$ and they are labeled by g (u) for *e-p* (*o-p*). They are denoted ^{+}P (^{-}P) and gap functions remain pure in that quantum number. In spin-diagonal cases such as that obtained when neglecting SOC, gap functions satisfy $\hat{S}\mathbf{\Delta} = +(-)\mathbf{\Delta}$ for triplet ^{+}S (singlet ^{-}S) solutions. In that case, the singlet channel $\mathbf{\Delta}^{\uparrow\downarrow} - \mathbf{\Delta}^{\downarrow\uparrow}$ that has total spin 0 and the three degenerate triplet channels $\mathbf{\Delta}^{\uparrow\uparrow}$, $\mathbf{\Delta}^{\downarrow\downarrow}$ and $\mathbf{\Delta}^{\uparrow\downarrow} + \mathbf{\Delta}^{\downarrow\uparrow}$ have total spin 1 and total spin projections $+1$, -1 and 0, respectively.

Considering SOC in multiorbital systems introduces spin-flips that entangles those spin channels together and can lead to coexistence of ^{+}S and ^{-}S contributions [92]. It also introduces interorbital interactions that hybridize formerly decoupled orbital sectors. In other words, it can induce mixing between ^{+}O and ^{-}O contributions. These hybridizations between nondegenerate orbitals were shown to generate coexistence between ^{+}T and ^{-}T contributions [74,75].

In this notation, conventional superconductors are purely $^{-}S^{+}P^{+}O^{+}T$ with a *s*-wave symmetry in $\mathbf{k}$ space. Similarly, cuprates are known to be spin-singlet one-band *d*-wave superconductors [2]. On the other hand, the few candidates for spin-triplet superconductivity are usually classified as *o-p* with a pure $^{+}S^{-}P^{+}O^{+}T$ contribution. Among potential materials, there are many uranium-based materials like UPt$_3$ [121] and UTe$_2$ [122]. Also, the $p_{\pm} \pm ip_y$ chiral *p*-wave state previously proposed for SRO would classify as such triplet.

These two types of SCOP, spin-singlet and spin-triplet, are often mentioned separately in the literature because most superconducting models are single-orbital and/or spin-diagonal. In SRO however, there have been increasing discussions about ^{-}O states [14,34,43,47,118,123–125]. Additionally, a few papers have studied the frequency dependence of the gap function and found purely ^{-}T states when neglecting SOC [40,77]. Considering SOC, the coexistence between ^{+}T and ^{-}T solutions should be ubiquitous [74,75]. One paper actually linked the ubiquitous presence of ^{-}T correlations in multiorbital SRO with its observed finite Kerr effect [76].

B. Group theory

In the Ginzburg-Landau paradigm, ordered states are characterized by an order parameter, which breaks at least one symmetry of the normal state. The SCOP breaks $U(1)$ gauge symmetry, associated with breaking conservation of the total number of particles. In BCS superconductors [62,126], it is the only broken symmetry. In unconventional superconductors, the complex mechanisms mediating pairing usually lead

TABLE I. Basis functions of the SCOP in spin space expressed as irreps. S is the parity under spin exchange.

Irrep	Spin basis function	S
A_{1g}	σ_2	$-$
A_{2g}	σ_1	$+$
E_g	σ_0, σ_3	$+$

TABLE II. Basis functions of the SCOP in orbital space expressed as irreps. O is the parity under orbital exchange. $|1\pm\rangle$ and $|2\pm\rangle$ are notations that are helpful later.

Irrep	Orbital basis function	O
A_{1g}	$|xy;xy\rangle$	$+$
A_{1g}	$|yz;yz\rangle + |zx;zx\rangle$	$+$
B_{1g}	$|yz;yz\rangle - |zx;zx\rangle$	$+$
A_{2g}	$|yz;zx\rangle - |zx;yz\rangle$	$-$
B_{2g}	$|yz;zx\rangle + |zx;yz\rangle$	$+$
E_g	$|1+\rangle \equiv |xy;yz\rangle + |yz;xy\rangle$	$+$
	$|2+\rangle \equiv |xy;zx\rangle + |zx;xy\rangle$	$+$
E_g	$|1-\rangle \equiv |xy;yz\rangle - |yz;xy\rangle$	$-$
	$|2-\rangle \equiv |xy;zx\rangle - |zx;xy\rangle$	$-$

to additional symmetry breaking [116]. The different symmetries that are broken in an ordered phase have a specific label attached, referred to as an irrep. In Appendix G, we detail the symmetries and irreps of the D_{4h} space group.

As the irrep characterizing a SCOP involves all quantum numbers at the same time, it is instructive to look at how it decomposes in each of them separately. The total irrep is obtained from the direct product of the irreps of each independent space; spin, orbital, wave vector. In Sec. IVB1, we discuss the spin-orbital components themselves, without including **k** dependence. First in the case without SOC, we classify the basis functions in spin and orbital spaces separately. Then, we introduce SOC, which entangles them. Certain products of irreps become reducible while maintaining pseudospin symmetry. In Sec. IVB2, we generalize the classification of Ref. [127], but for systems with multiple *SPOT* contributions. We explain why time-reversal operation $\hat{\mathcal{T}}$ would be preferable to $\hat{T}^*$ in systems with multiple *SPOT* contributions. However, $\hat{\mathcal{T}}$ has a phase ambiguity that prevents actually using it. As an in-between, we use the frequency dependence of the intra-orbital components of the SCOP in our classification. Even-frequency (odd-frequency) intraorbital components are denoted by a $+$ ($-$) superscript in the irrep label.

1. Spin-orbital basis

Without SOC. The electrons in SRO transform like irreps of the double group $\tilde{D}_{4h}$ [128]. An irrep of this group $D_{l\sigma} \equiv D_l \otimes E_{1/2,g}$ can decomposed into the orbital part D_l and the spin part $E_{1/2,g}$. The gap function describing Cooper pairs depends on two such electrons, thus it transforms like $D_{l_1\sigma_1} \otimes D_{l_2\sigma_2}$. Without SOC, the normal state Hamiltonian is diagonal in the spin-basis and can be mapped to a doubly degenerate spin-diagonal Hamiltonian. In that case, the spin part of the gap function is separable into $E_{1/2,g} \otimes E_{1/2,g} = A_{1g} \oplus A_{2g} \oplus E_g$ where A_{1g} corresponds to the spin singlet $\Delta^{\uparrow\downarrow} - \Delta^{\downarrow\uparrow}$ with total spin 0 while the three others are spin-triplet with total spin 1. The A_{2g} one is given by $\Delta^{\uparrow\downarrow} + \Delta^{\downarrow\uparrow}$ with spin projection 0 and the E_g ones are $\Delta^{\uparrow\uparrow}$ and $\Delta^{\downarrow\downarrow}$ with spin projection ± 1. These four components are represented by Pauli matrices shown in Table I.

On the other hand, the orbital part depends in this case on the t_{2g} basis. Those transform intrinsically like two independent subsets: the xy orbital transforms like the one-dimensional $D_{xy} = B_{2g}$ irrep while the yz and zx orbitals transform like the two-dimensional $D_{yz/zx} = E_g$ irrep. In other words, the electrons states forming the Cooper pairs transform nontrivially depending on the orbital that hosts them. The orbital part of the SCOP transforms like $D_{l_1} \otimes D_{l_2}$ with three distinct possibilities:

(i) The $l_1 = l_2 = xy$ sector that involves a single component transforming like $B_{2g} \otimes B_{2g} = A_{1g}$.

(ii) The $l_1, l_2 \in \{yz, zx\}$ sector that involves four components transforming like $E_g \otimes E_g = A_{1g} \oplus A_{2g} \oplus B_{1g} \oplus B_{2g}$.

(iii) The $l_1 = xy$ and $l_2 \in \{yz, zx\}$ sectors (and vice versa), involving four components transforming like $B_{2g} \otimes E_g = E_g \otimes B_{2g} = E_g$.

The orbital basis functions written in terms of the irreps are shown in Table II. See how $E_g \otimes E_g$ is reducible. Moreover, these basis functions can be either even ^+O or odd ^-O under exchange of the two orbitals forming the pair.

Neglecting SOC makes **Δ** diagonal in spins, implying it is an eigenvector of $\hat{S}$. It is also block diagonal in the orbital basis with the three independent sectors given above. Note again that we are neglecting the wavevector dependence of the gap functions. If we were considering a nontrivial irrep in wavevector space, it would have to be multiplied by the other irreps. For example, a spin-singlet component for $xy;xy$ orbitals transforms like A_{1g} in spin-orbit basis. If, in **k** space, it transforms like the $d_{x^2-y^2}$ function that is B_{1g}, this component globally transforms like $A_{1g} \otimes B_{1g} = B_{1g}$.

With SOC.. Introducing SOC in the Hamiltonian of the noninteracting system has the effect that spin and orbital are no longer good quantum numbers at the one-particle level. As a result, an electron is in a superposition of different orbitals and spins, with coefficients depending on its wavevector. In other words, the Hamiltonian is no longer block diagonal in those spaces, although it stays diagonal in pseudospin space. Consequently, the three orbital sectors are coupled together and the gap functions involve all of the orbitals through combinations of $\hat{S}\hat{P}^*\hat{O}\hat{T}^* = -1$ contributions. All these contributions however have to globally transform like a single irrep.

In spin-orbital space, the whole space of t_{2g} orbitals transforms like $D_{t_{2g}\sigma} = (B_{2g} \oplus E_g) \otimes E_{1/2,g}$. The product $D_{t_{2g}\sigma} \otimes D_{t_{2g}}$ involved in the SCOP gives new basis functions that entangle spins and orbitals. Most of these are trivially obtained, like a singlet state in the $xy;xy$ orbitals transforms like $|xy;xy\rangle \otimes \sigma_2$, that is $A_{1g} \otimes A_{1g} = A_{1g}$. The only nontrivial basis functions are those involving the 2D irreps in both orbital and spin spaces, that is the $\{yz, zx\}$ orbitals with $\{\sigma_0, \sigma_3\}$ spins. This $E_g \otimes E_g$ product is reduced by forming

TABLE III. Nontrivial basis functions of the SCOP in spin-orbital space expressed as irreps. The orbital and spin parts are respectively defined in Tables I and II. O (S) is the parity under orbital (spin) exchange.

Irrep	Basis function	S	O
A_{1g}	$\|1+\rangle \otimes \sigma_0 + i\|2+\rangle \otimes \sigma_3$	+	+
B_{1g}	$\|1+\rangle \otimes \sigma_0 - i\|2+\rangle \otimes \sigma_3$	+	+
A_{2g}	$\|1+\rangle \otimes \sigma_3 + i\|2+\rangle \otimes \sigma_0$	+	+
B_{2g}	$\|1+\rangle \otimes \sigma_3 - i\|2+\rangle \otimes \sigma_0$	+	+
A_{1g}	$\|1-\rangle \otimes \sigma_0 + i\|2-\rangle \otimes \sigma_3$	+	−
B_{1g}	$\|1-\rangle \otimes \sigma_0 - i\|2-\rangle \otimes \sigma_3$	+	−
A_{2g}	$\|1-\rangle \otimes \sigma_3 + i\|2-\rangle \otimes \sigma_0$	+	−
B_{2g}	$\|1-\rangle \otimes \sigma_3 - i\|2-\rangle \otimes \sigma_0$	+	−

linear combinations that transform like the A_{1g}, A_{2g}, B_{1g}, and B_{2g} irreps. These combinations are given in Table III.

Although SOC couples orbitals of different sectors, the effective reduction in pseudospin space given in Eq. (23) implies the gap functions are purely intra- or inter-pseudospin. In this paper, we only study the inter-pseudospin solutions as explained in Sec. III C.

2. Time-reversal symmetry

In Ref. [127], the group theory classification for the D_{4h} space group was extended to the Shubnikov group of the second kind to include odd-frequency superconductivity. They do so by including $\hat{T}^*$, the exchange of relative time, to the symmetry operations. However, $\hat{T}^*$ is not necessarily a symmetry of the normal state, since the actual symmetry of the normal state is TR $\hat{\mathcal{T}}$. It involves all electronic degrees of freedom while $\hat{T}^*$ only affects $i\omega_n$.

As shown with two proofs in Appendix E, under $\hat{\mathcal{T}}$, the Gorkov function $\boldsymbol{F}$ transforms like

$$[\hat{\mathcal{T}}\boldsymbol{F}]^{\sigma_1\sigma_2}_{\mathbf{k}l_1l_2}(i\omega_m) = \epsilon_{\sigma_1\sigma_2}\boldsymbol{F}^{-\sigma_1-\sigma_2}_{-\mathbf{k}l_1l_2}(-i\omega_m)^* \quad (30)$$

where $\epsilon = \delta_{\sigma_1\sigma_2} - \delta_{-\sigma_1\sigma_2}$. In the ordered phase, TR symmetry is either conserved or broken by the Gorkov function, with $\hat{\mathcal{T}}\boldsymbol{F} = \pm\boldsymbol{F}$. On the other hand, $\boldsymbol{F}$ is not necessarily an eigenstate of $\hat{T}^*$ and a multiorbital state that respects TR symmetry can still exhibit the coexistence of even- and odd-frequency correlations in the presence of SOC. Our solutions to the Eliashberg equation all satisfy Eq. (30), up to a global phase discussed in Appendix E. Such a global phase has no consequence of observables.

Since SCOPs in multiorbital systems with SOC are not purely even or odd under the $\hat{T}^*$ operation, we use an in-between criterion to label states. The intraorbital components of the SCOPs are always pure in Matsubara frequencies. Thus, in the spirit of Ref. [127], we use their *SPOT* character to label irreps with the superscript + (−), given they have a ^+T (^-T) character.

V. LEADING AND SUBLEADING EIGENVECTORS

We now present solutions to the effective Eliashberg equation Eq. (23) in the inter-pseudospin channel. The *p-h* channel is dressed using the RPA vertex, as explained in Sec. III B,
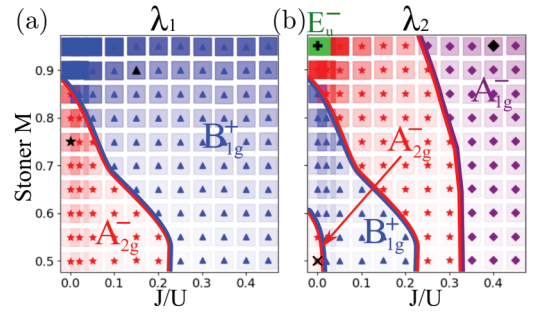

FIG. 8. Global irrep of the (a) leading and (b) first subleading eigenvectors at $T = 250$ K and for a $24 \times 24 \times 2$ **q**-grid. The parameter space is constructed as a function of the dressed parameters J/U and S^m given in Fig. 6 c). The transparency of the background square represents the size of the eigenvalue between zero and one. Notice the ▲, ★, ×, ♦, and + symbols associated to eigenvectors with global irreps B_{1g}^+, two different A_{2g}^-, A_{1g}^-, and E_u^- respectively. These specific solutions will be discussed further in the text.

at $T = 250$ K, on a $24 \times 24 \times 2$ **q**-grid and with parameters shown in Fig. 6(c). The resulting leading eigenvector symmetries in terms of global irreps are shown in Fig. 8(a) while in (b) we show the first subleading symmetries. They are labeled using irreps defined in Sec. IV B and the transparency of each square is proportional to the size of the eigenvalue, between zero and one. We find various possibilities, but only two leading instabilities. For each different irrep, we selected a point in parameter space where we will present actual gap functions in the following discussion. In particular, we identify the *SPOT* decomposition the following way: From the solution of Eq. (23) in a given parity channel, we can express it in pseudospin-orbital space using Eq. (22). We then rotate it to the spin-orbital space and apply the $\hat{S}$, $\hat{P}^*$, $\hat{O}$, and $\hat{T}^*$ operators. We find that many different *SPOT* contributions are associated to different real and imaginary parts of the spin-orbital components, although they all transform like the same unique irrep. The interference between different *SPOT* contributions lead to complex numbers with a nontrivial distribution of angles in the complex plane.

This analysis is performed for the B_{1g}^+ state in Sec. V 1 and for the A_{2g}^- in Sec. V 2. The phase diagram naturally suggests the possibility of an accidental degeneracy between these two, which could explain the experimental discrepancies. We then discuss the temperature dependence of the solutions in Sec. V 3, along with subleading candidates and reasons why we do not find some of the other SCOPs proposed for SRO in Sec. V 4.

1. The B_{1g}^+ irrep

Denoted by a ▲ in Fig. 8, the $J/U = 0.15$ and $S^m = 0.9$ parameter set has a B_{1g}^+ leading irrep. This symmetry is a prime candidate that could form an accidental degeneracy in SRO. It is usually discussed as having a purely $^-S^+P^+O^+T$ character, neglecting the entanglement of *SPOT* characters. However, SOC leads to entanglement of the electronic quantum numbers and the *SPOT* decomposition has $^-S^+P^+O^+T$, $^+S^+P^-O^+T$, and $^+S^+P^+O^-T$ characters, given in Table IV. Those can be understood by studying the real and imaginary

TABLE IV. *SPOT* decompositions of the gap functions denoted by ▲ and ★ in Fig. 8. Here, $\mathcal{P}^{SPOT}\Delta$ is the ratio of the absolute value of the projected gap function Δ for a specific *SPOT* on the total one. Each *SPOT* is specified by a color that is used in Figs. 9–12.

S	P	O	T	$\mathcal{P}^{SPOT}\Delta^{\blacktriangle}(\mathrm{B}_{1g}^{+})$	$\mathcal{P}^{SPOT}\Delta^{\star}(\mathrm{A}_{2g}^{-})$
−	+	+	+	95%	<1%
+	+	+	−	10%	81%
+	+	−	+	29%	58%
−	+	−	−	0%	<1%

parts of the spin-orbital components of $\Delta^{\blacktriangle}(\mathrm{B}_{1g}^{+})$, shown in Fig. 9(a) for the first positive and negative Matsubara frequencies. Globally, this state transforms like a single global irrep with ubiquitous even- and odd-frequency correlations, as expected in such a multiorbital system [74]. Although arguably responsible for the finite polar Kerr effect [76], these odd-frequency correlations are insufficient to explain the two-component signatures in SRO, which motivates revisiting the polar Kerr experiment under uniaxial pressure.

The intraorbital parts have $^{-}S^{+}P^{+}O^{+}T$ character. We make them real by selecting the appropriate global phase and the gap function transforms like $\hat{\mathcal{T}}\Delta = \Delta$ under TR symmetry. These components are the largest and because they are spin-singlet ^{-}S, they are characterized by the $|l;l\rangle \otimes \sigma_2$ basis functions defined in Sec. IV B. While the $xy;xy$ component transforms like A_{1g} in spin-orbital space, it transforms like a $\mathrm{B}_{1g}\ d_{x^2-y^2}$ function in **k** space, making it globally B_{1g}. The $yz;yz$ and $zx;zx$ components transform into each other and their phase difference implies that they transform like the B_{1g} orbital basis function in Table II. In **k** space, they transform like A_{1g} making them globally B_{1g}. Because of the ^{+}T character of these intraorbital components, this gap function is labeled B_{1g}^{+}.

These intraorbital components involve opposite spins. Because of SOC, the orbital sectors are coupled by spin-flip processes as follows: One of the paired xy electrons of a $xy;xy$ pair can propagate to the $\{xz, yz\}$ orbitals by flipping a spin (yet preserving pseudospin). The resulting interorbital pair involving one xy electrons with one yz or zx must now have equal spins, i.e., form a triplet pair with ^{+}S. Having a

fixed ^{+}P, there are two possible *SPOT* characters that can entangle: $^{+}S^{+}P^{-}O^{+}T$ and $^{+}S^{+}P^{+}O^{-}T$. Inspecting Fig. 9, we see that the real parts of $xy;yz$ and $yz;xy$ and imaginary parts of $xy;zx$ and $zx;xy$ have $^{+}S^{+}P^{-}O^{+}T$ character and can be expressed using the $\mathrm{B}_{1g}\ |1-\rangle \otimes \sigma_0 - i|2-\rangle \otimes \sigma_3$ basis function. On the other hand, the imaginary parts of $xy;yz$ and $yz;xy$ and real parts of $xy;zx$ and $zx;xy$ have $^{+}S^{+}P^{+}O^{-}T$ character and can be expressed using the $\mathrm{B}_{1g}\ |1+\rangle \otimes \sigma_0 - i|2+\rangle \otimes \sigma_3$ basis function. These $xy;\{yz, zx\}$ interorbital components are smaller yet similar in magnitude to the $xy;xy$ one and also transform like B_{1g}^{+}.

Moreover, the other xy electron of the initial pair can also flip its spin and propagate to $\{yz, zx\}$ orbitals. All orbital sectors are connected and the intraorbital $\Delta_{yz,yz}^{-\sigma,\sigma}$ and $\Delta_{zx,zx}^{-\sigma,\sigma}$ are the second largest components. They globally transform like the $\Delta_{xy,xy}^{\sigma,-\sigma}$ component as B_{1g}^{+} with $^{-}S^{+}P^{+}O^{+}T$ character. The interorbital components $yz;zx$ and $zx;yz$ are much smaller than the others. Their real (imaginary) parts have $^{+}S^{+}P^{+}O^{-}T$ ($^{+}S^{+}P^{-}O^{+}T$) character expressed using $[|yz;zx\rangle + |zx;yz\rangle] \otimes \sigma_1$ ($[|yz;zx\rangle - |zx;yz\rangle] \otimes \sigma_1$). The irreps associated to those components are B_{2g} (A_{2g}) in orbital space, A_{2g} (A_{2g}) in spin space and A_{1g} (B_{1g}) in **k** space, thus globally transforming like B_{1g}.

Although there are multiple *SPOT* contributions to the state, it still satisfies the TR condition (30). However, the transformation properties of individual components involve complex numbers, which means that the gap function represented by the 3×3 matrices cannot simply be written with real numbers. To illustrate this fact, we show in Fig. 10 a polar plot of the weighted distribution of phases in the complex plane of the ▲ B_{1g}^{+} gap function Fig. 9 at $i\omega_0$, on a semilog scale. It is defined by

$$\mathcal{D}(\phi) = \sum_{\mathbf{k}\mu_1\mu_2} \left|\Delta_K^{\mu_1\mu_2}\right| \text{ with } \phi \text{ in } \Delta_K^{\mu_1\mu_2} = \left|\Delta_K^{\mu_1\mu_2}\right|e^{i\phi}. \quad (31)$$

The black line corresponds to the distribution of phases when we include all the matrix elements entering the gap functions. The colored distributions are associated to a single *SPOT* characters, with colors associated to characters as in Table IV and the contours of Fig. 9. For a given *SPOT* contribution, the distribution has mostly $\phi \in \{0, \frac{\pi}{2}, \pi, \frac{3\pi}{2}\}$ angles, in other words a given SPOT contribution can be represented by purely
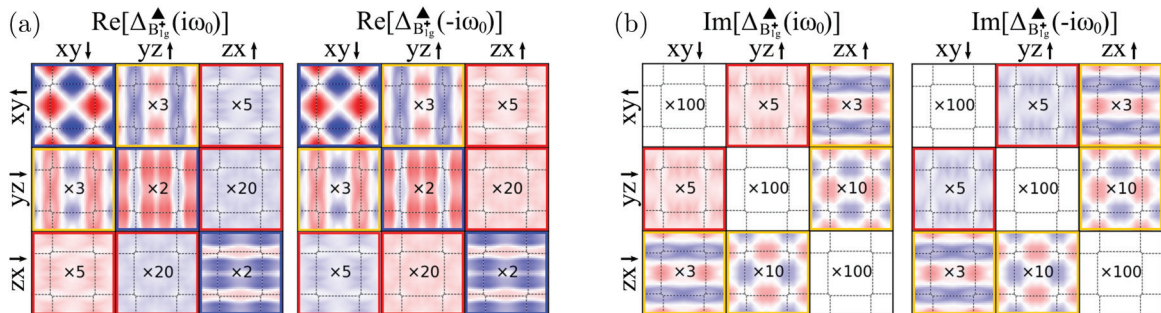

FIG. 9. (a) Real and (b) imaginary parts at the first positive $i\omega_0$ and negative $-i\omega_0$ Matsubara frequencies of the leading B_{1g}^{+} gap function denoted ▲ in Fig. 8. Each entry of a 3×3 matrix is the momentum distribution in the first Brillouin zone for $\mathrm{k}_z = 0$ and $\mathrm{k}_z = 2\pi/c$ of a component of the inter-pseudospin gap function. Colors go from -1 (blue) to 1 (red) and components were rescaled with a coefficient printed at their Γ point. The colors around the squares show the *SPOT* character of each component: blue, red, and orange correspond to $^{-}S^{+}P^{+}O^{+}T$, $^{+}S^{+}P^{+}O^{-}T$, and $^{+}S^{+}P^{-}O^{+}T$ respectively, as in Table IV.
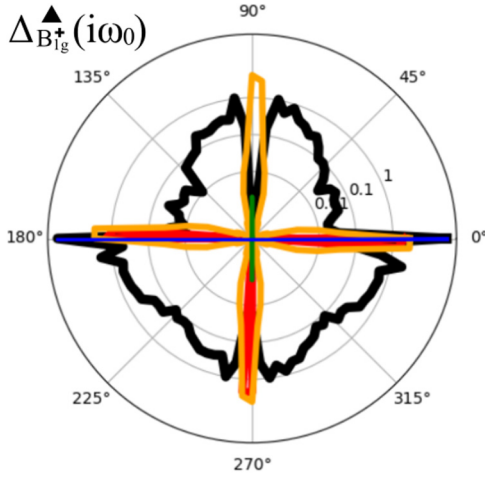
FIG. 10. Weighted distributions of the phases of the complex numbers entering the ▲ gap function at $i\omega_0$, defined in Eq. (31). The black line is associated to the total gap. The other colors are the distributions of each *SPOT* contribution of Table IV, with corresponding colors.

real or imaginary numbers. The purely imaginary ones are imposed by the C_4 symmetry operation detailed in Appendix G, acting on the spin-space of interorbital components. Including all *SPOT* contributions creates the wild phase distribution seen in black in Fig. 10. This kind of distribution emerging from the interference of different *SPOT* contributions is unavoidable in multiorbital systems with SOC. It is not clear how these phases affect physical observables.

2. The A_{2g}^- irrep

The other leading irrep in Fig. 8 is the A_{2g}^- gap function. We study the one found at $J/U = 0$ and $S^m = 0.75$ and denoted by the star (★) symbol, where its real and imaginary parts are shown in Fig. 11 for the first positive and negative Matsubara frequencies. It has $^+S^+P^+O^-T$ intraorbital components, which explains the minus superscript in our notation. This state is a generalization of regular odd-frequency to a multiorbital system where SOC leads to multiple coexisting *SPOT* contributions. In this case, the dominant characters are $^+S^+P^-O^+T$ and $^+S^+P^+O^-T$ in the proportions given in

Table IV, with negligible contributions from $^-S^+P^-O^-T$ and $^-S^+P^+O^+T$ characters.

The dominant components are intraorbital and transform like $^+S^+P^+O^-T$. If we make them real by choosing the appropriate global phase, we find that the whole gap transforms like $\hat{\mathcal{T}}\Delta = \Delta$ under TR symmetry. If instead we apply an additional $\pi/2$ phase shift, these intraorbital components are purely imaginary and the whole gap now transforms like $\hat{\mathcal{T}}\Delta = -\Delta$. This global phase invariance is detailed in Sec. IVB2.

The intraorbital $xy;xy$ component is the largest and is characterized by the $|xy;xy\rangle \otimes \sigma_1$ basis function defined in Sec. IVB1, which transforms like A_{1g} in orbital space and is a spin zero A_{2g} triplet in spin space. In **k** space, it is almost uniform, transforming like A_{1g} so that overall this component transforms like A_{2g}. The other intraorbital components are much smaller and have the same phase. They transform like $[|yz;yz\rangle + |zx;zx\rangle] \otimes \sigma_1$ in spin-orbital space and they are almost uniform in **k** space, thus they globally transform like A_{2g} as well.

Now, because the intraorbital components are ^+S for opposite spins $\sigma_1 = -\sigma_2$, a single spin-flip induced by SOC generates interorbital components that are necessarily ^+S as well. This explains why the dominant *SPOT* contributions are both triplet. Those are of the same order of magnitude as the dominant $xy;xy$ one. The real part of $xy;yz$ and imaginary part of $xy;zx$ can be expressed as the $|1+\rangle \otimes \sigma_3 + i|2+\rangle \otimes \sigma_0$ basis function with $^+S^+P^-O^+T$ character, while the imaginary part of $xy;yz$ and real part of $xy;zx$ is instead of the form $|1-\rangle \otimes \sigma_3 + i|2-\rangle \otimes \sigma_0$ with $^+S^+P^+O^-T$ character. Both of these transform like A_{2g}. Looking at the small $yz;zx$ components, their real (imaginary) parts have $^-S^+P^-O^-T$ ($^-S^+P^+O^+P$) characters. All components consistently transform like A_{2g} globally.

Again, we can look at the weighted distribution Eq. (31) of phases in the complex plane shown in Fig. 12, for all components of the gap function in black and for the individual *SPOT* contributions are shown in Fig. 11 with colors as in Table IV. In this case, most individual *SPOT* contributions have only complex phases as $\phi \in \{0, \frac{\pi}{2}, \pi, \frac{3\pi}{2}\}$, but the $^+S^+P^+O^-T$ contribution has additional interference coming from the interorbital components. We cannot explain why that is. Overall, all *SPOT* contributions again interfere, leading to a wild distribution of complex number phases for which it is
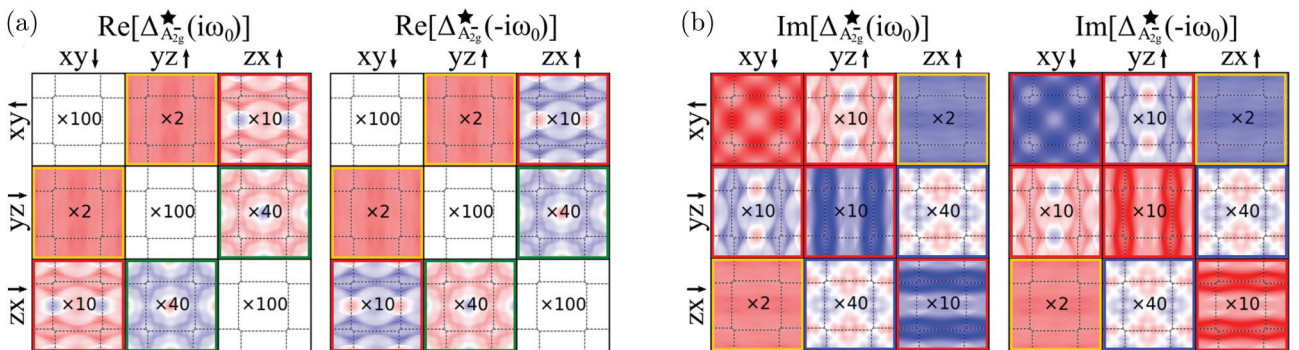

FIG. 11. (a) Real and (b) imaginary parts at the first positive and negative Matsubara frequencies of the leading A_{2g}^- gap function denoted ★ in Fig. 8. See Fig. 9 for more details of what is shown. The additional $^-S^+P^-O^-T$ component is highlighted in green.
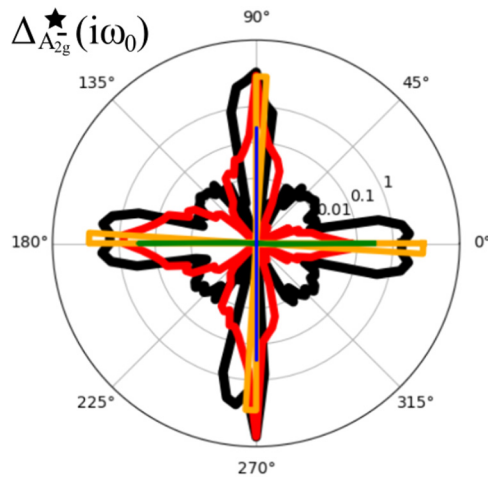
FIG. 12. Weighted distributions of the phases of the complex numbers entering the ★ gap function at $i\omega_0$. The black line is associated to the total gap. The other colors are the distributions of each *SPOT* contribution of Table IV, with corresponding colors.

FIG. 13. Eigenvalues' temperature dependence at the (a) ▲ and (b) ★ points of Fig. 8. Error bars explained in Appendix H.

not clear whether a signature can be observed in experiments, motivating further investigations.

Now, because this state has spin-triplet intraorbital components in the inter-pseudospin channel, it is expected to have nearly degenerate intra-pseudospin solutions with a similar structure. This is what unconverged calculations confirm. Because the A_{2g} character of the different components comes from the spin degrees of freedom, the intra-pseudospin solutions instead have E_g spin irreps and globally transform like two degenerate E_g^- states.

The interest in this A_{2g}^- SCOP is twofold. First, it transforms like A_{2g}, consistent with ultrasound experiments. Second, intraorbital odd-frequency SCOP are gapless at the Fermi level [66]. This property implies that their effect on the Fermi surface of SRO could be negligible enough that it has a negligible signature in specific heat. A similar behavior is expected for the even-frequency components since, being interorbital, they open gaps where the bands with the same orbital characters cross, which is mostly away from the Fermi level for different characters. Consequently, an accidental degeneracy between B_{1g}^+ and A_{2g}^- in the system at ambient pressure could appear as having two components and breaking TR symmetry. Applying uniaxial strain, one can imagine that the B_{1g}^+ acquires a larger critical temperature while the A_{2g}^- remains almost constant. As a result, one would observe a first transition when entering the B_{1g}^+ state and a second one when entering the $B_{1g}^+ \pm e^{i\phi}A_{2g}^-$, which could suddenly break TR symmetry, with a negligible signature in specific heat. Such a scenario should be further investigated.

3. Temperature dependence

While the eigenvectors of Fig. 8 have largest eigenvalues, these are lower than one, meaning that the system remains in the normal state. The assumption is that these eigenvalues are enhanced by lowering temperature and at some point become unity, signaling a phase transition. The temperature dependence of the eigenvalue is very important as a subleading
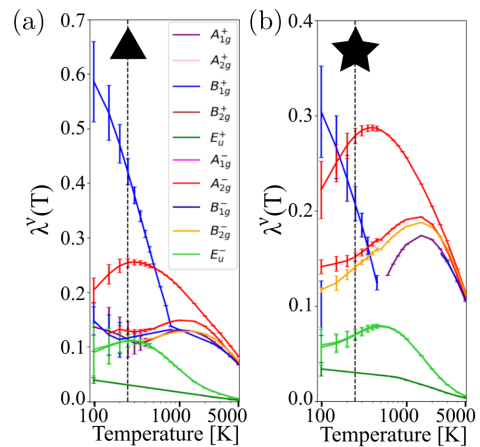
eigenvalue might rise faster than the leading one. We studied this possibility for the ▲ and ★ points of the phase diagram, which have leading eigenvectors $\Delta^{\blacktriangle}(B_{1g}^+)$ and $\Delta^{\bigstar}(A_{2g}^-)$. The results are shown in Figs. 13(a) and 13(b), respectively. The eigenvalues are very challenging to calculate at lower temperatures where the convergence in **k** points and fermionic frequencies becomes increasingly difficult. The way the error bars are obtained is explained in Appendix H.

We observe that the eigenvalues of states with odd-frequency intraorbital components, denoted by the minus superscript in our notation, are not monotonous in temperature. In other words, they have a maximal value at a finite temperature. This reentrance property has been predicted in odd-frequency superconductors and could lead to a metal-superconductor-metal transition induced by temperature [68,129]. In our case, the maxima appear at high temperatures, with eigenvalues far from unity. Because this has not been studied a lot, it is unclear whether this behavior can be avoided with better choices of interactions and normal states, leading to enhanced maximum eigenvalues at lower temperatures. Otherwise, these states might never trigger a phase transition. However, the B_{1g}^+ state behaves normally and rises as temperature is lowered, guaranteeing its importance as a potential state to form an accidental degeneracy.

4. Subleading gap functions

As the temperature dependence suggests, it is not impossible that subleading gap functions become leading when lowering temperature further. We briefly present a few of the other symmetries present in the phase diagram, denoted by the $+$, $\times$, and ♦ symbols on Fig. 8(b) and shown in Fig. 14.

At the $+$ symbol, there are both large amounts of spin and charge fluctuations, with both Stoner factors around 95%. In this parameter regime, the second and third largest eigenvalues are degenerate and transform like the E_u^- irrep. The largest component in pseudospin-orbital basis is the intraorbital $xy;xy$, classified as a $^-S^-P^+O^-T$. The second largest are the interorbital $xy;yz/zx$ ones. These gap functions are shown in Figs. 14(a) and 14(b). One can see that they are complementary, exhibiting the fact that they represent the
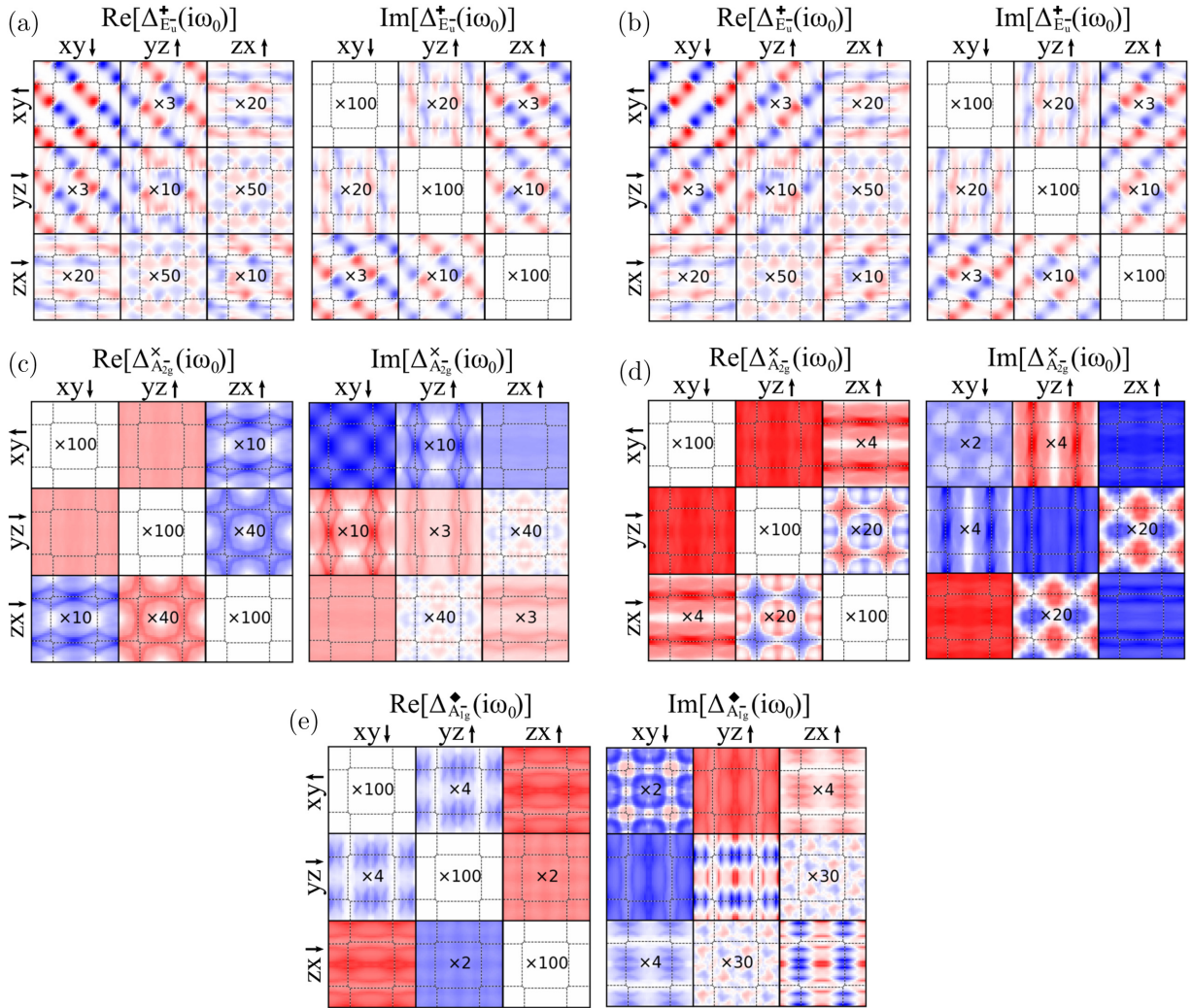
FIG. 14. Other gap functions at the points denoted by the $+$, $\times$, and $\blacklozenge$ symbols on Fig. 8. In (a) and (b), eigenvectors with second and third largest eigenvalues at the $\times$ point. They are degenerate and correspond to the two-dimensional E_u^- irrep. In (c) and (d), first and second eigenvectors at the $\blacklozenge$ point. They both transform like different A_{2g}^- irreps. In (e), second largest eigenvector at the $\blacklozenge$ point, which have A_{1g}^- symmetry. For more details about what is shown, see Fig. 9.

same two-dimensional irrep. The symmetry protected degeneracy between these states would naturally be broken under uniaxial conditions. However, they would have either zero or two temperature transitions under uniaxial strain.

At the $\times$ symbol, both the spin and charge fluctuations are relatively low around 50%. In this region of parameter space, both the first and second eigenvectors transform like A_{2g}^-, a one-dimensional irrep. They are shown in Figs. 14(c) and 14(d). These two gaps should be linearly independent. The first one has similar relative amplitudes and momentum structure as the $\Delta^\star(A_{2g}^-)$ gap function. This is expected as they are part of the same region in the phase diagram Fig. 8. The second gap is similar in structure, but the magnitude between different components is different, and most strikingly, the phase between the intraorbital $xy;xy$ component and the $yz;yz$ and $zx;zx$ ones is opposite, which makes it orthogonal to the A_{2g}^- state.

At the $\blacklozenge$ symbol, spin fluctuations are very large with a magnetic Stoner factor of 95%, while charge fluctuations are

unenhanced by correlations. At this point in parameter space, the second eigenvector transforms like the A_{1g}^- irrep, shown in Fig. 14(e). Its intraorbital components have a lot of gradients and sharp values due to extremely sharp peaks in the dressed p-h susceptibility. Equivalently important components are the uniform interorbital $xy;yz$ and $xy;zx$ ones.

We notice that all these second leading eigenvectors have odd-frequency intraorbital components. We do not find the even-frequency solutions that could have been expected for SRO. First, the $d_{zx} \pm i d_{yz}$ state that transforms like the E_g irrep and could originate from **k**-SOC [34,35] is vanishing at $k_z = 0$ and $k_z = \frac{2\pi}{c}$. To study this state, we need to include more k_z dispersion and cannot use the pseudospin reduction of the Eliashberg equation (20). However, we do not expect this state to be dominant, since the **k**-SOC obtained from DFT is negligibly small and SRO is well known to be quasi-2D [36]. Second, the odd-frequency interorbital E_g found when computing the dressed p-h susceptibility using DMFT [77] was obtained when neglecting SOC. Restoring it, the gap

function would need to involve all orbital sectors, in which case intraorbital E_g would necessarily involve a strong k_z dispersion like the $d_{zx} \pm i d_{yz}$ state or higher-order harmonics, which is improbable. It might however be compatible with the E_g^- intra-pseudospin state analogous to $\Delta^\star$. Third, although the extended s wave proposed in some studies [42–44] was found when neglecting SOC [40], it appears only in the yz/zx orbital sector because it is originating from fluctuations caused by the quasi-one-dimensional nesting vector. Again, considering strong SOC implies that all sectors are active, but the A_{1g} irrep is incompatible with the xy orbital sector due to the repulsive nature of the singlet Coulomb interaction. Fourth, various studies have proposed the $g_{xy(x^2-y^2)}$ A_{2g} state [50–53]. As a higher angular momentum version of $d_{x^2-y^2}$, this state might involve too many gradients in **k** space, thus reducing its eigenvalue.

From our results, it seems that the only state with even-frequency intraorbital components that has a large enough eigenvalue to be considered a leading eigenvector for SRO is the B_{1g}^+ state. Our calculations suggest that the other dominant states have odd-frequency intraorbital components, making this kind of state an important case that should be further studied.

VI. CONCLUSIONS

Unconventional superconductivity in strongly correlated systems is a phenomenon involving many degrees of freedom. Consequently, the space of possible order parameters is broad and identifying the right symmetry is a challenging process. In this paper, we present a general formalism to study frequency-dependent correlation-enhanced pairing, starting from realistic electronic structures that characterize the normal states of multiorbital systems with SOC. We apply it to the archetypal unconventional superconductor SRO for which the normal state is extremely well understood, while the superconducting one continues to evade clear theoretical propositions with seemingly contradicting experimental evidences.

We start by projecting DFT wave functions on a localized basis set of $4d$-t_{2g} orbitals of the Ru atom. We discuss how SOC couples orbitals with different spins, yet preserves a pseudospin symmetry for intralayer wave vectors. We use the RPA approximation to obtain dressed *p-h* susceptibilities. While SOC entangles the spin and charge channels, the magnetic and density Stoner factors remain relevant indicators of the amount of spin and charge fluctuations.

In *p-h* fluctuation mediated pairing, correlation-enhanced pairing is studied by inspecting *p-p* vertex corrections through the Eliashberg equation. It is extremely difficult to solve when considering all momenta, orbitals, spins, and frequencies, the relevant quantum numbers. Using pseudospin symmetry and Pauli principle, we map the inter-pseudospin channel to an equation that does not involve spins, thus greatly reduces the numerical costs of the Eliashberg equation.

Because of SOC, we find complex and rich SCOPs that involve all quantum numbers. The ubiquitous coexistence between even and odd contributions in the exchange of spins, relative momenta, orbitals, and relative frequencies invites us to define *SPOT* decomposition to characterize SCOPs. More-

over, we show under which irreps of the D_{4h} space group each quantum number transforms. We use the pure *SPOT* character of the intraorbital components to extend the space of irreps to include states with odd-frequency intraorbital components.

In SRO, we find two different leading symmetries to the Eliashberg equation: a B_{1g}^+ and an A_{2g}^- that have even- and odd-frequency intraorbital components, respectively. We discuss how the leading spin-orbital components naturally lead to coexistence of *SPOT* contributions due to SOC. We study the temperature dependence of these leading states and find that gap functions with odd-frequency intraorbital components have a maximum eigenvalue at a finite temperature. We also observe that SOC imposes all orbital sectors to be active, which greatly reduces possible SCOPs. The only state with even-frequency intraorbital components is the B_{1g}^+ state, while all other dominant states have odd-frequency intraorbital components. We contend that this generalized picture with extended possible SCOP symmetries is an important step in understanding completely the phenomenon of unconventional superconductivity and that it has the potential to explain the mysterious experimental signatures of SRO.

APPENDIX A: DERIVATION FROM FREE ENERGY

Consider a system ruled by the grand canonical Hamiltonian $\hat{K} = \hat{H} - \mu\hat{N}$. Each electron is characterized by a set of quantum numbers $\mathbf{1} \equiv (\mathbf{k}_1, \sigma_1, \tau_1, l_1)$ with respective labels for its momentum, spin, imaginary time, and orbital degrees of freedom. The more usual basis is in position space instead of momentum, but for our purpose, momentum is more convenient. Creation and annihilation operators for such a particle are written $\psi^\dagger(\mathbf{1})$ and $\psi(\mathbf{1})$. In systems with inversion $\hat{P}^*$ and time-reversal $\hat{\mathcal{T}}$ symmetries, superconducting pairs form between degenerate states related by $\hat{\mathcal{T}}$. Acted on $\psi/\psi^\dagger$, this operation flips momentum and spin [64]. We will consider general spin states, thus we employ a time and multiorbital generalization of the Barlian-Werthammer particle-hole spinor [130,131], leading to

$$\mathbf{\Psi}(\mathbf{1}) = \begin{pmatrix} \psi(\mathbf{1}) \\ \psi^\dagger(\mathbf{1}^*) \end{pmatrix}, \qquad \mathbf{\Psi}^\dagger(\mathbf{1}) = (\psi^\dagger(\mathbf{1})\ \psi(\mathbf{1}^*)) \quad \text{(A1)}$$

where $\mathbf{1}^* \equiv (-\mathbf{k}_1, -\sigma_1, l_1, \tau_1)$ and in this two-dimensional particle-hole (p-h) representation, we label the first and second components with indices as $\Psi_1(\mathbf{1}) \equiv \psi(\mathbf{1})$ and $\Psi_2(\mathbf{1}) \equiv \psi^\dagger(\mathbf{1}^*)$. In order to keep canonical anticommutation relations, we restrict ourselves to $k_x > 0$ so that

$$\{\Psi_\alpha(\mathbf{1}), \Psi_\beta^\dagger(\mathbf{2})\} = \delta_{\alpha\beta}\delta(\mathbf{1};\mathbf{2}), \quad \{\Psi_\alpha(\mathbf{1}), \Psi_\beta(\mathbf{2})\} = 0. \quad \text{(A2)}$$

We now consider source terms $\phi(\mathbf{1};\mathbf{2})$ that couple as follows: $\Psi_\alpha^\dagger(\mathbf{1})\phi_{\alpha\beta}(\mathbf{1};\mathbf{2})\Psi_\beta(\mathbf{2})$. In this p-h basis, ϕ_{11} and ϕ_{22} conserve the number of particles while ϕ_{12} and ϕ_{21} do not. The partition function characterizing this system including source terms is

$$Z[\phi] = \text{Tr}[T_\tau S[\phi]] \quad \text{with} \quad S[\phi] \equiv e^{-\beta \hat{K}} e^{-\Psi_{\bar{\alpha}}^\dagger(\bar{\mathbf{1}})\phi_{\bar{\alpha}\bar{\beta}}(\bar{\mathbf{1}};\bar{\mathbf{2}})\Psi_{\bar{\beta}}(\bar{\mathbf{2}})} \quad \text{(A3)}$$

with T_τ the time-ordering operator and where the bar over the quantum numbers implies that the continuous variables are integrated and the discrete ones are summed over. Similarly, the bar over the p-h indices implies summation. Above, this integration is performed in the argument of the exponential. Even if we sum over only half of the Brillouin zone, the contributions from $\mathbf{1}$ and $\mathbf{1}^*$ compensate. Moreover, each field

is independent. In other words,

$$\frac{\delta\phi_{\alpha\beta}(\mathbf{1};\mathbf{2})}{\delta\phi_{\gamma\delta}(\mathbf{3};\mathbf{4})} = \delta(\mathbf{1};\mathbf{3})\delta(\mathbf{2};\mathbf{4})\delta_{\alpha\gamma}\delta_{\beta\delta}. \quad \text{(A4)}$$

The Helmholtz free energy is $\mathcal{F}[\phi] = -\frac{1}{\beta}\ln Z[\phi]$ and the generalized Nambu Green's function in the presence of the source fields is defined as

$$G(\mathbf{1};\mathbf{2};\phi) = -\frac{1}{Z[\phi]}\text{Tr}[T_\tau S[\phi]\Psi(\mathbf{1})\Psi^\dagger(\mathbf{2})]. \quad \text{(A5)}$$

Each component of the Green's function is related to the free energy by

$$G_{\alpha\beta}(\mathbf{1};\mathbf{2};\phi) = \beta\frac{\delta\mathcal{F}[\phi]}{\delta\phi_{\beta\alpha}(\mathbf{2};\mathbf{1})} = -\frac{\delta\ln Z[\phi]}{\delta\phi_{\beta\alpha}(\mathbf{2};\mathbf{1})}$$

$$= \frac{1}{Z[\phi]}\text{Tr}\left[T_\tau S[\phi]\Psi_{\bar{\alpha}}^\dagger(\bar{\mathbf{1}})\frac{\delta\phi_{\bar{\alpha}\bar{\beta}}(\bar{\mathbf{1}};\bar{\mathbf{2}})}{\delta\phi_{\beta\alpha}(\mathbf{2};\mathbf{1})}\Psi_{\bar{\beta}}(\bar{\mathbf{2}})\right]. \quad \text{(A6)}$$

Without source terms, we recover the system's normal and anomalous Green's functions

$$G(\mathbf{1};\mathbf{2};\phi)\Big|_{\phi=0} = -\langle T_\tau \Psi(\mathbf{1})\Psi^\dagger(\mathbf{2})\rangle = \begin{pmatrix} -\langle T_\tau\psi(\mathbf{1})\psi^\dagger(\mathbf{2})\rangle & -\langle T_\tau\psi(\mathbf{1})\psi(\mathbf{2}^*)\rangle \\ -\langle T_\tau\psi^\dagger(\mathbf{1}^*)\psi^\dagger(\mathbf{2})\rangle & -\langle T_\tau\psi^\dagger(\mathbf{1}^*)\psi(\mathbf{2}^*)\rangle \end{pmatrix} \equiv \begin{pmatrix} G(\mathbf{1};\mathbf{2}) & -F(\mathbf{1};\mathbf{2}) \\ -\bar{F}(\mathbf{1};\mathbf{2}) & \bar{G}(\mathbf{1};\mathbf{2}) \end{pmatrix} \quad \text{(A7)}$$

where we define the particle-particle and hole-hole Gorkov functions F and $\bar{F}$, which vanish in the normal state, along with the particle and hole propagators G and $\bar{G}$ [77]. These two are related by

$$\bar{G}(\mathbf{1};\mathbf{2}) = -G(\mathbf{2}^*, \mathbf{1}^*). \quad \text{(A8)}$$

The equations of motion are given by $G_{\alpha\beta}^{-1}(\phi) = G_{\alpha\beta}^{0-1} - \phi_{\alpha\beta} - \Sigma_{\alpha\beta}(\phi)$ with $G_{\alpha\bar{\gamma}}G_{\bar{\gamma}\beta}^{-1} = \delta_{\alpha\beta}$ since

$$\left[\underbrace{\left(-\frac{\partial}{\partial\tau_1} - H_0 - \mu\right)\delta_{\alpha\bar{\beta}}\delta(\mathbf{1},\bar{\mathbf{2}})}_{[G_0^{-1}]_{\alpha\bar{\beta}}(\mathbf{1},\bar{\mathbf{2}})} - \Sigma_{\alpha\bar{\beta}}(\mathbf{1};\bar{\mathbf{2}};\phi) - \phi_{\alpha\bar{\beta}}(\mathbf{1};\bar{\mathbf{2}})\right]G_{\bar{\beta}\beta}(\bar{\mathbf{2}};\mathbf{2};\phi) = \delta_{\alpha\beta}\delta(\mathbf{1};\mathbf{2}) \quad \text{(A9)}$$

where H_0 are matrix elements of the Hamiltonian's noninteracting part and Σ is the self-energy, which accounts for the electronic correlations at the one-particle level.

The particle-hole and particle-particle susceptibilities are obtained from

$$\chi_{ph}(\mathbf{1};\mathbf{2};\mathbf{3};\mathbf{4}) \equiv -\beta\frac{\delta^2\mathcal{F}[\phi]}{\delta\phi_{11}(\mathbf{2};\mathbf{1})\delta\phi_{11}(\mathbf{3};\mathbf{4})}\Big|_{\phi=0}, \quad \chi_{pp}(\mathbf{1};\mathbf{2};\mathbf{3};\mathbf{4}) \equiv -\frac{\beta}{2}\frac{\delta^2\mathcal{F}[\phi]}{\delta\phi_{21}(\mathbf{2};\mathbf{1})\delta\phi_{12}(\mathbf{3};\mathbf{4})}\Big|_{\phi=0} \quad \text{(A10)}$$

where the factor $\frac{1}{2}$ in the p-p channel is necessary to avoid double counting due to the indiscernibility of electrons. These susceptibilities can be expressed as four-point correlation functions. In the normal state, we find, leaving the time-ordering operator implicit,

$$\chi_{ph}(\mathbf{1};\mathbf{2};\mathbf{3};\mathbf{4}) = \langle T_\tau\psi^\dagger(\mathbf{3})\psi(\mathbf{4})\psi^\dagger(\mathbf{2})\psi(\mathbf{1})\rangle - \langle T_\tau\psi^\dagger(\mathbf{3})\psi(\mathbf{4})\rangle\langle T_\tau\psi^\dagger(\mathbf{2})\psi(\mathbf{1})\rangle, \quad \text{(A11)}$$

$$\chi_{pp}(\mathbf{1};\mathbf{2};\mathbf{3};\mathbf{4}) = \frac{1}{2}\langle T_\tau\psi^\dagger(\mathbf{3})\psi^\dagger(\mathbf{4}^*)\psi(\mathbf{2}^*)\psi(\mathbf{1})\rangle. \quad \text{(A12)}$$

From $\frac{\delta\mathcal{G}}{\delta\phi} = -\mathcal{G}\frac{\delta\mathcal{G}^{-1}}{\delta\mathcal{G}}\mathcal{G} = 0$ and the equations of motion,

$$\frac{\delta G_{11}(\mathbf{1};\mathbf{2};\phi)}{\delta\phi_{11}(\mathbf{3};\mathbf{4})} = -G_{1\bar{\alpha}}(\mathbf{1};\bar{\mathbf{1}};\phi)\overbrace{\left[-\frac{\delta\phi_{\bar{\alpha}\bar{\beta}}(\bar{\mathbf{1}};\bar{\mathbf{2}})}{\delta\phi_{11}(\mathbf{3};\mathbf{4})} - \underbrace{\frac{\delta\Sigma_{\bar{\alpha}\bar{\beta}}(\bar{\mathbf{1}};\bar{\mathbf{2}};\phi)}{\delta G_{\bar{\gamma}\bar{\delta}}(\bar{\mathbf{3}};\bar{\mathbf{4}};\phi)}\frac{\delta G_{\bar{\gamma}\bar{\delta}}(\bar{\mathbf{3}};\bar{\mathbf{4}};\phi)}{\delta\phi_{11}(\mathbf{3};\mathbf{4})}}_{\Gamma_{\bar{\alpha}\bar{\beta}\bar{\gamma}\bar{\delta}}^{irr}(\bar{\mathbf{1}};\bar{\mathbf{2}};\bar{\mathbf{3}};\bar{\mathbf{4}};\phi)}\right]}^{\frac{\delta G_{\bar{\alpha}\bar{\beta}}^{-1}(\bar{\mathbf{1}};\bar{\mathbf{2}};\phi)}{\delta\phi_{11}(\mathbf{3};\mathbf{4})}}G_{\bar{\beta}1}(\bar{\mathbf{2}};\mathbf{2};\phi) \quad \text{(A13)}$$

$$= G(1; 3; \phi)G(4; 2; \phi) + G_{1\bar{\alpha}}(1; \bar{1}; \phi)G_{\bar{\beta}1}(\bar{2}; 2; \phi)\Gamma^{irr}_{\bar{\alpha}\bar{\beta}\bar{\gamma}\bar{\delta}}(\bar{1}; \bar{2}; \bar{3}; \bar{4}; \phi)\frac{\delta G_{\bar{\gamma}\bar{\delta}}(\bar{3}; \bar{4}; \phi)}{\delta\phi_{11}(3; 4)}. \tag{A14}$$

In this expression, we have defined the irreducible vertex Γ^{irr}. Since we are looking at instabilities from the normal state, taking the $\phi \to 0$ limit means the off-diagonal components of the Nambu Green's function vanish. Thus the following equalities and the ones with $\phi_{12} \to \phi_{21}$ are satisfied:

$$\frac{\delta G_{\alpha\alpha}(1; 2; \phi)}{\delta\phi_{12}(3, 4)}\bigg|_{\phi=0} = \frac{\delta G_{12}(1, 2; \phi)}{\delta\phi_{\beta\beta}(3, 4)}\bigg|_{\phi=0} = 0. \tag{A15}$$

By conservation of momentum and of particle number when $\phi_{12} = \phi_{21} = 0$, we have $\Gamma^{irr}_{11\gamma\delta} = \delta_{\gamma\delta}\delta_{\gamma1}\Gamma^{irr}_{1111}$. Defining the bare p-h susceptibility $\chi^0_{ph}(1; 2; 3; 4)$ as $-G(1; 3)G(4; 2)$, Eq. (A14) becomes

$$-\frac{\delta G_{11}(1; 2; \phi)}{\delta\phi_{11}(3; 4)}\bigg|_{\phi=0} = \chi^0_{ph}(1; 2; 3; 4) - \chi^0_{ph}(1; 2; \bar{1}; \bar{2})\Gamma_{ph}(\bar{1}; \bar{2}; \bar{3}; \bar{4})\frac{\delta G_{11}(\bar{3}; \bar{4}; \phi)}{\delta\phi_{11}(3; 4)}\bigg|_{\phi=0} \tag{A16}$$

$$\text{where } \Gamma_{ph}(\bar{1}; \bar{2}; \bar{3}; \bar{4}) \equiv \Gamma^{irr}_{1111}(\bar{1}; \bar{2}; \bar{3}; \bar{4}). \tag{A17}$$

The above can also be written in the form

$$\chi_{ph}(1; 2; 3; 4) = \chi^0_{ph}(1; 2; 3; 4) + \chi^0_{ph}(1; 2; \bar{1}; \bar{2})\Gamma_{ph}(\bar{1}; \bar{2}; \bar{3}; \bar{4})\chi_{ph}(\bar{3}; \bar{4}; 3; 4). \tag{A18}$$

Now looking at functional derivatives of off-diagonal components, we have

$$\frac{\delta G_{12}(1; 2; \phi)}{\delta\phi_{12}(3; 4)} = G_{11}(1; 3; \phi)G_{22}(4; 2; \phi) + G_{11}(1; \bar{1}; \phi)G_{22}(\bar{2}; 2; \phi)\Gamma^{irr}_{12\bar{\gamma}\bar{\delta}}(\bar{1}; \bar{2}; \bar{3}; \bar{4}; \phi)\frac{\delta G_{\bar{\gamma}\bar{\delta}}(\bar{3}; \bar{4}; \phi)}{\delta\phi_{12}(3, 4)}. \tag{A19}$$

Momentum and particle number conservation in the vertex when $\phi_{12} = \phi_{21} = 0$ imposes $(\bar{\gamma}, \bar{\delta}) = (1, 2)$. Replacing the hole propagator for a particle one using Eq. (A8) and defining $\chi^0_{pp}(1; 2; 3; 4)$ as $\frac{1}{2}G(1; 3)G(2^*; 4^*)$, we use the antisymmetry of the p-p susceptibility under the exchange of both particles to write

$$\chi_{pp}(1; 2; 3; 4) = \chi^0_{pp}(1; 2; 3; 4) + \chi^0_{pp}(1; 2; \bar{1}; \bar{2})\underbrace{\left[\Gamma^{irr}_{1212}(\bar{1}; \bar{2}; \bar{3}; \bar{4}) - \Gamma^{irr}_{1212}(\bar{1}; \bar{2}; \bar{4}; \bar{3})\right]}_{\Gamma_{pp}(\bar{1};\bar{2};\bar{3};\bar{4})}\chi_{pp}(\bar{3}; \bar{4}; 3; 4) \tag{A20}$$

and Γ_{pp} is defined such that it is antisymmetrized and to avoid double counting.

For normal state Green's function that are diagonal in momentum space, we have $G(1; 2) = G(1; 2)\delta_{\mathbf{k}_1, \mathbf{k}_2}$. It also satisfies time-translation symmetry. Matsubara transforming it yields

$$G^{\mu_1\mu_2}_K \equiv \int_0^\beta e^{i\omega_m\tau}G^{\mu_1\mu_2}(\mathbf{k}_1, \tau; \mathbf{k}_1, 0)\, d\tau \tag{A21}$$

where $\tau = \tau_1 - \tau_2$, while $K \equiv (\mathbf{k} = \mathbf{k}_1, i\omega_m)$ is the momentum-energy quadrivector and we use $\mu_i \equiv (\sigma_i, l_i)$ for compactness. We write the bare susceptibilities accordingly as

$$\left[\chi^0_{ph}(Q)\right]^{\mu_1\mu_2\mu_3\mu_4}_{KK'} = \int_0^\beta d\tau\, e^{(i\omega_m+i\nu_n)\tau}\int_0^\beta d\tau'\, e^{i\omega_m\tau'}\chi^0_{ph}(1; 2; 3; 4) = -\frac{1}{\beta}G^{\mu_1\mu_3}_{K+Q}G^{\mu_4\mu_2}_K\delta_{KK'}, \tag{A22}$$

$$\left[\chi^0_{pp}(Q)\right]^{\mu_1\mu_2^*\mu_3\mu_4^*}_{KK'} = \int_0^\beta d\tau\, e^{(i\omega_m+i\nu_n)\tau}\int_0^\beta d\tau'\, e^{-i\omega_m\tau'}\chi^0_{pp}(1; 2; 3; 4) = \frac{1}{2\beta}G^{\mu_1\mu_3}_{K+Q}G^{\mu_2^*\mu_4^*}_{-K}\delta_{KK'} \tag{A23}$$

where we used $\tau = \tau_1 - \tau_3$ and $\tau' = \tau_4 - \tau_2$ and $\mu^* \equiv (-\sigma, l)$. The spin σ in the latter label needs to be replaced by a pseudospin index ρ in the presence of spin-orbit coupling. The $1/\beta$ factor is associated to the Kronecker delta in Matsubara frequencies. The bare susceptibilities characterize two noninteracting particles. In the p-h channel, a particle is created at **1** (**4**) and removed at **3** (**2**). It has a frequency $i\omega_m + i\nu_n$ ($i\omega_m$) and a momentum $\mathbf{k} + \mathbf{q}$ (**k**). The vertex encodes an interaction between these particles. Since they conserve energy-momentum, we take $K_1 = K + Q$, $K_2 = K$, $K_3 = K' + Q$, and $K_4 = K'$. In the p-p channel, K' and K are changed for $-K'$ and $-K$. A number of additional relations between the vertices of both channels are derived in Appendix B. The susceptibilities read

$$[\chi_{ph}(Q)]^{\mu_1\mu_2\mu_3\mu_4}_{KK'} = \left[\chi^0_{ph}(Q)\right]^{\mu_1\mu_2\mu_3\mu_4}_{KK'} + \sum_{K''K'''}\sum_{\mu_5\ldots\mu_8}\left[\chi^0_{ph}(Q)\right]^{\mu_1\mu_2\mu_5\mu_6}_{KK''}[\Gamma_{ph}(Q)]^{\mu_5\mu_6\mu_7\mu_8}_{K''K'''}[\chi_{ph}(Q)]^{\mu_7\mu_8\mu_3\mu_4}_{K'''K'} \tag{A24}$$

$$[\chi_{pp}(Q)]^{\mu_1\mu_2\mu_3\mu_4}_{KK'} = \left[\chi^0_{pp}(Q)\right]^{\mu_1\mu_2\mu_3\mu_4}_{KK'} + \sum_{K''K'''}\sum_{\mu_5\ldots\mu_8}\left[\chi^0_{pp}(Q)\right]^{\mu_1\mu_2\mu_5\mu_6}_{KK''}[\Gamma_{pp}(Q)]^{\mu_5\mu_6\mu_7\mu_8}_{K''K'''}[\chi_{pp}(Q)]^{\mu_7\mu_8\mu_3\mu_4}_{K'''K'}. \tag{A25}$$

APPENDIX B: TWO-PARTICLE VERTICES

The completely reducible particle-hole and particle-particle vertices are given by [78]

$$\mathbf{\Gamma} = \frac{1}{2} \sum_{\substack{KK'Q \\ \mu_1...\mu_4}} [\mathbf{\Gamma}(Q)]_{K;K'}^{\mu_1\mu_2\mu_3\mu_4} \hat{c}_{K+Q}^{\dagger,\mu_1} \hat{c}_K^{\mu_2} \hat{c}_{K'}^{\dagger,\mu_4} \hat{c}_{K'+Q}^{\mu_3} \quad \text{and} \quad \mathbf{\Gamma}_P = \frac{1}{2} \sum_{\substack{KK'Q \\ \mu_1...\mu_4}} [\mathbf{\Gamma}_P(Q)]_{K;K'}^{\mu_1\mu_2\mu_3\mu_4} \hat{c}_{K+Q}^{\dagger,\mu_1} \hat{c}_{-K}^{\dagger,\mu_2} \hat{c}_{-K'}^{\mu_4} \hat{c}_{K'+Q}^{\mu_3} \tag{B1}$$

where $\mu \equiv (\sigma, l)$ with as usual spin replaced by pseudospin in the presence of SOC. Using the anticommutation relations of the c operators, one can show that inside a time-ordered product it implies the crossing relations

$$[\mathbf{\Gamma}(Q)]_{K;K'}^{\mu_1\mu_2;\mu_3\mu_4} = -[\mathbf{\Gamma}(K'-K)]_{K;K+Q}^{\mu_4\mu_2;\mu_3\mu_1} = [\mathbf{\Gamma}(-Q)]_{K'+Q;K+Q}^{\mu_4\mu_3;\mu_2\mu_1} = -[\mathbf{\Gamma}_P(K'+K+Q)]_{-K';-K}^{\mu_1\mu_4;\mu_3\mu_2}. \tag{B2}$$

The usual perturbative approach is to define irreducible vertices $\mathbf{\Gamma}^{ph}, \bar{\mathbf{\Gamma}}^{ph}, \mathbf{\Gamma}^{pp}$, which are irreducible in either the horizontal channel ($\mathbf{\Gamma}^{ph}$ and $\mathbf{\Gamma}^{pp}$) or the vertical channel ($\bar{\mathbf{\Gamma}}^{ph}$) and to construct the full vertices using the Bethe-Salpeter equations

$$[\mathbf{\Gamma}_P(Q)]_{K;K'}^{\mu_1\mu_2;\mu_3\mu_4} = [\mathbf{\Gamma}_{pp}(Q)]_{K;K'}^{\mu_1\mu_2;\mu_3\mu_4} + [\mathbf{\Gamma}_P(Q)\boldsymbol{\chi}_{pp}^0(Q)\mathbf{\Gamma}_{pp}(Q)]_{K;K'}^{\mu_1\mu_2;\mu_3\mu_4}, \tag{B3}$$

$$[\mathbf{\Gamma}(Q)]_{K;K'}^{\mu_1\mu_2;\mu_3\mu_4} = [\mathbf{\Gamma}_{ph}(Q)]_{K;K'}^{\mu_1\mu_2;\mu_3\mu_4} + [\mathbf{\Gamma}(Q)\boldsymbol{\chi}_{ph}^0(Q)\mathbf{\Gamma}_{ph}(Q)]_{K;K'}^{\mu_1\mu_2;\mu_3\mu_4}. \tag{B4}$$

Using the crossing relations (B2), one finds the Parquet equations, which can be reduced to

$$[\mathbf{\Gamma}_{ph}(Q)]_{K;K'}^{\mu_1\mu_2;\mu_3\mu_4} = [\mathbf{\Lambda}_{ph}(Q)]_{K;K'}^{\mu_1\mu_2;\mu_3\mu_4} - [\mathbf{\Phi}(K'-K)]_{K;K+Q}^{\mu_4\mu_2;\mu_3\mu_1} + [\mathbf{\Psi}(K'+K+Q)]_{-K-Q;-K}^{\mu_4\mu_1;\mu_3\mu_2}, \tag{B5}$$

$$[\mathbf{\Gamma}_{pp}(Q)]_{K;K'}^{\mu_1\mu_2;\mu_3\mu_4} = -[\mathbf{\Lambda}_{ph}(K'+K+Q)]_{-K';-K}^{\mu_1\mu_4;\mu_3\mu_2} + [\mathbf{\Phi}(K'-K)]_{-K';K+Q}^{\mu_2\mu_4;\mu_3\mu_1} - [\mathbf{\Phi}(K'+K+Q)]_{-K';-K,}^{\mu_1\mu_4;\mu_3\mu_2} \tag{B6}$$

where $\mathbf{\Lambda}_{ph}$ is the vertex. which is irreducible in all channels given by Eq. (C3) and the vertex corrections are characterized by the p-h and p-p ladder functions $\mathbf{\Phi}$ and $\mathbf{\Psi}$, respectively given by

$$[\mathbf{\Phi}(Q)]_{K;K'}^{\mu_1\mu_2;\mu_3\mu_4} = [\mathbf{\Gamma}_{ph}\boldsymbol{\chi}_{ph}\mathbf{\Gamma}_{ph}(Q)]_{K;K'}^{\mu_1\mu_2;\mu_3\mu_4} \quad \text{and} \quad [\mathbf{\Psi}(Q)]_{K;K'}^{\mu_1\mu_2;\mu_3\mu_4} = [\mathbf{\Gamma}_{pp}\boldsymbol{\chi}_{pp}\mathbf{\Gamma}_{pp}(Q)]_{K;K'}^{\mu_1\mu_2;\mu_3\mu_4}. \tag{B7}$$

In the approximation that we use, the fully reducible vertices appearing in the latter equations are replaced by, respectively, the particle-hole irreducible vertex and the particle-particle irreducible vertex.

APPENDIX C: KANAMORI VERTEX FUNCTION

In this paper, we assume that local interactions between electrons mediate unconventional superconductivity. These local correlations on individual sites labeled i are modeled by the Kanamori-Slater Hamiltonian [85], that is

$$\hat{H}_{\text{int}} = \underbrace{\sum_{il} U \hat{n}_{il}^{\uparrow} \hat{n}_{il}^{\downarrow}}_{\hat{H}_U} + \underbrace{\sum_{il_1 \neq l_2} U' \hat{n}_{il_1}^{\uparrow} \hat{n}_{il_2}^{\downarrow}}_{\hat{H}_{U'}} + \underbrace{\sum_{i\sigma l_1 \neq l_2} U'' \hat{n}_{il_1}^{\sigma} \hat{n}_{il_2}^{\sigma}}_{\hat{H}_{U''}} - \underbrace{\sum_{il_1 \neq l_2} J \hat{c}_{il_1}^{\uparrow,\dagger} \hat{c}_{il_1}^{\downarrow} \hat{c}_{il_2}^{\downarrow,\dagger} \hat{c}_{il_2}^{\uparrow}}_{\hat{H}_{\text{sf}}} + \underbrace{\sum_{il_1 \neq l_2} J' \hat{c}_{il_1}^{\uparrow,\dagger} \hat{c}_{il_1}^{\downarrow,\dagger} \hat{c}_{il_2}^{\downarrow} \hat{c}_{il_2}^{\uparrow}}_{\hat{H}_{\text{ph}}}. \tag{C1}$$

In this expression, σ and l are electronic spin and orbital respectively and U, U', and U'' are the intraorbital, opposite spin interorbital, and same spin interorbital Coulomb repulsion, respectively. J is the spin-flip (sf) term and J' the pair-hopping (ph) term. In the vertex formulation, this interacting Hamiltonian can be recast as

$$\hat{H}_{\text{int}} = \frac{1}{2} \sum_i \sum_{l_1...l_4} \sum_{\sigma_1...\sigma_4} I_{l_1 l_2; l_3 l_4}^{\sigma_1\sigma_2;\sigma_3\sigma_4} \hat{c}_{il_1}^{\sigma_1,\dagger} \hat{c}_{il_2}^{\sigma_2,\dagger} \hat{c}_{il_4}^{\sigma_4} \hat{c}_{il_3}^{\sigma_3}. \tag{C2}$$

In this formalism, $\boldsymbol{I}$ is the antisymmetrized Coulomb interaction and here it is given in the particle-particle channel. We take it as the bare particle-particle vertex $\mathbf{\Lambda}_{pp} = \boldsymbol{I}$. To rotate it to the particle-hole channel, we use the second crossing relation $[\mathbf{\Lambda}_{ph}]_{l_1 l_2 l_3 l_4}^{\sigma_1\sigma_2\sigma_3\sigma_4} = -[\mathbf{\Lambda}_{pp}]_{l_1 l_4 l_3 l_2}^{\sigma_1\sigma_4\sigma_3\sigma_2}$. Then, the bare particle-hole vertex is given by

$$[\mathbf{\Lambda}_{ph}]_{l_1 l_2 l_3 l_4}^{\sigma_1\sigma_2\sigma_3\sigma_4} = \begin{cases} U & l_1 = l_2 = l_3 = l_4 \\ U' & l_1 = l_2 \neq l_3 = l_4 \\ J & l_1 = l_3 \neq l_2 = l_4 \\ J' & l_1 = l_4 \neq l_2 = l_3 \\ U'' & l_1 = l_2 \neq l_3 = l_4 \end{cases} \Big] \begin{matrix} \sigma_1 = \sigma_2 = -\sigma_3 = -\sigma_4 \\ \\ \\ \\ - \ \sigma_1 = \sigma_2 = \sigma_3 = \sigma_4 \end{matrix} + \begin{cases} -U & l_1 = l_2 = l_3 = l_4 \\ -U' & l_1 = l_3 \neq l_2 = l_4 \\ -J & l_1 = l_2 \neq l_3 = l_4 \\ -J' & l_1 = l_4 \neq l_2 = l_3 \\ -U'' & l_1 = l_3 \neq l_2 = l_4 \end{cases} \Big] \begin{matrix} \sigma_1 = \sigma_3 = -\sigma_2 = -\sigma_4 \\ \\ \\ \\ - \ \sigma_1 = \sigma_2 = \sigma_3 = \sigma_4 \end{matrix} \tag{C3}$$
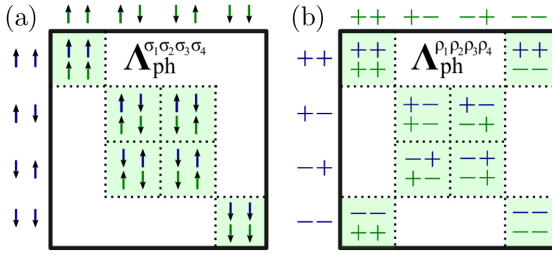
FIG. 15. Structure of the *p-h* vertex in (a) spin and (b) pseudospin basis. In each small square of this representation, the upper (lower) labels are associated to spins/pseudospins labeled 1 and 2 (3 and 4).

Half of its elements have a minus sign difference with the other half as a consequence of the first crossing relation

$$[\mathbf{\Lambda}_{ph}]^{\sigma_1\sigma_2\sigma_3\sigma_4}_{l_1l_2l_3l_4} = -[\mathbf{\Lambda}_{ph}]^{\sigma_1\sigma_3\sigma_2\sigma_4}_{l_1l_3l_2l_4}. \quad (C4)$$

Assuming the rotationally invariant formulation of this interaction, we have $U' = U - 2J$, $U'' = U - 3J$ and $J' = J$. Thus, the vertex $\mathbf{\Lambda}_{ph}[U, J]$ depends only on two parameters, the on-site Coulomb repulsion U and the Hund's coupling J and one finds the relation

$$\mathbf{\Lambda}_{ph}[U, J] = U \cdot \mathbf{\Lambda}_{ph}[1, J/U]. \quad (C5)$$

Moreover, because it preserves the spin projection, the vertex can be interpreted as an exchange of either spin 0 or 1. It is spin-diagonalized [61,79] from the $\frac{1}{2} \otimes \frac{1}{2}$ basis represented in Fig. 15(a) into the $0 \oplus 1 \sim A_{1g} \oplus A_{2g} \oplus E_g$ one in spin-space. The spin 0 (A_{1g}) bare vertex $\mathbf{\Lambda}_d$ is the density channel while the spin 1 ($A_{2g} \oplus E_g$) bare vertices $\mathbf{\Lambda}_{m,-1}$, $\mathbf{\Lambda}_{m,0} \equiv \mathbf{\Lambda}_m$ and $\mathbf{\Lambda}_{m,+1}$ are form the magnetic channels. Because of rotational invariance, the choice of axis for the projection is arbitrary and the magnetic channels are degenerate. One can check that $\mathbf{\Lambda}_{m,+1} \equiv \mathbf{\Lambda}^{\uparrow\downarrow\uparrow\downarrow} = \mathbf{\Lambda}_{m,-1} \equiv \mathbf{\Lambda}^{\downarrow\uparrow\downarrow\uparrow} = \mathbf{\Lambda}_m$ and that

$$[\mathbf{\Lambda}_{d/m}]_{l_1l_2l_3l_4} \equiv \mathbf{\Lambda}^{\uparrow\uparrow\uparrow\uparrow}_{l_1l_2l_3l_4} + / - \mathbf{\Lambda}^{\uparrow\uparrow\downarrow\downarrow}_{l_1l_2l_3l_4} \quad (C6)$$

$$= \begin{cases} 2U' - J / - J & l_1 = l_2 \neq l_3 = l_4 \\ -U' + 2J / - U' & l_1 = l_3 \neq l_2 = l_4 \\ J' / - J' & l_1 = l_4 \neq l_2 = l_3 \\ U / - U & l_1 = l_2 = l_3 = l_4 \\ 0 & \text{otherwise.} \end{cases} \quad (C7)$$

Writing the *p-h* vertex in the pseudospin basis introduces off-block diagonal elements, for example the diagram of Fig. 7 in the main text. Its structure in this basis is represented in Fig. 15(b).

APPENDIX D: CONNECTION BETWEEN THE GENERAL GREEN'S FUNCTIONS AND THE GREEN'S FUNCTIONS IN MODEL SPACE

The general Matsubara Green's function of a system in thermodynamic equilibrium is given by

$$G^{\sigma_1\sigma_2}(\mathbf{r}_1, \mathbf{r}_2, \tau) \equiv -\langle T_\tau \hat{\mathbf{\Psi}}^{\sigma_1}(\mathbf{r}_1, \tau)\hat{\mathbf{\Psi}}^{\sigma_2,\dagger}(\mathbf{r}_2)\rangle \quad (D1)$$

where $\hat{\mathbf{\Psi}}$ is a field operator and $\hat{A}(\tau) \equiv e^{H\tau}\hat{A}e^{-H\tau}$. Note that the hat distinguishes this operator from the Nambu spinor of Appendix A. We follow the derivations of Ref. [132]. Using

the relation $G(\mathbf{r}_1, \mathbf{r}_2) = \frac{1}{N}\sum_{\mathbf{R}_0} G(\mathbf{r}_1 + \mathbf{R}_0, \mathbf{r}_2 + \mathbf{R}_0)$ for $\mathbf{R}_0$ a translational vector of the unit cell, the Fourier transform leads to

$$G^{\sigma_1\sigma_2}_{\mathbf{Q}\mathbf{Q}'}(\mathbf{q}, \tau)$$
$$= \frac{1}{V} \int d\mathbf{r}_1 d\mathbf{r}_2 e^{-i(\mathbf{q}+\mathbf{Q})\cdot\mathbf{r}_1}G^{\sigma_1\sigma_2}(\mathbf{r}_1, \mathbf{r}_2, \tau)e^{i(\mathbf{q}+\mathbf{Q}')\cdot\mathbf{r}_2} \quad (D2)$$

where $\mathbf{q}$ is taken within the first Brillouin zone and $\mathbf{Q}$, $\mathbf{Q}'$ are reciprocal lattice vectors.

For an interaction well defined in an atomic-like orbital basis set $\{\phi^\sigma_{\mathbf{R}_il}(\mathbf{r})\}$ where l and σ are orbital and spin indices respectively and $\mathbf{R}_i$ is the position of the *i*th atom, it is suitable to expand the field operator in this basis with destruction operators ψ as

$$\hat{\mathbf{\Psi}}^\sigma(\mathbf{r}) = \sum_{\mathbf{R}_il} \phi^\sigma_{\mathbf{R}_il}(\mathbf{r})\psi^\sigma_{\mathbf{R}_il}. \quad (D3)$$

Defining one-body oscillator matrix elements

$$O^{\sigma_1}_{\mathbf{R}_1l_1}(\mathbf{q}) = \frac{1}{\sqrt{V}} \int d\mathbf{r}_1 \, e^{-i\mathbf{q}\cdot\mathbf{r}_1}\phi^{\sigma_1}_{\mathbf{R}_1l_1}(\mathbf{r}_1), \quad (D4)$$

we can write

$$G^{\sigma_1\sigma_2}_{\mathbf{Q}\mathbf{Q}'}(\mathbf{q}, \tau) = -\sum_{l_1l_2\mathbf{R}_1\mathbf{R}_2} O^{\sigma_1}_{\mathbf{R}_1l_1}(\mathbf{q}+\mathbf{Q})$$
$$\times \langle T_\tau \psi^{\sigma_1}_{\mathbf{R}_1l_1}(\tau)\psi^{\sigma_2,\dagger}_{\mathbf{R}_2l_2}\rangle O^{\sigma_2,*}_{\mathbf{R}_2l_2}(\mathbf{q}+\mathbf{Q}'). \quad (D5)$$

Introducing Fourier transforms

$$\psi^\sigma_{\mathbf{R}l} = \frac{1}{\sqrt{N}} \sum_{\mathbf{k}} e^{i\mathbf{k}\cdot\mathbf{R}}\psi^\sigma_{\mathbf{k}l} \quad \text{and} \quad (D6)$$

$$O^\sigma_{\mathbf{k}l}(\mathbf{q}) = \frac{1}{\sqrt{N}} \sum_{\mathbf{R}} e^{i\mathbf{k}\cdot\mathbf{R}}O^\sigma_{\mathbf{R}l}(\mathbf{q}), \quad (D7)$$

one has

$$G^{\sigma_1\sigma_2}_{\mathbf{Q}\mathbf{Q}'}(\mathbf{q}) = \sum_{l_1l_2\mathbf{k}\mathbf{k}'} O^{\sigma_1}_{\mathbf{k}l_1}(\mathbf{q}+\mathbf{Q})G^{\sigma_1\sigma_2}_{\mathbf{k}\mathbf{k}'l_1l_2}O^{\sigma_2,*}_{\mathbf{k}'l_2}(\mathbf{q}+\mathbf{Q}') \quad (D8)$$

where there τ dependence was omitted and

$$G^{\sigma_1\sigma_2}_{\mathbf{k}\mathbf{k}'l_1l_2}(\tau) \equiv -\langle T_\tau \psi^{\sigma_1}_{\mathbf{k}l_1}(\tau)\psi^{\sigma_2,\dagger}_{\mathbf{k}'l_2}\rangle. \quad (D9)$$

is the Green's function in the model space. The oscillator matrix elements are needed to make contact with observables such as the local density, but for calculations of the Green's function in the model space with the model Hamiltonian, they are not necessary. For detailed arguments on the relation between observable susceptibilities and susceptibilities calculated in the model space, see Ref. [132]. This is particularly important for nonsymmorphic groups.

Similarly, the Gorkov (or anomalous Green's) functions of a stable system are defined as

$$F^{\sigma_1\sigma_2}(\mathbf{r}_1, \mathbf{r}_2, \tau) \equiv \langle T_\tau \hat{\mathbf{\Psi}}^{\sigma_1}(\mathbf{r}_1, \tau)\hat{\mathbf{\Psi}}^{\sigma_2}(\mathbf{r}_2)\rangle \quad \text{and} \quad (D10)$$

$$\bar{F}^{\sigma_1\sigma_2}(\mathbf{r}_1, \mathbf{r}_2, \tau) \equiv \langle T_\tau \hat{\mathbf{\Psi}}^{\sigma_2,\dagger}(\mathbf{r}_2, \tau)\hat{\mathbf{\Psi}}^{\sigma_1,\dagger}(\mathbf{r}_1)\rangle. \quad (D11)$$

Following the same procedure as for the normal Green's function, we find

$$F_{QQ'}^{\sigma_1\sigma_2}(\mathbf{q}) = \sum_{l_1 l_2 \mathbf{k}\mathbf{k}'} O_{\mathbf{k}l_1}^{\sigma_1}(\mathbf{q}+\mathbf{Q}) F_{\mathbf{k}\mathbf{k}'l_1 l_2}^{\sigma_1\sigma_2} O_{\mathbf{k}'l_2}^{\sigma_2}(-\mathbf{q}-\mathbf{Q}') \quad \text{and}$$

(D12)

$$\bar{F}_{QQ'}^{\sigma_1\sigma_2}(\mathbf{q}) = \sum_{l_1 l_2 \mathbf{k}\mathbf{k}'} O_{\mathbf{k}'l_2}^{\sigma_2,*}(-\mathbf{q}-\mathbf{Q}) \bar{F}_{\mathbf{k}\mathbf{k}'l_1 l_2}^{\sigma_1\sigma_2} O_{\mathbf{k}l_1}^{\sigma_1,*}(\mathbf{q}+\mathbf{Q}') \quad \text{(D13)}$$

where

$$F_{\mathbf{k}\mathbf{k}'l_1 l_2}^{\sigma_1\sigma_2}(\tau) \equiv F_{\mathbf{k}\mathbf{k}'}^{\mu_1\mu_2}(\tau) \equiv \langle T_\tau \psi_{\mathbf{k}}^{\mu_1}(\tau)\psi_{\mathbf{k}'}^{\mu_2}\rangle, \qquad \text{(D14)}$$

$$\bar{F}_{\mathbf{k}\mathbf{k}'l_1 l_2}^{\sigma_1\sigma_2}(\tau) \equiv \bar{F}_{\mathbf{k}\mathbf{k}'}^{\mu_1\mu_2}(\tau) \equiv \langle T_\tau \psi_{\mathbf{k}'}^{\mu_2,\dagger}(\tau)\psi_{\mathbf{k}}^{\mu_1,\dagger}\rangle. \qquad \text{(D15)}$$

APPENDIX E: PROPERTIES OF MODEL GREEN'S FUNCTIONS

In this paper, we consider a local model Hamiltonian that is invariant under the crystal translation symmetry, which allows to simply take $\mathbf{k} = \mathbf{k}'$.

In the presence of spin-orbit coupling, it is useful to employ spinors $\Psi_{\mathbf{k}l}^\dagger(\tau) \equiv (\psi_{\mathbf{k}l}^{\uparrow,\dagger}(\tau) \quad \psi_{\mathbf{k}l}^{\downarrow,\dagger}(\tau))$ and electrons can propagate flipping spins. Again, this spinor is different from the Nambu spinor defined in Appendix A. The probability amplitude is related to the Green function propagator

$$G_{\mathbf{k}l_1 l_2}^{\sigma_1\sigma_2}(\tau) = -\langle T_\tau [\Psi_{\mathbf{k}l_1}(\tau)\Psi_{\mathbf{k}l_2}^\dagger]^{\sigma_1\sigma_2}\rangle. \qquad \text{(E1)}$$

Applying complex conjugation on each side, we find the relation

$$G_{\mathbf{k}}^{\mu_1\mu_2}(\tau)^* = G_{\mathbf{k}}^{\mu_2\mu_1}(\tau) \qquad \text{(E2)}$$

where $\mu_i \equiv (\sigma_i, l_i)$.

For a symmetry of the system characterized by the operator $\hat{S}$, the matrix element of Eq. (E1) is equal to

$$[\hat{S}G]_{\mathbf{k}l_1 l_2}(\tau) = -\langle T_\tau S^{-1}\Psi_{\mathbf{k}l_1}(\tau)\Psi_{\mathbf{k}l_2}^\dagger S\rangle. \qquad \text{(E3)}$$

For time-reversal symmetry, $S = \mathcal{T} = iK\sigma_y$ with σ_y the second Pauli matrix in spin-space and K is the right-side conjugation operator, which acts as $\langle K^{-1}\mathcal{O}K\rangle = \langle \mathcal{O}^{\dagger*}\rangle$. Thus

$$[\hat{\mathcal{T}}G]_{\mathbf{k}l_1 l_2}(\tau) = -\langle T_\tau \sigma_y[\Psi_{\mathbf{k}l_2}^*(\tau)\Psi_{\mathbf{k}l_1}^{\dagger*}]\sigma_y\rangle. \qquad \text{(E4)}$$

Using $[\sigma_y A\sigma_y]^{\sigma_1\sigma_2} = \epsilon_{\sigma_1\sigma_2}A^{-\sigma_1-\sigma_2}$ with $\epsilon_{\sigma_1\sigma_2} \equiv \delta_{\sigma_1\sigma_2} - \delta_{\sigma_1-\sigma_2}$ and $\psi_{\mathbf{k}l}^{\sigma*} = \psi_{-\mathbf{k}l}^{-\sigma}$ where orbitals are taken to be time-reversal invariant [133], we find

$$[\hat{\mathcal{T}}G]_{\mathbf{k}}^{\mu_1\mu_2}(\tau) = \epsilon_{\sigma_1\sigma_2}G_{-\mathbf{k}}^{\mu_2^*\mu_1^*}(\tau), \qquad \text{(E5)}$$

where $\mu^* \equiv (-\sigma, l)$.

Given that spins are invariant under inversion symmetry $\hat{S} = \hat{I}$, systems with $\hat{I}$ and orbitals that are even under $\hat{I}$ satisfy

$$G_{\mathbf{k}}^{\mu_1\mu_2}(\tau) = G_{-\mathbf{k}}^{\mu_1\mu_2}(\tau). \qquad \text{(E6)}$$

Transforming from imaginary time τ to Matsubara frequencies ω_m, complex conjugation Eq. (E2), time-reversal Eq. (E5) and inversion symmetry Eq. (E6) become respectively

$$G_{\mathbf{k}}^{\mu_1\mu_2}(i\omega_m) = G_{\mathbf{k}}^{\mu_2\mu_1}(-i\omega_m)^* \qquad \text{(E7)}$$

$$= \epsilon_{\sigma_1\sigma_2}G_{-\mathbf{k}}^{\mu_2^*\mu_1^*}(i\omega_m) \qquad \text{(E8)}$$

$$= G_{-\mathbf{k}}^{\mu_1\mu_2}(i\omega_m). \qquad \text{(E9)}$$

We write the Green's function as $G_{Kl_1 l_2}^{\mu_1\mu_2} \equiv G_{\mathbf{k}}^{\mu_1\mu_2}(i\omega_m)$ with the fermionic four-momentum $K \equiv (\mathbf{k}, i\omega_m)$.

Without magnetic field or applied current, the composite bosons described by the Gorkov function usually favours a vanishing center of mass momentum, which leads to $\mathbf{k}' = -\mathbf{k}$. We define

$$F_{\mathbf{k}}^{\mu_1\mu_2}(\tau) \equiv \langle T_\tau \Psi_{\mathbf{k}}^{\mu_1}(\tau)\Psi_{-\mathbf{k}}^{\mu_2}\rangle \quad \text{and} \qquad \text{(E10)}$$

$$\bar{F}_{\mathbf{k}}^{\mu_1\mu_2}(\tau) \equiv \langle T_\tau \Psi_{-\mathbf{k}}^{\mu_2,\dagger}(\tau)\Psi_{\mathbf{k}}^{\mu_1,\dagger}\rangle. \qquad \text{(E11)}$$

We find relations analogous to those found above for the normal Green's function for Pauli, complex conjugation and time-reversal operation, respectively

$$F_{\mathbf{k}}^{\mu_1\mu_2}(i\omega_m) = -F_{-\mathbf{k}}^{\mu_2\mu_1}(-i\omega_m), \qquad \text{(E12)}$$

$$F_{\mathbf{k}}^{\mu_1\mu_2}(i\omega_m)^* = \bar{F}_{\mathbf{k}}^{\mu_1\mu_2}(-i\omega_m), \quad \text{and} \qquad \text{(E13)}$$

$$[\hat{\mathcal{T}}F]_{\mathbf{k}}^{\mu_1\mu_2}(i\omega_m) = \epsilon_{\sigma_1\sigma_2}\bar{F}_{-\mathbf{k}}^{\mu_1^*\mu_2^*}(i\omega_m). \qquad \text{(E14)}$$

Combining these last two gives

$$[\hat{\mathcal{T}}F]_{\mathbf{k}}^{\mu_1\mu_2}(i\omega_m) = \epsilon_{\sigma_1\sigma_2}F_{-\mathbf{k}}^{\mu_1^*\mu_2^*}(-i\omega_m)^*. \qquad \text{(E15)}$$

Using the fact that field operators ψ can be multiplied by a global phase $e^{-i\frac{\delta}{2}}$, we can also work with $\tilde{F} = e^{-i\delta}F$ so that in this gauge, time-reversal symmetry becomes

$$\left[\hat{\mathcal{T}}\tilde{F}\right]_{\mathbf{k}}^{\mu_1\mu_2}(i\omega_m) = e^{2i\delta}\epsilon_{\sigma_1\sigma_2}\tilde{F}_{-\mathbf{k}}^{\mu_1^*\mu_2^*}(-i\omega_m)^*. \qquad \text{(E16)}$$

Our solutions to the linearized Eliashberg equation satisfy the above equation with $\delta = 0$. The eigenvectors have components that pick up phases that may differ depending on quantum numbers (components of the eigenvectors) so that there is no way to choose a global phase that would set all elements of the eigenvectors to have the same phase.

1. Other proof for time-reversal

Here is another proof of Eq. (E15). We start from the spectral weight in the Nambu representation, given by

$$A(\mathbf{k}, t) = \begin{bmatrix} \langle\{\Psi_1(\mathbf{k}, t), \Psi_1^\dagger(\mathbf{k})\}\rangle & \langle\{\Psi_1(\mathbf{k}, t), \Psi_2^\dagger(\mathbf{k})\}\rangle \\ \langle\{\Psi_2(\mathbf{k}, t), \Psi_1^\dagger(\mathbf{k})\}\rangle & \langle\{\Psi_2(\mathbf{k}, t), \Psi_2^\dagger(\mathbf{k})\}\rangle \end{bmatrix}. \qquad \text{(E17)}$$

We look at the 12 component and write spins and orbitals indices

$$A_{12}^{\mu_1\mu_2}(\mathbf{k}, t) = \langle\{\psi_{\mathbf{k}}^{\mu_1}(t), \psi_{-\mathbf{k}}^{\mu_2^*}\}\rangle. \qquad \text{(E18)}$$

Upon complex conjugation it becomes

$$A_{12}^{\mu_1\mu_2}(\mathbf{k}, t)^* = \langle\{\psi_{-\mathbf{k}}^{\mu_2^*\dagger}, \psi_{\mathbf{k}}^{\mu_1\dagger}(t)\}\rangle. \qquad \text{(E19)}$$

Applying time-reversal

$$\hat{\mathcal{T}}[A_{12}^{\mu_1\mu_2}(\mathbf{k}, t)] = \langle\{\Theta\psi_{-\mathbf{k}}^{\mu_2^*,\dagger}\Theta^{-1}, \Theta\psi_{\mathbf{k}}^{\mu_1,\dagger}(t)\Theta^{-1}\}\rangle$$

$$= \epsilon_{\sigma_1\sigma_2}\langle\{\psi_{\mathbf{k}}^{\mu_2,\dagger}, \psi_{-\mathbf{k}}^{\mu_1,\dagger}(-t)\}\rangle. \qquad \text{(E20)}$$

Comparing the last two equations, we have

$$\hat{\mathcal{T}}[A_{12}^{\mu_1\mu_2}(\mathbf{k}, t)] = \epsilon_{\sigma_1\sigma_2}A_{12}^{\mu_1^*\mu_2^*}(-\mathbf{k}, -t)^*. \qquad \text{(E21)}$$

From this point of view, time-reversal symmetry takes a simple form, namely time-reversal symmetry is satisfied if

$$A_{12}^{\mu_1\mu_2}(\mathbf{k}, t) = \epsilon_{\sigma_1\sigma_2} A_{12}^{\mu_1^*\mu_2^*}(-\mathbf{k}, -t)^*, \tag{E22}$$

which is similar to what one would require from wave functions. The above does not require that $A_{12}^{\mu_1\mu_2}(\mathbf{k}, t)$ be real. Fourier transforming back to space however, if time-reversal is satisfied $A_{12}^{\mu_1\mu_2}(\mathbf{r}, 0)$ is real when the spins are identical, or pure imaginary if the spins are anti-parallel (assuming throughout that the orbitals are invariant under time-reversal). In other words, for a given spin configuration, there is a global phase that can make $A_{12}^{\mu_1\mu_2}(\mathbf{r}, 0)$ real. However, seen as a matrix in the spin-indices, there is no way that matrix can be made purely real with a global phase.

How this translates in frequency is less familiar, but is not difficult to find. Using

$$\int dt\, e^{i\omega t} f^*(-t) = f^*(\omega), \tag{E23}$$

we have

$$\hat{\mathcal{T}}\left[A_{12}^{\mu_1\mu_2}(\mathbf{k}, \omega)\right] = \epsilon_{\sigma_1\sigma_2} A_{12}^{\mu_1^*\mu_2^*}(-\mathbf{k}, \omega)^*. \tag{E24}$$

We can also obtain the Gorkov function in Matsubara frequency as follows:

$$\mathcal{G}_{12}(\mathbf{k}, i\omega_n) \equiv F_{\mathbf{k}}^{\mu_1\mu_2}(i\omega_n) = \int \frac{d\omega}{2\pi} \frac{A_{12}^{\mu_1\mu_2}(\mathbf{k}, \omega)}{i\omega_n - \omega}. \tag{E25}$$

We thus recover our previous results Eq. (E15) or Eq. (30) since

$$\hat{\mathcal{T}} F_{\mathbf{k}}^{\mu_1\mu_2}(i\omega_n) = \epsilon_{\sigma_1\sigma_2} \int \frac{d\omega}{2\pi} \frac{A_{12}^{\mu_1^*\mu_2^*}(-\mathbf{k}, \omega)^*}{i\omega_n - \omega} \tag{E26}$$

$$= \epsilon_{\sigma_1\sigma_2} F_{-\mathbf{k}}^{\mu_1^*\mu_2^*}(-i\omega_n)^*. \tag{E27}$$

Note that $F_{\mathbf{k}}^{\mu_1\mu_2}(i\omega_n)$ does not need to be real, nor to be even or odd in frequency to satisfy this equation.

However, in the presence of time-reversal symmetry, the usual singlet combination $F_{\mathbf{k}}^{\sigma,-\sigma}(i\omega_n) - F_{\mathbf{k}}^{-\sigma,\sigma}(i\omega_n)$ for a single real orbital is even in Matsubara frequency when there is also inversion symmetry since

$$\hat{\mathcal{T}} F_{\mathbf{k}}^{\sigma,-\sigma}(i\omega_n) - \hat{\mathcal{T}} F_{\mathbf{k}}^{-\sigma,\sigma}(i\omega_n) \tag{E28}$$

$$= F_{-\mathbf{k}}^{\sigma,-\sigma}(-i\omega_n) - F_{-\mathbf{k}}^{-\sigma,\sigma}(-i\omega_n). \tag{E29}$$

This is the familiar BCS result.

APPENDIX F: PROPERTIES OF SUSCEPTIBILITIES

Within the RPA approximation, an element of the bare susceptibility in the particle-hole channel is given by

$$\left[\tilde{\chi}_{ph}^0(Q)\right]^{\mu_1\mu_2\mu_3\mu_4} \equiv -\left(\frac{k_B T}{N}\right) \sum_K G_{K+Q}^{\mu_1\mu_3} G_K^{\mu_4\mu_2} \tag{F1}$$

where $Q \equiv (\mathbf{q}, i\nu_n)$ is a bosonic four-momentum. Because of the sum over fermionic four-momentum, one can show it equals

$$\left[\tilde{\chi}_{ph}^0(-Q)\right]^{\mu_4\mu_3\mu_2\mu_1}. \tag{F2}$$
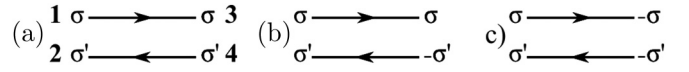
FIG. 16. Three categories of diagrams representing bare particle-hole susceptibilities. They are characterized by having (a) zero, (b) one, and (c) two spin-flips where the spin $\bar{\sigma} = -\sigma$.

Using the property of Green's functions under complex conjugation Eq. (E7), we have

$$\left[\tilde{\chi}_{ph}^0(\mathbf{q}, i\nu_n)\right]^{\mu_1\mu_2\mu_3\mu_4} = \left[\tilde{\chi}_{ph}^0(\mathbf{q}, -i\nu_n)\right]^{\mu_3\mu_4\mu_1\mu_2*} \tag{F3}$$

and with time-reversal and inversion Eq. (E9), one can show that

$$\left[\tilde{\chi}_{ph}^0(Q)\right]^{\mu_1\mu_2\mu_3\mu_4} = \left[\tilde{\chi}_{ph}^0(-Q)\right]^{\mu_1\mu_2\mu_3\mu_4}. \tag{F4}$$

Using time reversal symmetry Eq. (E8) leads to the following relations:

$$\begin{aligned}
\left[\tilde{\chi}_{ph}^0\right]^{\mu_1\mu_2\mu_3\mu_4} &= \epsilon_{\sigma_1\sigma_3} \left[\tilde{\chi}_{ph}^0\right]^{\mu_3^*\mu_2\mu_1^*\mu_4} \\
&= \epsilon_{\sigma_2\sigma_4} \left[\tilde{\chi}_{ph}^0\right]^{\mu_1\mu_4^*\mu_3\mu_2^*} \\
&= \epsilon_{\sigma_1\sigma_3}\epsilon_{\sigma_2\sigma_4} \left[\tilde{\chi}_{ph}^0\right]^{\mu_3^*\mu_4^*\mu_1^*\mu_2^*},
\end{aligned} \tag{F5}$$

where the Q dependence is implicit.

Time-reversal symmetry then connects different spin-sectors into three categories, diagrammatically represented on Fig. 16. The first one has no spin-flips (a) and satisfies

$$\left[\tilde{\chi}_{ph}^0\right]_{l_1l_2l_3l_4}^{\sigma\sigma\sigma\sigma} = \left[\tilde{\chi}_{ph}^0\right]_{l_3l_2l_1l_4}^{\bar{\sigma}\sigma\bar{\sigma}\sigma} = \left[\tilde{\chi}_{ph}^0\right]_{l_1l_4l_3l_2}^{\sigma\bar{\sigma}\sigma\bar{\sigma}} = \left[\tilde{\chi}_{ph}^0\right]_{l_3l_4l_1l_2}^{\bar{\sigma}\bar{\sigma}\bar{\sigma}\bar{\sigma}}, \tag{F6}$$

the second has one spin-flip (b) with

$$\left[\tilde{\chi}_{ph}^0\right]_{l_1l_2l_3l_4}^{\sigma\sigma\sigma\bar{\sigma}} = \left[\tilde{\chi}_{ph}^0\right]_{l_3l_2l_1l_4}^{\bar{\sigma}\sigma\bar{\sigma}\bar{\sigma}} = -\left[\tilde{\chi}_{ph}^0\right]_{l_1l_4l_3l_2}^{\sigma\bar{\sigma}\sigma\sigma} = -\left[\tilde{\chi}_{ph}^0\right]_{l_3l_4l_1l_2}^{\bar{\sigma}\bar{\sigma}\bar{\sigma}\sigma} \tag{F7}$$

and the last category has two spin-flips (c) with

$$\left[\tilde{\chi}_{ph}^0\right]_{l_1l_2l_3l_4}^{\sigma\sigma\bar{\sigma}\bar{\sigma}} = -\left[\tilde{\chi}_{ph}^0\right]_{l_3l_2l_1l_4}^{\sigma\sigma\bar{\sigma}\bar{\sigma}} = -\left[\tilde{\chi}_{ph}^0\right]_{l_1l_4l_3l_2}^{\sigma\sigma\bar{\sigma}\bar{\sigma}} = \left[\tilde{\chi}_{ph}^0\right]_{l_3l_4l_1l_2}^{\sigma\sigma\bar{\sigma}\bar{\sigma}}. \tag{F8}$$

The particle-particle bare susceptibility is given by

$$\left[\chi_{pp}^0(Q)\right]_{KK'}^{\mu_1\mu_2\mu_3\mu_4} = \frac{1}{2\beta} G_{K+Q}^{\mu_1\mu_3} G_{-K}^{\mu_2\mu_4} \delta_{KK'}. \tag{F9}$$

In spin and charge fluctuation-mediated superconductivity, it only involves $Q = 0$ in Eq. (16) and we change notation for $\chi_{pp}^0(K)$. The following relations hold from the definition and from the property of Green's functions under complex conjugation Eq. (E7):

$$\left[\chi_{pp}^0(K)\right]^{\mu_1\mu_2\mu_3\mu_4} = \left[\chi_{pp}^0(-K)\right]^{\mu_2\mu_1\mu_4\mu_3} \tag{F10}$$

$$= \left[\left[\chi_{pp}^0(K^*)\right]^{\mu_3\mu_4\mu_1\mu_2}\right]^*, \tag{F11}$$

where $K^* \equiv (\mathbf{k}, -i\omega_n)$. Again, using time reversal Eq. (E8) and inversion Eq. (E9) leads to

$$\begin{aligned}
\left[\chi_{pp}^0(K)\right]^{\mu_1\mu_2\mu_3\mu_4} &= \epsilon_{\sigma_1\sigma_3} \left[\chi_{pp}^0(K)\right]^{\mu_3^*\mu_2\mu_1^*\mu_4} \\
&= \epsilon_{\sigma_2\sigma_4} \left[\chi_{pp}^0(K)\right]^{\mu_1\mu_4^*\mu_3\mu_2^*} \\
&= \epsilon_{\sigma_1\sigma_3}\epsilon_{\sigma_2\sigma_4} \left[\chi_{pp}^0(K)\right]^{\mu_3^*\mu_4^*\mu_1^*\mu_2^*}. \tag{F12}
\end{aligned}$$

TABLE V. Space group symmetry generators g and corresponding transformation matrices in momentum $T_{\mathbf{k}}$, orbital T_l ($\{xy, yz, zx\}$), and spin T_σ basis. C_4 is a rotation by $\pi/2$ around the z axis, while σ_x, σ_y, and σ_z are mirrors with respect to the yz, zx, and xy planes.

g	$T_{\mathbf{k}}$	T_l	T_σ
C_4	$\begin{pmatrix} 0 & -1 & 0 \\ 1 & 0 & 0 \\ 0 & 0 & 1 \end{pmatrix}$	$\begin{pmatrix} -1 & 0 & 0 \\ 0 & 0 & 1 \\ 0 & -1 & 0 \end{pmatrix}$	$\begin{pmatrix} \frac{1+i}{\sqrt{2}} & 0 \\ 0 & \frac{1-i}{\sqrt{2}} \end{pmatrix}$
σ_x	$\begin{pmatrix} -1 & 0 & 0 \\ 0 & 1 & 0 \\ 0 & 0 & 1 \end{pmatrix}$	$\begin{pmatrix} -1 & 0 & 0 \\ 0 & 1 & 0 \\ 0 & 0 & -1 \end{pmatrix}$	$\begin{pmatrix} 0 & i \\ i & 0 \end{pmatrix}$
σ_y	$\begin{pmatrix} 1 & 0 & 0 \\ 0 & -1 & 0 \\ 0 & 0 & 1 \end{pmatrix}$	$\begin{pmatrix} -1 & 0 & 0 \\ 0 & -1 & 0 \\ 0 & 0 & 1 \end{pmatrix}$	$\begin{pmatrix} 0 & 1 \\ -1 & 0 \end{pmatrix}$
σ_z	$\begin{pmatrix} 1 & 0 & 0 \\ 0 & 1 & 0 \\ 0 & 0 & -1 \end{pmatrix}$	$\begin{pmatrix} 1 & 0 & 0 \\ 0 & -1 & 0 \\ 0 & 0 & -1 \end{pmatrix}$	$\begin{pmatrix} i & 0 \\ 0 & -i \end{pmatrix}$

TABLE VI. Character table for the D_{4h} space group. Each row is assigned to an irrep. Each column is a class of symmetry operations with dimension as the prefactor. Each operations can be expressed in terms of the generators of Table V. E is identity, C_4 is a $\pi/2$ rotation around the z axis, C_2, C_2', and C_2'' are π rotations around the z axis, the x or y axis and the $(x+y)$- or $(x-y)$ axis, i is inversion and S_4, σ_h, σ_v, σ_d are C_4, C_2, C_2', C_2'' times i, respectively.

D_{4h}	E	$2C_4$	C_2	$2C_2'$	$2C_2''$	i	$2S_4$	σ_h	$2\sigma_v$	$2\sigma_d$
A_{1g}	1	1	1	1	1	1	1	1	1	1
A_{2g}	1	1	1	−1	−1	1	1	1	−1	−1
B_{1g}	1	−1	1	1	−1	1	−1	1	1	−1
B_{2g}	1	−1	1	−1	1	1	−1	1	−1	1
E_g	2	0	−2	0	0	2	0	−2	0	0
A_{1u}	1	1	1	1	1	−1	−1	−1	−1	−1
A_{2u}	1	1	1	−1	−1	−1	−1	−1	1	1
B_{1u}	1	−1	1	1	−1	−1	1	−1	−1	1
B_{2u}	1	−1	1	−1	1	−1	1	−1	1	−1
E_u	2	0	−2	0	0	−2	0	2	0	0

APPENDIX G: GROUP THEORY AND D_{4h} SPACE GROUP

The normal state of the system is invariant under a set G of symmetry operations g. They define the space group of the system and can all be constructed from a set of generators. In the case of SRO and as discussed in previous works [14,34,123,127], the generators are written in Table V, along with their representations in momentum, orbital, and spin basis.

Thus, the annihilation operators transform like

$$[\hat{g}\psi_{\mathbf{k}}]^{\mu_1} = [T(g)]^{\mu_1\mu_2}[\psi_{T_{\mathbf{k}}(g^{-1})\mathbf{k}}]^{\mu_2} \tag{G1}$$

where $T(g) = T_l(g) \otimes T_\sigma(g)$. It follows that gap functions transform like

$$[\hat{g}\Delta]_{\mathbf{k}}^{\mu_1\mu_2} = [T(g)]^{\mu_1\mu_3}[T(g)]^{\mu_2\mu_4}\Delta_{T_{\mathbf{k}}(g^{-1})\mathbf{k}}^{\mu_3\mu_4}. \tag{G2}$$

Any space group can be decomposed into a set of irreducible representations (irreps). They characterize the fundamental ways objects transform under the operations of the group. For an object ϕ^p, which transforms like the one-dimensional irrep p, we have $\hat{g}\phi^p = \chi^p(g)\phi^p$ where $\chi^p(g)$ is the character of the operation g for the p irrep. The n-dimensional irreps are characterized by n independent objects $\{\phi_i^p\}_{i\in\mathbb{N}}$, which transforms like

$$\hat{g}\phi_i^p = \sum_j \chi_{ij}^p \phi_j^p. \tag{G3}$$

In these cases, the character of the operation g for the p irrep is given as $\chi^p(g) = \text{Tr}[\chi_{ij}^p]$. For the D_{4h} space group, the character table is printed in Table VI.

The projector operator $\hat{\mathcal{P}}^p$ selects only the contribution associated with the p irrep. It is defined and acts as

$$\hat{\mathcal{P}}^p = \frac{1}{N_G}\sum_{g\in G}[\chi^p(g)]^*\hat{g}, \quad \hat{\mathcal{P}}^p\boldsymbol{\phi}^q = \delta_{pq}\boldsymbol{\phi}^p \tag{G4}$$

where N_G is the number of symmetry operations of the group. To characterize the symmetry of an order parameter, we find the irrep that represents its transformation properties under the operations of the group. There is a set of basis functions for each of the four quantum numbers characterizing a gap function. These basis functions can be classified with the irrep that represents how they transform.

APPENDIX H: CONVERGENCE OF THE GAP FUNCTIONS

While the gap functions considered have orbital and spin basis that have a fixed number of states, the relative momentum and frequency are discretized so their convergence needs to be studied. In momentum space, temperature introduces a broadening in the Green's functions, thus high temperatures do not necessitate large numbers of $\mathbf{k}$ points. Lowering temperatures however, the Green's functions become increasingly sharp and better resolutions are required. In Figs. 17(a) and 17(b), we study the ▲ (B_{1g}^+ leading) and ★ (A_{2g}^- leading) points of Fig. 8, respectively. For temperatures going from 100 to 450 K, we present the eigenvalues of the five leading eigenvectors as a function of the grid size L characterizing $L \times L \times 2$ $\mathbf{q}$-grids for the susceptibilities.

These $\mathbf{q}$-grid convergence calculations are all performed with two fermionic frequencies. The eigenvalues are classified by their global irrep, with the same colors as in Fig. 13. For each irreps ν and each temperature T, the eigenvalue at the largest L is presumed converged and we fit an exponential on the other values to define the error $\Delta\lambda_{\mathbf{q}}^\nu(T)$ associated to $\mathbf{q}$-point convergence. At high temperatures than 450 K, we simply take the eigenvalues for $L = 24$ as they are well converged. The phase diagram of Fig. 8 is using irreps at 250 K for $L = 24$, indicated by the dash lines.

Since the pairing interactions are dynamical and delayed in time, the fermionic frequencies should also be converged. However, solving the Eliashberg equation for a large number of fermionic frequencies in a multiorbital and strongly $\mathbf{q}$-dependent system like SRO is very challenging. Because Matsubara frequencies are spaced proportionally to temperature, they are very spread at large temperature and the first fermionic Matsubara frequencies $\pm i\omega_0$ are sufficient to capture all the dynamics of the gap functions. At lower temperature, again, the proximity of the frequencies to the origin
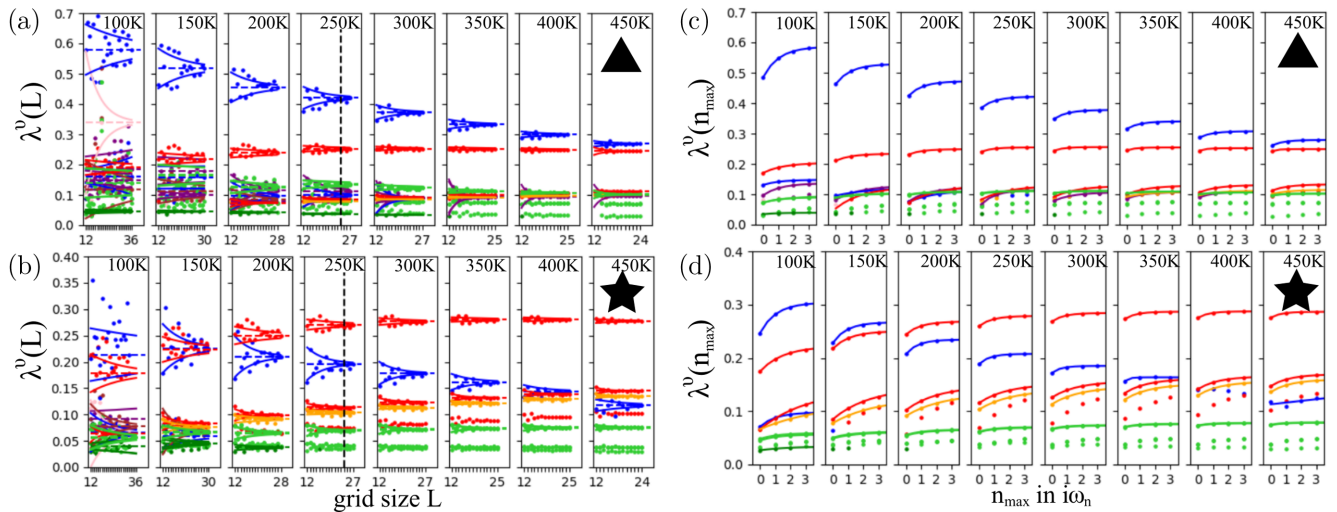
FIG. 17. Grid size dependence of the eigenvalues for various temperatures (a) for the triangle point in parameter space where the dominant eigenvalue is B_{1g}^+ and (b) for the star point where the dominant eigenvalue is A_{2g}^-. Convergence of the eigenvalues in the number of fermionic frequencies n_{max} for the $15 \times 15 \times 2$ **q**-grid for (c) the triangle point in parameter space and (d) for the star point.

implies that a lot of frequencies are required to have accurate eigenvalues. In Figs. 17(c) and 17(d), we present frequency convergences of the superconducting eigenvalues with respect to temperatures ranging from 100 to 450 K. Each eigenvector is again assigned a global irrep with color defined in Fig. 13.

For each temperature T and each irrep ν, we fit an exponential function and look at the value at infinity to define the error $\Delta \lambda_{i\omega_n}^\nu(T)$ associated to the frequency convergence. The error bars in Fig. 13 are given as the sum of the errors $\Delta \lambda_{\mathbf{q}}^\nu(T) + \Delta \lambda_{i\omega_n}^\nu(T)$.

[1] D. J. Van Harlingen, Phase-sensitive tests of the symmetry of the pairing state in the high-temperature superconductors— Evidence for $d_{x^2-y^2}$ symmetry, Rev. Mod. Phys. **67**, 515 (1995).

[2] D. J. Scalapino, The case for $d_{x^2-y^2}$ pairing in the cuprate superconductors, Phys. Rep. **250**, 329 (1995).

[3] D. J. Scalapino, Superconductivity and spin fluctuations, J. Low Temp. Phys. **117**, 179 (1999).

[4] T. A. Maier, M. Jarrell, T. C. Schulthess, P. R. C. Kent, and J. B. White, Systematic Study of d-Wave Superconductivity in the 2D Repulsive Hubbard Model, Phys. Rev. Lett. **95**, 237001 (2005).

[5] B. Kyung, D. Sénéchal, and A.-M. S. Tremblay, Pairing dynamics in strongly correlated superconductivity, Phys. Rev. B **80**, 205109 (2009).

[6] N. P. Armitage, P. Fournier, and R. L. Greene, Progress and perspectives on electron-doped cuprates, Rev. Mod. Phys. **82**, 2421 (2010).

[7] E. Gull, O. Parcollet, and A. J. Millis, Superconductivity and the Pseudogap in the Two-Dimensional Hubbard Model, Phys. Rev. Lett. **110**, 216405 (2013).

[8] L. Fratino, P. Sémon, G. Sordi, and A.-M. S. Tremblay, An organizing principle for two-dimensional strongly correlated superconductivity, Sci. Rep. **6**, 22715 (2016).

[9] N. Kowalski, S. S. Dash, P. Sémon, D. Sénéchal, and A.-M. Tremblay, Oxygen hole content, charge-transfer gap, covalency, and cuprate superconductivity, Proc. Natl. Acad. Sci. USA **118**, e2106476118 (2021).

[10] G. R. Stewart, Superconductivity in iron compounds, Rev. Mod. Phys. **83**, 1589 (2011).

[11] X. Wu, W. A. Benalcazar, Y. Li, R. Thomale, C.-X. Liu, and J. Hu, Boundary-Obstructed Topological High-T_c Superconductivity in Iron Pnictides, Phys. Rev. X **10**, 041014 (2020).

[12] A. P. Mackenzie, T. Scaffidi, C. W. Hicks, and Y. Maeno, Even odder after twenty-three years: The superconducting order parameter puzzle of Sr_2RuO_4, npj Quantum Mater. **2**, 40 (2017).

[13] W. Huang, A review of some new perspectives on the theory of superconducting Sr_2RuO_4, Chin. Phys. B **30**, 107403 (2021).

[14] S.-O. Kaba and D. Sénéchal, Group-theoretical classification of superconducting states of strontium ruthenate, Phys. Rev. B **100**, 214507 (2019).

[15] W. Huang, Y. Zhou, and H. Yao, Exotic cooper pairing in multiorbital models of Sr_2RuO_4, Phys. Rev. B **100**, 134506 (2019).

[16] K. Ishida, H. Mukuda, Y. Kitaoka, K. Asayama, Z. Q. Mao, Y. Mori, and Y. Maeno, Spin-triplet superconductivity in Sr_2RuO_4 identified by ^{17}O Knight shift, Nature (London) **396**, 658 (1998).

[17] A. P. Mackenzie and Y. Maeno, The superconductivity of Sr_2RuO_4 and the physics of spin-triplet pairing, Rev. Mod. Phys. **75**, 657 (2003).

[18] A. Pustogow, Y. Luo, A. Chronister, Y.-S. Su, D. A. Sokolov, F. Jerzembeck, A. P. Mackenzie, C. W. Hicks, N. Kikugawa, S. Raghu, *et al.*, Constraints on the superconducting order parameter in Sr_2RuO_4 from oxygen-17 nuclear magnetic resonance, Nature (London) **574**, 72 (2019).

[19] K. Ishida, M. Manago, K. Kinjo, and Y. Maeno, Reduction of the ^{17}O knight shift in the superconducting state and the heat-up effect by NMR pulses on Sr_2RuO_4, J. Phys. Soc. Jpn. **89**, 034712 (2020).

[20] A. Chronister, A. Pustogow, N. Kikugawa, D. A. Sokolov, F. Jerzembeck, C. W. Hicks, A. P. Mackenzie, E. D. Bauer, and S. E. Brown, Evidence for even parity unconventional superconductivity in Sr_2RuO_4, Proc. Natl. Acad. Sci. USA **118**, e2025313118 (2021).

[21] J. A. Duffy, S. M. Hayden, Y. Maeno, Z. Mao, J. Kulda, and G. J. McIntyre, Polarized-Neutron Scattering Study of the Cooper-Pair Moment in Sr_2RuO_4, Phys. Rev. Lett. **85**, 5412 (2000).

[22] A. N. Petsch, M. Zhu, M. Enderle, Z. Q. Mao, Y. Maeno, I. I. Mazin, and S. M. Hayden, Reduction of the Spin Susceptibility in the Superconducting State of Sr_2RuO_4 Observed by Polarized Neutron Scattering, Phys. Rev. Lett. **125**, 217004 (2020).

[23] A. Steppke, L. Zhao, M. E. Barber, T. Scaffidi, F. Jerzembeck, H. Rosner, A. S. Gibbs, Y. Maeno, S. H. Simon, A. P. Mackenzie, and C. W. Hicks, Strong peak in T_c of Sr_2RuO_4 under uniaxial pressure, Science **355**, eaaf9398 (2017).

[24] G. M. Luke, Y. Fudamoto, K. M. Kojima, M. I. Larkin, J. Merrin, B. Nachumi, Y. J. Uemura, Y. Maeno, Z. Q. Mao, Y. Mori, *et al.*, Time-reversal symmetry-breaking superconductivity in Sr_2RuO_4, Nature (London) **394**, 558 (1998).

[25] J. Xia, Y. Maeno, P. T. Beyersdorf, M. M. Fejer, and A. Kapitulnik, High Resolution Polar Kerr Effect Measurements of Sr_2RuO_4: Evidence for Broken Time-Reversal Symmetry in the Superconducting State, Phys. Rev. Lett. **97**, 167002 (2006).

[26] S. Benhabib, C. Lupien, I. Paul, L. Berges, M. Dion, M. Nardone, A. Zitouni, Z. Q. Mao, Y. Maeno, A. Georges, *et al.*, Ultrasound evidence for a two-component superconducting order parameter in Sr_2RuO_4, Nat. Phys. **17**, 194 (2021).

[27] S. Ghosh, A. Shekhter, F. Jerzembeck, N. Kikugawa, D. A. Sokolov, M. Brando, A. P. Mackenzie, C. W. Hicks, and B. J. Ramshaw, Thermodynamic evidence for a two-component superconducting order parameter in Sr_2RuO_4, Nat. Phys. **17**, 199 (2021).

[28] V. Sunko, E. Abarca Morales, I. Marković, M. E. Barber, D. Milosavljević, F. Mazzola, D. A. Sokolov, N. Kikugawa, C. Cacho, P. Dudin, *et al.*, Direct observation of a uniaxial stress-driven Lifshitz transition in Sr_2RuO_4, npj Quantum Mater. **4**, 46 (2019).

[29] V. Grinenko, S. Ghosh, R. Sarkar, J.-C. Orain, A. Nikitin, M. Elender, D. Das, Z. Guguchia, F. Brückner, M. E. Barber, *et al.*, Split superconducting and time-reversal symmetry-breaking transitions in Sr_2RuO_4 under stress, Nat. Phys. **17**, 748 (2021).

[30] Y.-S. Li, N. Kikugawa, D. A. Sokolov, F. Jerzembeck, A. S. Gibbs, Y. Maeno, C. W. Hicks, J. Schmalian, M. Nicklas, and A. P. Mackenzie, High-sensitivity heat-capacity measurements on Sr_2RuO_4 under uniaxial pressure, Proc. Natl. Acad. Sci. USA **118**, e2020492118 (2021).

[31] C. Kallin and A. J. Berlinsky, Is Sr_2RuO_4 a chiral *p*-wave superconductor?, J. Phys.: Condens. Matter **21**, 164210 (2009).

[32] S. Ghosh, T. G. Kiely, A. Shekhter, F. Jerzembeck, N. Kikugawa, D. A. Sokolov, A. P. Mackenzie, and B. J. Ramshaw, Strong increase in ultrasound attenuation below T_c in Sr_2RuO_4: Possible evidence for domains, Phys. Rev. B **106**, 024520 (2022).

[33] R. Willa, M. Hecker, R. M. Fernandes, and J. Schmalian, Inhomogeneous time-reversal symmetry breaking in Sr_2RuO_4, Phys. Rev. B **104**, 024511 (2021).

[34] H. G. Suh, H. Menke, P. M. R. Brydon, C. Timm, A. Ramires, and D. F. Agterberg, Stabilizing even-parity chiral superconductivity in Sr_2RuO_4, Phys. Rev. Research **2**, 032023(R) (2020).

[35] J. Clepkens, A. W. Lindquist, and H.-Y. Kee, Shadowed triplet pairings in Hund's metals with spin-orbit coupling, Phys. Rev. Research **3**, 013001 (2021).

[36] N. E. Hussey, A. P. Mackenzie, J. R. Cooper, Y. Maeno, S. Nishizaki, and T. Fujita, Normal-state magnetoresistance of Sr_2RuO_4, Phys. Rev. B **57**, 5505 (1998).

[37] M. W. Haverkort, I. S. Elfimov, L. H. Tjeng, G. A. Sawatzky, and A. Damascelli, Strong Spin-Orbit Coupling Effects on the Fermi Surface of Sr_2RuO_4 and Sr_2RhO_4, Phys. Rev. Lett. **101**, 026406 (2008).

[38] E. Hassinger, P. Bourgeois-Hope, H. Taniguchi, S. René de Cotret, G. Grissonnanche, M. S. Anwar, Y. Maeno, N. Doiron-Leyraud, and L. Taillefer, Vertical Line Nodes in the Superconducting Gap Structure of Sr_2RuO_4, Phys. Rev. X **7**, 011032 (2017).

[39] R. Sharma, S. D. Edkins, Z. Wang, A. Kostin, C. Sow, Y. Maeno, A. P. Mackenzie, J. C. S. Davis, and V. Madhavan, Momentum-resolved superconducting energy gaps of Sr_2RuO_4 from quasiparticle interference imaging, Proc. Natl. Acad. Sci. USA **117**, 5222 (2020).

[40] O. Gingras, R. Nourafkan, A.-M. S. Tremblay, and M. Côté, Superconducting Symmetries of Sr_2RuO_4 from First-Principles Electronic Structure, Phys. Rev. Lett. **123**, 217005 (2019).

[41] Y. Sidis, M. Braden, P. Bourges, B. Hennion, S. NishiZaki, Y. Maeno, and Y. Mori, Evidence for Incommensurate Spin Fluctuations in Sr_2RuO_4, Phys. Rev. Lett. **83**, 3320 (1999).

[42] S. Raghu, S. B. Chung, and S. Lederer, Theory of 'hidden' quasi-1D superconductivity in Sr_2RuO_4, J. Phys.: Conf. Ser. **449**, 012031 (2013).

[43] A. T. Rømer, D. D. Scherer, I. M. Eremin, P. J. Hirschfeld, and B. M. Andersen, Knight Shift and Leading Superconducting Instability from Spin Fluctuations in Sr_2RuO_4, Phys. Rev. Lett. **123**, 247001 (2019).

[44] A. T. Rømer and B. M. Andersen, Fluctuation-driven superconductivity in Sr_2RuO_4 from weak repulsive interactions, Mod. Phys. Lett. B **34**, 2040052 (2020).

[45] T. Scaffidi, J. C. Romers, and S. H. Simon, Pairing symmetry and dominant band in Sr_2RuO_4, Phys. Rev. B **89**, 220510(R) (2014).

[46] W. Huang and H. Yao, Possible Three-Dimensional Nematic Odd-Parity Superconductivity in Sr_2RuO_4, Phys. Rev. Lett. **121**, 157002 (2018).

[47] H. S. Røising, T. Scaffidi, F. Flicker, G. F. Lange, and S. H. Simon, Superconducting order of Sr_2RuO_4 from a three-dimensional microscopic model, Phys. Rev. Research **1**, 033108 (2019).

[48] T. Scaffidi, Degeneracy between even- and odd-parity superconductivity in the quasi-1D Hubbard model and implications for Sr_2RuO_4, arXiv:2007.13769.

[49] W. Huang and Z. Wang, Possibility of mixed helical *p*-wave pairings in Sr_2RuO_4, Phys. Rev. Research **3**, L042002 (2021).

[50] S. A. Kivelson, A. C. Yuan, B. Ramshaw, and R. Thomale, A proposal for reconciling diverse experiments on the superconducting state in Sr$_2$RuO$_4$, npj Quantum Mater. **5**, 43 (2020).

[51] A. C. Yuan, E. Berg, and S. A. Kivelson, Strain-induced time reversal breaking and half quantum vortices near a putative superconducting tetra-critical point in Sr$_2$RuO$_4$, Phys. Rev. B **104**, 054518 (2021).

[52] J. Clepkens, A. W. Lindquist, X. Liu, and H.-Y. Kee, Higher angular momentum pairings in interorbital shadowed-triplet superconductors: Application to Sr$_2$RuO$_4$, Phys. Rev. B **104**, 104512 (2021).

[53] G. Wagner, H. S. Røising, F. Flicker, and S. H. Simon, Microscopic Ginzburg-Landau theory and singlet ordering in Sr$_2$RuO$_4$, Phys. Rev. B **104**, 134506 (2021).

[54] Y. Sheng, Y. Li, and Y.-f. Yang, Superconducting pairing mechanism of Sr$_2$RuO$_4$, Phys. Rev. B **106**, 054516 (2022).

[55] A. T. Rømer, P. J. Hirschfeld, and B. M. Andersen, Superconducting state of Sr$_2$RuO$_4$ in the presence of longer-range Coulomb interactions, Phys. Rev. B **104**, 064507 (2021).

[56] S. Bhattacharyya, A. Kreisel, X. Kong, T. Berlijn, A. T. Rømer, B. M. Andersen, and P. J. Hirschfeld, Superconducting gap symmetry from Bogoliubov quasiparticle interference analysis on Sr$_2$RuO$_4$, arXiv:2109.10712.

[57] V. Grinenko, D. Das, R. Gupta, B. Zinkl, N. Kikugawa, Y. Maeno, C. W. Hicks, H.-H. Klauss, M. Sigrist, and R. Khasanov, Unsplit superconducting and time reversal symmetry breaking transitions in Sr$_2$RuO$_4$ under hydrostatic pressure and disorder, Nat. Commun. **12**, 3920 (2021).

[58] B. Zinkl and M. Sigrist, Impurity-induced double transitions for accidentally degenerate unconventional pairing states, Phys. Rev. Research **3**, L012004 (2021).

[59] M. T. Béal-Monod, C. Bourbonnais, and V. J. Emery, Possible superconductivity in nearly antiferromagnetic itinerant fermion systems, Phys. Rev. B **34**, 7716 (1986).

[60] D. J. Scalapino, E. Loh, and J. E. Hirsch, *d*-wave pairing near a spin-density-wave instability, Phys. Rev. B **34**, 8190 (1986).

[61] G. Esirgen and N. E. Bickers, Fluctuation exchange analysis of superconductivity in the standard three-band CuO$_2$ model, Phys. Rev. B **57**, 5376 (1998).

[62] J. Bardeen, L. N. Cooper, and J. R. Schrieffer, Theory of Superconductivity, Phys. Rev. **108**, 1175 (1957).

[63] V. L. Ginzburg and L. D. Landau, Phenomenological theory, J. Exp. Theor. Phys. USSR **20**, 17 (1950).

[64] J. Linder and A. V. Balatsky, Odd-frequency superconductivity, Rev. Mod. Phys. **91**, 045005 (2019).

[65] V. L. Berezinskii, New model of the anisotropic phase of superfluid He^3, JETP Lett. **20**, 287 (1974).

[66] A. Balatsky and E. Abrahams, New class of singlet superconductors, which break the time reversal and parity, Phys. Rev. B **45**, 13125 (1992).

[67] E. Abrahams, A. Balatsky, J. R. Schrieffer, and P. B. Allen, Interactions for odd-ω-gap singlet superconductors, Phys. Rev. B **47**, 513 (1993).

[68] E. Abrahams, A. Balatsky, D. J. Scalapino, and J. R. Schrieffer, Properties of odd-gap superconductors, Phys. Rev. B **52**, 1271 (1995).

[69] W. Huang, E. Taylor, and C. Kallin, Vanishing edge currents in non-*p*-wave topological chiral superconductors, Phys. Rev. B **90**, 224519 (2014).

[70] A. Di Bernardo, S. Diesch, Y. Gu, J. Linder, G. Divitini, C. Ducati, E. Scheer, M. G. Blamire, and J. W. A. Robinson, Signature of magnetic-dependent gapless odd frequency states at superconductor/ferromagnet interfaces, Nat. Commun. **6**, 8053 (2015).

[71] J. A. Krieger, A. Pertsova, S. R. Giblin, M. Döbeli, T. Prokscha, C. W. Schneider, A. Suter, T. Hesjedal, A. V. Balatsky, and Z. Salman, Proximity-Induced Odd-Frequency Superconductivity in a Topological Insulator, Phys. Rev. Lett. **125**, 026802 (2020).

[72] V. Perrin, F. L. N. Santos, G. C. Ménard, C. Brun, T. Cren, M. Civelli, and P. Simon, Unveiling Odd-Frequency Pairing around a Magnetic Impurity in a Superconductor, Phys. Rev. Lett. **125**, 117003 (2020).

[73] E. Taylor and C. Kallin, Intrinsic Hall Effect in a Multiband Chiral Superconductor in the Absence of an External Magnetic Field, Phys. Rev. Lett. **108**, 157001 (2012).

[74] A. M. Black-Schaffer and A. V. Balatsky, Odd-frequency superconducting pairing in multiband superconductors, Phys. Rev. B **88**, 104514 (2013).

[75] C. Triola, J. Cayao, and A. M. Black-Schaffer, The role of odd-frequency pairing in multiband superconductors, Ann. Phys. **532**, 1900298 (2020).

[76] L. Komendová and A. M. Black-Schaffer, Odd-Frequency Superconductivity in Sr$_2$RuO$_4$ Measured by Kerr Rotation, Phys. Rev. Lett. **119**, 087001 (2017).

[77] S. Käser, H. U. R. Strand, N. Wentzell, A. Georges, O. Parcollet, and P. Hansmann, Inter-orbital singlet pairing in Sr$_2$RuO$_4$: A Hund's superconductor, Phys. Rev. B **105**, 155101 (2022).

[78] N. E. Bickers, Self-consistent many-body theory for condensed matter systems, in *Theoretical Methods for Strongly Correlated Electrons*, CRM Series in Mathematical Physics, edited by D. Sénéchal, A.-M. Tremblay, and C. Bourbonnais (Springer, New York, 2004), pp. 237–296.

[79] R. Nourafkan, Nodal versus nodeless superconductivity in isoelectronic LiFeP and LiFeAs, Phys. Rev. B **93**, 241116(R) (2016).

[80] J. Hubbard, Electron correlations in narrow energy bands, Proc. R. Soc. London A **276**, 238 (1963).

[81] J. Hubbard, Electron correlations in narrow energy bands. II. The degenerate band case, Proc. R. Soc. London A **277**, 237 (1964).

[82] J. Hubbard, Electron correlations in narrow energy bands III. An improved solution, Proc. R. Soc. London A **281**, 401 (1964).

[83] J. Kanamori, Electron correlation and ferromagnetism of transition metals, Prog. Theor. Phys. **30**, 275 (1963).

[84] M. C. Gutzwiller, Effect of Correlation on the Ferromagnetism of Transition Metals, Phys. Rev. Lett. **10**, 159 (1963).

[85] A. Georges, L. d. Medici, and J. Mravlje, Strong correlations from Hund's coupling, Annu. Rev. Condens. Matter Phys. **4**, 137 (2013).

[86] J. Mravlje, M. Aichhorn, T. Miyake, K. Haule, G. Kotliar, and A. Georges, Coherence-Incoherence Crossover and the Mass-Renormalization Puzzles in Sr$_2$RuO$_4$, Phys. Rev. Lett. **106**, 096401 (2011).

[87] G. Zhang, E. Gorelov, E. Sarvestani, and E. Pavarini, Fermi Surface of Sr$_2$RuO$_4$: Spin-Orbit and Anisotropic Coulomb Interaction Effects, Phys. Rev. Lett. **116**, 106402 (2016).

[88] M. Kim, J. Mravlje, M. Ferrero, O. Parcollet, and A. Georges, Spin-Orbit Coupling and Electronic Correlations in Sr_2RuO_4, Phys. Rev. Lett. **120**, 126401 (2018).

[89] A. Tamai, M. Zingl, E. Rozbicki, E. Cappelli, S. Ricco, A. de la Torre, S. McKeown Walker, F. Y. Bruno, P. D. C. King, W. Meevasana, M. Shi, M. Radovic, N. C. Plumb, A. S. Gibbs, A. P. Mackenzie, C. Berthod, H. U. R. Strand, M. Kim, A. Georges, and F. Baumberger, High-Resolution Photoemission on Sr_2RuO_4 Reveals Correlation-Enhanced Effective Spin-Orbit Coupling and Dominantly Local Self-Energies, Phys. Rev. X **9**, 021048 (2019).

[90] H. U. R. Strand, M. Zingl, N. Wentzell, O. Parcollet, and A. Georges, Magnetic response of Sr_2RuO_4: Quasi-local spin fluctuations due to Hund's coupling, Phys. Rev. B **100**, 125120 (2019).

[91] F. B. Kugler, M. Zingl, H. U. R. Strand, S.-S. B. Lee, J. von Delft, and A. Georges, Strongly Correlated Materials from a Numerical Renormalization Group Perspective: How the Fermi-Liquid State of Sr_2RuO_4 Emerges, Phys. Rev. Lett. **124**, 016401 (2020).

[92] C. N. Veenstra, Z.-H. Zhu, M. Raichle, B. M. Ludbrook, A. Nicolaou, B. Slomski, G. Landolt, S. Kittaka, Y. Maeno, J. H. Dil, I. S. Elfimov, M. W. Haverkort, and A. Damascelli, Spin-Orbital Entanglement and the Breakdown of Singlets and Triplets in Sr_2RuO_4 Revealed by Spin- and Angle-Resolved Photoemission Spectroscopy, Phys. Rev. Lett. **112**, 127002 (2014).

[93] X. Gonze, B. Amadon, G. Antonius, F. Arnardi, L. Baguet, J.-M. Beuken, J. Bieder, F. Bottin, J. Bouchet, E. Bousquet *et al.*, The Abinit project: Impact, environment and recent developments, Comput. Phys. Commun. **248**, 107042 (2020).

[94] A. H. Romero, D. C. Allan, B. Amadon, G. Antonius, T. Applencourt, L. Baguet, J. Bieder, F. Bottin, J. Bouchet, E. Bousquet *et al.*, ABINIT: Overview and focus on selected capabilities, J. Chem. Phys. **152**, 124102 (2020).

[95] B. Amadon, F. Lechermann, A. Georges, F. Jollet, T. O. Wehling, and A. I. Lichtenstein, Plane-wave based electronic structure calculations for correlated materials using dynamical mean-field theory and projected local orbitals, Phys. Rev. B **77**, 205112 (2008).

[96] P. E. Blöchl, Projector augmented-wave method, Phys. Rev. B **50**, 17953 (1994).

[97] M. Torrent, F. Jollet, F. Bottin, G. Zérah, and X. Gonze, Implementation of the projector augmented-wave method in the ABINIT code: Application to the study of iron under pressure, Comput. Mater. Sci. **42**, 337 (2008).

[98] C. Bergemann, J. S. Brooks, L. Balicas, A. P. Mackenzie, S. R. Julian, Z. Q. Mao, and Y. Maeno, Normal state of the unconventional superconductor Sr_2RuO_4 in high magnetic fields, Phys. B: Condens. Matter, **294-295**, 371 (2001).

[99] J. P. Carlo, T. Goko, I. M. Gat-Maluranu, P. L. Russo, A. T. Savici, A. A. Aczel, G. J. MacDougall, J. A. Rodriguez, T. J. Williams, G. M. Luke, *et al.*, New magnetic phase diagram of $(Sr, Ca)_2RuO_4$, Nat. Mater. **11**, 323 (2012).

[100] K. Iida, M. Kofu, N. Katayama, J. Lee, R. Kajimoto, Y. Inamura, M. Nakamura, M. Arai, Y. Yoshida, M. Fujita, K. Yamada, and S.-H. Lee, Inelastic neutron scattering study of the magnetic fluctuations in Sr_2RuO_4, Phys. Rev. B **84**, 060402(R) (2011).

[101] P. Steffens, Y. Sidis, J. Kulda, Z. Q. Mao, Y. Maeno, I. I. Mazin, and M. Braden, Spin Fluctuations in $Sr_2 RuO_4$ from Polarized Neutron Scattering: Implications for Superconductivity, Phys. Rev. Lett. **122**, 047004 (2019).

[102] K. Jenni, S. Kunkemöller, P. Steffens, Y. Sidis, R. Bewley, Z. Q. Mao, Y. Maeno, and M. Braden, Neutron scattering studies on spin fluctuations in Sr_2RuO_4, Phys. Rev. B **103**, 104511 (2021).

[103] E. J. Rozbicki, J. F. Annett, J.-R. Souquet, and A. P. Mackenzie, Spin–orbit coupling and k-dependent Zeeman splitting in strontium ruthenate, J. Phys.: Condens. Matter **23**, 094201 (2011).

[104] K. Iida, M. Kofu, K. Suzuki, N. Murai, S. Ohira-Kawamura, R. Kajimoto, Y. Inamura, M. Ishikado, S. Hasegawa, T. Masuda, *et al.*, Horizontal line nodes in Sr_2RuO_4 proved by spin resonance, J. Phys. Soc. Jpn. **89**, 053702 (2020).

[105] N. Kikugawa, A. P. Mackenzie, C. Bergemann, R. A. Borzi, S. A. Grigera, and Y. Maeno, Rigid-band shift of the Fermi level in the strongly correlated metal: $Sr_{2−y}La_yRuO_4$, Phys. Rev. B **70**, 060508(R) (2004).

[106] B. Burganov, C. Adamo, A. Mulder, M. Uchida, P. D. C. King, J. W. Harter, D. E. Shai, A. S. Gibbs, A. P. Mackenzie, R. Uecker, M. Bruetzam, M. R. Beasley, C. J. Fennie, D. G. Schlom, and K. M. Shen, Strain Control of Fermiology and Many-Body Interactions in Two-Dimensional Ruthenates, Phys. Rev. Lett. **116**, 197003 (2016).

[107] H. J. Lee, C. H. Kim, and A. Go, Interplay between spin-orbit coupling and Van Hove singularity in the Hund's metallicity of Sr_2RuO_4, Phys. Rev. B **102**, 195115 (2020).

[108] I. Lifshitz, Anomalies of electron characteristics of a metal in the high pressure region, Sov. Phys. JETP **11**, 1130 (1960).

[109] K. M. Shen, N. Kikugawa, C. Bergemann, L. Balicas, F. Baumberger, W. Meevasana, N. J. C. Ingle, Y. Maeno, Z.-X. Shen, and A. P. Mackenzie, Evolution of the Fermi Surface and Quasiparticle Renormalization through a van Hove Singularity in $Sr_{2−y}La_yRuO_4$, Phys. Rev. Lett. **99**, 187001 (2007).

[110] C. W. Hicks, D. O. Brodsky, E. A. Yelland, A. S. Gibbs, J. A. N. Bruin, M. E. Barber, S. D. Edkins, K. Nishimura, S. Yonezawa, Y. Maeno, and A. P. Mackenzie, Strong increase of T_c of Sr_2RuO_4 under both tensile and compressive strain, Science **344**, 283 (2014).

[111] Y.-C. Liu, W.-S. Wang, F.-C. Zhang, and Q.-H. Wang, Superconductivity in Sr_2RuO_4 thin films under biaxial strain, Phys. Rev. B **97**, 224522 (2018).

[112] C. A. Watson, A. S. Gibbs, A. P. Mackenzie, C. W. Hicks, and K. A. Moler, Micron-scale measurements of low anisotropic strain response of local T_c in Sr_2RuO_4, Phys. Rev. B **98**, 094521 (2018).

[113] Y. S. Li, N. Kikugawa, D. A. Sokolov, F. Jerzembeck, A. S. Gibbs, Y. Maeno, C. W. Hicks, M. Nicklas, and A. P. Mackenzie, High sensitivity heat capacity measurements on Sr_2RuO_4 under uniaxial pressure, arXiv:1906.07597.

[114] J. Karp, M. Bramberger, M. Grundner, U. Schollwöck, A. J. Millis, and M. Zingl, Sr_2MoO_4 and Sr_2RuO_4: Disentangling the Roles of Hund's and van Hove Physics, Phys. Rev. Lett. **125**, 166401 (2020).

[115] E. E. Salpeter and H. A. Bethe, A relativistic equation for bound-state problems, Phys. Rev. **84**, 1232 (1951).

[116] D. J. Scalapino, A common thread: The pairing interaction for unconventional superconductors, Rev. Mod. Phys. **84**, 1383 (2012).

[117] Y. M. Vilk and A.-M. S. Tremblay, Non-perturbative many-body approach to the Hubbard model and single-particle pseudogap, J. Phys. (Paris) I **7**, 1309 (1997).

[118] A. W. Lindquist and H.-Y. Kee, Distinct reduction of Knight shift in superconducting state of Sr_2RuO_4 under uniaxial strain, Phys. Rev. Research **2**, 032055(R) (2020).

[119] A. W. Lindquist, J. Clepkens, and H.-Y. Kee, Evolution of interorbital superconductor to intraorbital spin-density wave in layered ruthenates, Phys. Rev. Research **4**, 023109 (2022).

[120] P. Dutta, F. Parhizgar, and A. M. Black-Schaffer, Superconductivity in spin-3/2 systems: Symmetry classification, odd-frequency pairs, and Bogoliubov Fermi surfaces, Phys. Rev. Research **3**, 033255 (2021).

[121] R. Joynt and L. Taillefer, The superconducting phases of UPt_3, Rev. Mod. Phys. **74**, 235 (2002).

[122] S. Ran, C. Eckberg, Q.-P. Ding, Y. Furukawa, T. Metz, S. R. Saha, I.-L. Liu, M. Zic, H. Kim, J. Paglione *et al.*, Nearly ferromagnetic spin-triplet superconductivity, Science **365**, 684 (2019).

[123] A. Ramires and M. Sigrist, Superconducting order parameter of Sr_2RuO_4: A microscopic perspective, Phys. Rev. B **100**, 104501 (2019).

[124] W. Chen and J. An, Interorbital *p*- and *d*-wave pairings between $d_{xz/yz}$ and d_{xy} orbitals in Sr_2RuO_4, Phys. Rev. B **102**, 094501 (2020).

[125] S.-J. Zhang, D. Wang, and Q.-H. Wang, Possible two-component spin-singlet pairings in Sr_2RuO_4, Phys. Rev. B **104**, 094504 (2021).

[126] M. Tinkham, *Introduction to Superconductivity*, 2nd ed., International Series in Pure and Applied Physics (McGraw Hill, New York, 1996).

[127] R. M. Geilhufe and A. V. Balatsky, Symmetry analysis of odd- and even-frequency superconducting gap symmetries for time-reversal symmetric interactions, Phys. Rev. B **97**, 024507 (2018).

[128] S. L. Altmann and P. Herzig, *Point-Group Theory Tables* (Clarendon Press, Oxford, 1994).

[129] H. Kusunose, Y. Fuseya, and K. Miyake, Possible odd-frequency superconductivity in strong-coupling electron–phonon systems, J. Phys. Soc. Jpn. **80**, 044711 (2011).

[130] R. Balian and N. R. Werthamer, Superconductivity with Pairs in a Relative *p* Wave, Phys. Rev. **131**, 1553 (1963).

[131] P. Coleman, *Introduction to Many-Body Physics* (Cambridge University Press, Cambridge, 2015).

[132] R. Nourafkan and A.-M. S. Tremblay, Effect of nonsymmorphic space groups on correlation functions in iron-based superconductors, Phys. Rev. B **96**, 125140 (2017).

[133] R. Nourafkan, G. Kotliar, and A.-M. S. Tremblay, Correlation-Enhanced Odd-Parity Interorbital Singlet Pairing in the Iron-Pnictide Superconductor LiFeAs, Phys. Rev. Lett. **117**, 137001 (2016).